NORTHWESTERN UNIVERSITY

Altered Mechanics of Schlemm's Canal Endothelial Cells and Trabecular Meshwork in Glaucoma

A DISSERTATION

SUBMITTED TO THE GRADUATE SCHOOL
IN PARTIAL FULFILLMENT OF THE REQUIREMENTS

for the degree

DOCTOR OF PHILOSOPHY

Field of Biomedical Engineering

By

Amir Vahabikashi

EVANSTON, ILLINOIS

December 2016

Abstract

Glaucoma is a neurodegenerative blinding disease associated with increased intraocular pressure, which is caused by an increased resistance to the outflow of aqueous humor. Although the cause for increased resistance remains unknown, it has been associated with a decreased density of pores in the cells of the inner wall endothelium of Schlemm's canal (SC). These pores are thought to form when SC cells experience large deformations in response to a transcellular pressure gradient.

Previous studies established a correlation between the elevated cell stiffness in glaucomatous SC cells and their reduced pore formation capability in-vitro. Here, we extend these studies by (i) mechanically characterizing the SC cell and it substrate properties in-situ and (ii) further characterizing the cyto-mechanical behavior of these cells in vitro, particularly as to how they are affect by changes to their cytoskeleton.

In the first of these studies, we combined atomic force microscopy (AFM) and optical microscopy to establish a new technique to measure the stiffness of SC cells and their underlying substrate, the trabecular meshwork (TM), in-situ. To interpret AFM measurements, finite element modeling (FEM) is used to simulate AFM indentation on a cell with cortex that is sitting on the TM. Our results show that both SC cell stiffness and that of their substrate can be measured simultaneously in-situ. Our in-situ measurements and computational simulations confirm previous in-vitro

findings suggesting that the stiffness is elevated in TM in-situ but further show that SC cells stiffness in-situ is increased in glaucoma, as was already reported in-vitro.

To better understand the cytomechanics of the SC cells, we used agents that altered their cytoskeleton. Dexamethasone is an anti-inflammatory glucocorticoid that can cause steroid-induced glaucoma in some individuals and has been reported to alter the cytoskeleton. We focused on investigating the effect of dexamethasone on SC cell cytoskeleton and mechanics using imaging, AFM, optical magnetic twisting cytometry (OMTC), and traction force microscopy (TFM) studies. Using FEM we have previously shown that AFM sharp probes measure the mechanics of the cell cortex whereas rounded probes mainly characterize the subcortical stiffness of the cell; here we show that OMTC measurements behave similar to AFM rounded probes and thus, probe the mechanics of the subcortical region as opposed to some studies that suggest OMTC characterizes cortex mechanics. Our studies show that dexamethasone treatment alters cytoskeletal distribution and significantly increases cortical stiffness in SC cells, which can potentially impede pore formation.

Finally, to further understand the role of F-actin and vimentin in cell mechanics, the same experimental approaches were used to show that promoting RhoA and α-actinin increases cortex stiffness and traction forces in SC cells and that vimentin plays an integral role in regulating cortex mechanics and traction forces in mouse embryonic fibroblasts.

These findings improve our understanding from the pathogenesis of glaucoma and open a new venue for developing new therapeutics for the disease by targeting SC cell mechanics.

Acknowledgements

I would like to express my gratitude to my advisor Dr. Mark Johnson for his guidance and my doctoral committee members: Drs. Robert Goldman, Matt Glucksbesrg, and Cate Brinson for their advice through my doctoral studies.

I would like to thank Dr. Dan Stamer and Kristin Perkumas for providing SC cells and human eye globes and conducting western blots for our studies, Drs. Tom Read and John Flanagan for kindly hosting me in Canada and providing necessary trainings for extracting the inner wall tissue from the human eye, Dr. Biqin Dong for establishing the optical set up for AFM measurements on the inner wall tissue, Drs. Chan Park for conducting OMTC and TFM studies and Jeff Fredberg for insights about OMTC, Dr. Rudolf Fuchshofer for assistance with western blot data analysis, Dr. Ross Ethier for his suggestion on how to immobilize the inner wall tissue, and CAMI, Nikon Imaging Center, and NUANCE facilities.

I would like to pay tribute to my wife, Mastaneh, my parents Akram and Saeed, my brother, Ali, and my late grandmother, Manji, for their devotion and incessant support throughout different stages of my education.

Funding from the National Institute of Health, grant 2R01EY019696-06, supported this work.

Table of Contents

List of Tables

List of Figures

Chapter 1: Introduction

1.1 Primary open angle glaucoma

Glaucoma is a group of neurodegenerative diseases of the optic nerve that lead to vision loss (Kizhatil et al. 2014). The disease is the leading cause of irreversible blindness and is now growing at a faster pace due to increase in the world population age (Tham et al. 2014). In 2010, 60.5 million people suffered from glaucoma worldwide and it is estimated that this number will increase to 112 million in 2040 (Tham et al. 2014).

Among different types of glaucoma, primary open angle glaucoma (POAG) is the most prevalent type (Quigley & Broman 2006) and it is estimated to affect 3.4 million Americans in 2020 (Vajaranant et al. 2012). Elevated intraocular pressure (IOP) is frequently associated with glaucoma and lowering of IOP is the only proven therapy for glaucoma. The elevated pressure characteristic of glaucoma is caused by increased resistance to the outflow of aqueous humor from the eye (Ellingsen & Grant 1971). However, the major site/s and mechanism for this phenomenon is still a topic of debate and investigation (Johnson 2006).

1.2 Aqueous humor outflow and intraocular pressure

Aqueous humor is secreted in the ciliary muscle in posterior chamber of the eye and passes through the pupil to enter the anterior chamber. It then flows towards the iridocorneal angle and leaves the eye through two pathways (see Figure 1.1A). About 10% of aqueous humor outflow leaves the eye through an "unconventional outflow pathway" (Figure 1.1A). The remaining 90% drains through the “conventional outflow pathway” comprised of the trabecular meshwork (TM), basement membrane of the inner wall endothelium of the Schlemm’s canal, inner wall (IW) endothelium of the Schlemm’s canal, Schlemm’s canal itself, and finally the collecting channels that are connected to the episcleral veins (Freddo & Johnson 2008). The TM itself includes three distinct regions: uveal trabecular meshwork (UVTM), corneoscleral trabecular meshwork (CSTM), and the juxtacanalicular tissue (JCT) (Figure 1.1B).

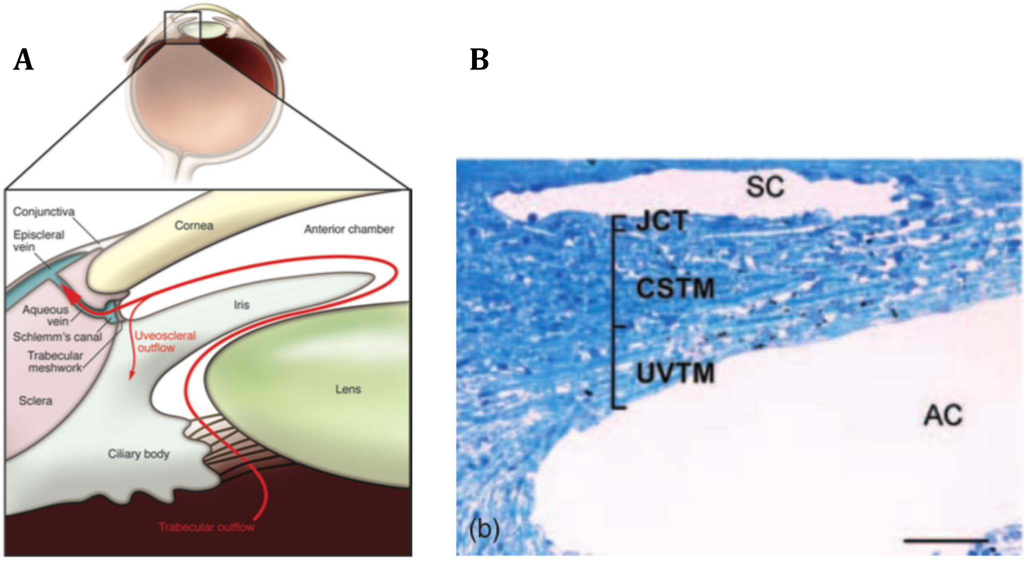

Figure 1.1: The outflow pathway in human eye consists of two routes: conventional and unconventional [A]. Major bulk of the aqueous humor leaves the eye trough the conventional outflow pathway. Image adopted from Fan (2010). A light micrograph of the TM that illustrates the three distinct regions of the tissue [B] (scale bar is 50μm). Image adopted from Johnson (2010)

The intraocular pressure can be calculated using Goldmann equation:

$$\mathrm{IOP} = \frac{\mathrm{F}-\mathrm{F}_{\mathrm{un}}}{\mathrm{C}} + \mathrm{P}_{\mathrm{ev}},$$

where F is the total outflow rate, F_{un} is the unconventional outflow rate, P_{ev} is the pressure in the episcleral vein, and C is the outflow facility (Lei, Overby, et al. 2011). The conventional outflow facility, which is the inverse of flow resistance, is defined as the ratio of pressure difference between the eye and the episcleral veins ($IOP-P_{ev}$) to the flow through the conventional outflow pathway ($F-F_{un}$). The average IOP in normal eyes is reported to be 15.5±2.6 mmHg in general population where pressure higher than 21mmHg are associated with glaucoma (Ethier et al. 2004) although the relationship between IOP and damage to the optic nerve is complex.

The precise location responsible the generation of the bulk of outflow resistance in the normal eye has not yet been definitely identified, nor has the cause by which outflow resistance is elevated in glaucoma been localized or what causes this elevated flow resistance. One hypothesis was that higher IOP would lead to the collapse of the canal and result in higher outflow resistance. Johnson and Kamm (Johnson & Kamm 1983) measured the outflow resistance of a non-glaucomatous human eye at high IOP where they found the resistance to be much lower than that of a glaucomatous eye. This observation ruled out Schlemm's canal as the major contributor causing elevated outflow resistance.

A study by Grant et al. showed that trabeculotomy is able to eliminate the elevated resistance from glaucoma and restore the normal pressure inside the eye (Johnson 2006). Trabeculotomy is a surgical procedure where an opening is created in the TM and extends further through the Schlemm's canal inner wall into the canal. This study confirms that the major contributor to the increased outflow resistance is located near the SC and most likely in the TM or in the inner wall of Schlemm's canal.

Previous studies show that UVTM and CSTM are highly porous structures that barely contribute to outflow resistance and the collector channels are too large to generate a significant resistance in the outflow (Johnson & Tamm 2010). Of the TM components, the JCT possess submicron tortuous pathways and can potentially generate resistance to the outflow. Ethier et al. used electron microscopy (EM) along with Carmen-Kozeny theory to estimate the hydraulic conductivity of the JCT with the conclusion that the JCT could not generate a significant outflow resistance (Ethier et al. 1986). However, they pointed out that if the open spaces in this region were filled with an extracellular matrix gel (that is removed in routine preparation for EM), then these spaces would be able to generate a significant flow resistance. Indeed, Maepna and Bill (1992) used micropipettes to measure the pressure drop in the vicinity of the inner wall endothelium and concluded that JCT is capable of generating significant resistance. Along with the JCT, the basement membranes of the inner wall endothelium is a candidate for generating flow resistance as they have low hydraulic conductivities (Johnson 2006). While the inner wall basement membrane is very thin, which may limit its ability to generate high levels of resistance, Johnson et al. (Johnson 2006) estimated the hydraulic conductivity of the inner wall basement membrane and concluded that it can potentially make significant contributions to the outflow resistance. But, they also mention the caveat that the membrane is discontinuous with breaks, which makes it difficult to evaluate its contribution to the outflow resistance (Johnson 2006).

A final location that can generate significant flow resistance is the inner wall endothelium.

1.3 Inner wall endothelium of Schlemm's Canal and role of pores

The inner wall of the SC is covered with a monolayer of endothelial cells that are similar to vascular linings. The long axes of these cells are oriented along the canal (which is the direction of the flow) and they have lengths and widths of 40-100μm and 5-15μm respectively. The cells are attached to each other and form tight junctions at the areas of contact (Johnson & Tamm 2010). EM studies reveal that these cells go under excessively large deformations and protrude towards the lumen of the canal as a result of the pressure drop across the inner wall endothelium. These invaginations lead to formation of giant vacuoles (GVs) that are followed by the formation of openings on their surface called "pores" (Figure 1.2).

The presence of pores on the surface of the inner wall endothelium had been speculated long before investigators could visualize them using EM, where Seidel et al. (1921) showed the ability of micron sized particles to pass through the outflow pathway (Johnson 2006). Bill and Svedberg used EM to estimate the number and size of the pores and concluded that the tissue could, at most, generate 10% of the total resistance (Bill & Svedberg 1972). While their findings tend to rule out inner wall as major contributor, experimental results showed that rupturing the endothelium using enzymes and agents could decrease the outflow resistance to extents that could not be explained by calculating the resistance caused by the pores (Johnson & Tamm 2010).

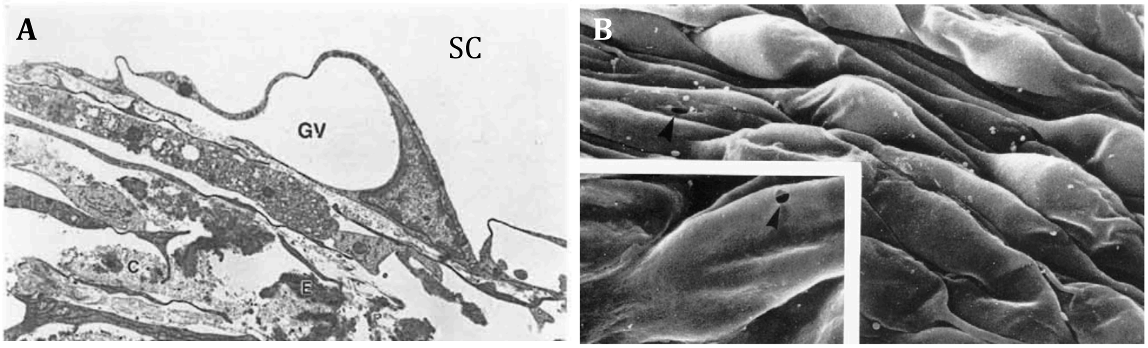

Figure 1.2: Transmission electron micrograph of the JCT and a giant vacuole (GV) in a human eye fixed at an IOP of 15mmHg [A] (Image from Johnson et al. 2000, Courtesy of Haiyan Gong). [B] Scanning electron micrograph of the inner wall as seen from inside the canal. The black arrow in the insert points towards a pore formed on the surface of a GV. (Image from Johnson et al. 2006)

To reconcile this paradox, Johnson et al. proposed the “funneling” theory proposing a hydrodynamic interaction between the pores and JCT (Overby et al. 2009). The theory allows that the bulk of outflow resistance still resides within the JCT and basement membrane of the SC cells. However, the pores force the fluid to passing through the regions of JCT that are close to the pores and vacuoles, thereby decreasing the effective flow area (Figure 1.3). In this case, the pore size and density could amplify the resistance generated in JCT by a factor of E that is defined as:

$$E=1+1/(4nRL) \tag{1}$$

where n is pore density (pores per unit area), R is giant vacuole radius, and L is JCT thickness.

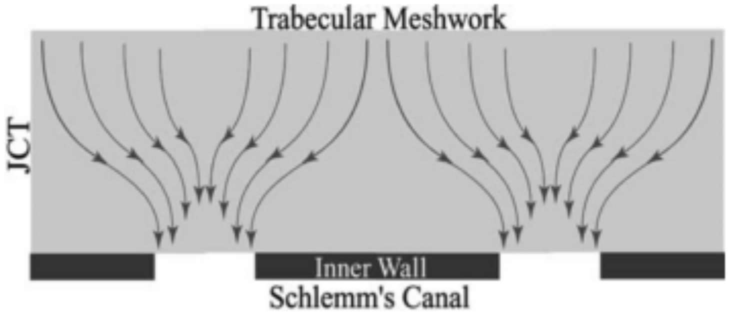

Figure 1.3: Schematic for the funneling effect. The presence of pores forces the fluid funnel through the regions closer to the inner wall. This phenomenon will give pores a regulatory role in homeostasis of the outflow resistance. (Image from Overby 2008)

Previous studies have shown a significantly reduced pore density in the inner wall endothelium of glaucomatous eyes (Allingham & Kater 1992); (Johnson et al. 2002). This is consistent with the funneling theory that predicts a higher outflow resistance when pore density is reduced. As a result, understanding the pore formation process and its homeostasis has been an area of interest in studies for the pathogenesis of glaucoma. In our research we focus on understanding the mechanics of SC endothelial cells and its role in pore formation.

1.4 Altered mechanobiology of Schlemm's Canal endothelial cells in glaucoma

It is widely recognized that many aspects of a cell behavior, including migration, differentiation, proliferation, and signal transduction, are influenced by mechanical properties of the cell and in particular, stiffness (Lautenschläger et al. 2009); (Gasiorowski et al. 2013). Research has provided abundant evidence on the role of altered cell mechanics in progression of a wide range of diseases including cancer (Suresh et al. 2005), malaria (Suresh et al. 2005), arthritis (Carl & Schillers 2008), and asthma (Discher et al. 2009). Hence, understanding the mechanical properties of cells and their regulatory mechanisms are of significant importance in elucidating the pathogenesis of such diseases.

Zhou et al. (Zhou et al. 2012) have shown a positive correlation between the SC cell stiffness (in-vitro) and outflow resistance. This observation initiated the hypothesis that pore formation may involve SC cell mechanics as these cells experience high strain rates (more than 50% (Ethier 2002)) to form giant vacuoles and subsequently pores. To test this hypothesis, Overby et al. perfused cultured monolayers of normal and glaucomatous SC cells in the basal to apical direction and detected pore formation in both cell strains. However, when they characterized pore density, glaucomatous cells had remarkably lower pore density (almost a third) as compared to the normal cells (Overby et al. 2014). They also characterized the mechanics of cortical and subcortical regions in normal and glaucomatous SC cells using atomic force microscope (AFM) sharp and rounded probes as described previously (Vargas-Pinto et al. 2013). Data from AFM revealed an elevated subcortical stiffness in glaucomatous SC cells when compared to normal cells. More importantly, when a correlation was tested between the subcortical stiffness and pore density, a statistically significant inverse relation was found as shown in Figure 1.4. Although this correlation doesn't prove a

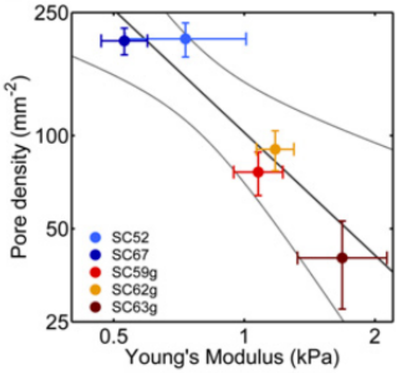

Figure 1.4: Correlation between pore density and subcortical stiffness in SC cells. Glaucomatous cells have higher subcortical stiffness and fewer pores.

causal relationship, it confirms the strong link between SC cell mechanics and pore formation (Overby et al. 2014).

To investigate the mechanism for the elevated stiffness in glaucomatous SC cells, Overby et al. used optical magnetic twisting cytometry (OMTC) to examine the effect of substrate stiffness on the stiffness of cultured SC cells. The incentive for this study was twofold. First, it was previously reported that the stiffness of TM, which is the underlying substrate for SC cells, is significantly higher in glaucomatous eyes (Last et al. 2011) and secondly, the already established fact that tissue cells feel the mechanics of their microenvironment and adjust their mechanobiology accordingly (Discher et al. 2005a). Consistent with the literature, the results showed that both normal and glaucomatous SC cells become stiffer when cultured on stiffer substrates. Importantly, the response from glaucomatous SC cells to increased substrate stiffness was significantly greater than that of SC cells from normal eyes (Overby et al. 2014).

Despite the valuable information provided by the studies from Overby et al., the caveat in these studies is that the elevated subcortical stiffness in glaucomatous cells was detected through in-vitro studies where cells are cultured on plastic substrates that are orders of magnitude stiffer than their actual substrate, TM. Hence, one might argue that such observation might be due to higher sensitivity of glaucomatous SC cells to stiffer plastic substrates and such behavior may be absent in-situ. We know from previous in-situ studies that glaucomatous TMs are stiffer than normal ones (Last et al. 2011). However, the stiffness of SC cells hasn't been examined in-situ to date and this has been the major scope of our work described in this thesis.

1.5 Effect of dexamethasone on outflow facility

Glucocorticoids are a family of steroid hormones that bind to the GC receptors and are involved in metabolic and immunological regulatory system. Among glucocorticoids, dexamethasone has anti-inflammatory properties and is used to treat inflammatory conditions (Jones & Rhee 2006). It has been shown that dexamethasone treatment of the eye can result in ocular hypertension in some individuals (Clark et al. 1995) leading to steroid induced glaucoma (Overby & Bertrand 2014)(Clark & Wordinger 2009), particularly in individuals with a family history of glaucoma (Jones & Rhee 2006). Interestingly, patients who are diagnosed as glaucoma suspects and respond to steroid treatment have increased outflow resistance during the period of steroid treatment and experience reduced resistance and lower IOP when the steroid treatments is ended (Kersey & Broadway 2006).

At the cellular level, dexamethasone can modulate the actomyosin machinery and increase the traction forces in cells (Puig et al. 2007). It can also alter actin cytoskeleton in different cell types including human alveolar epithelial cells (Puig et al. 2007) and TM cells (Clark et al. 2005). A recent study found that dexamethasone treatment significantly increases the stiffness of TM cells and their extracellular matrix (Raghunathan et al. 2015). However, the effect of dexamethasone on the cytoskeletal organization and mechanics of SC cells is not understood as yet.

1.6 Hypothesis and goals

We described the role of pores in regulating outflow resistance in section 1.4, and the relationship between SC cell mechanics and pore density described by Overby et al. (Overby et al. 2014). We also noted the caveat that these studies were done in-vitro and need to be confirmed in-situ. As such, a major focus of our studies was to develop a method to simultaneously characterize the stiffness of SC cells and their underlying substrate in-situ. Our approach has been to extract the inner wall tissue from postmortem human eyes and to use AFM for stiffness measurements. We developed the tissue preparation protocol in collaboration with Dr. Thomas Read at the laboratory of Dr. John Flanagan at Toronto Western Hospital. The appropriate AFM and imaging set up was built in collaboration with Dr. Biqin Dong at the laboratory of Dr. Hao Zhang at Northwestern University.

Our goal from these studies was twofold: first, we sought to replicate the results from Last et al. that TM in glaucomatous eyes is an order of magnitude stiffer than the TM from normal eyes (Last et al. 2011). Secondly, we were interested to see whether there is a difference between the stiffness of normal and glaucomatous cells in-situ. We will discuss the approach and results for AFM measurements in Chapter 3. A significant limitation to the AFM studies was the scarcity of glaucomatous eyes due to their high research demand. During the eight months that this study was conducted, we only procured a single glaucomatous eye and this significantly restricted our conclusions.

The experimental data we obtained from AFM on intact inner wall specimens showed a variable of stiffness patterns in both normal and glaucoma tissues. To interpret these data, we developed a finite element model (FEM), which was able to explain some aspects of the experimental data. The model and results are discussed in detail in Chapter 4.

A secondary focus of our studies was to examine the effect of dexamethasone on the cytoskeletal structure and mechanics of SC cells. We hypothesize that the stiffness of SC cells is increased in steroid induced glaucoma. The foundation for our hypothesis is based on three facts. First, dexamethasone treatment in steroid responsive patients correlates with increased outflow resistance (Clark & Wordinger 2009). Secondly, dexamethasone has been shown to increase the stiffness in several cell types (Puig et al. 2007)(Raghunathan et al. 2015). And finally, there is a strong correlation between the SC cell stiffness and pore density (Overby et al. 2014).

To examine the effect of dexamethasone on the mechanics of SC cells we used AFM, OMTC, and traction force microscopy (TFM). These techniques are described in detail in Chapter 2. All OMTC and TFM studies were conducted by Dr. Chan Young Park at the laboratory of Dr. Fredberg at Harvard University where as AFM studies were done in our lab at Northwestern University. We also conducted imaging studies to monitor cytoskeletal changes in these cells upon dexamethasone treatment.

The AFM studies revealed that dexamethasone while significantly increased the cortical stiffness in SC cells, it did not change the subcortical stiffness. Consistent with what Puig et al. reported for dexamethasone treated alveolar epithelial cells (Puig et al. 2007), TFM studies showed higher traction forces in most dexamethasone treated SC cells. However, when dexamethasone treated SC cells were tested with OMTC, there was a marginally significant drop in cell modulus after treatment. The imaging studies revealed significant changes in F-actin and vimentin distribution in dexamethasone treated SC cells when compared to their controls. Hence, we sought to further understand how altered cytoskeleton can influence the mechanics of these cells by overexpressing Rho A and α-actinin in them. RhoA, a small GTPase of the Rho family, is thought to be the principle regulator of the contractile state of a cell, and thereby a major regulator of cell stiffness (Sit & Manser 2011)(Hotulainen & Lappalainen 2006). It directly activates formins that are involved in the polymerization of actin and activates myosin II by regulating its phosphorylation state through Rho-kinase (Charras et al. 2006). α-actinin acts within a cell to cross-link actin filaments and thus, could modulate cells biomechanical behavior (Jackson et al. 2008) (Ehrlicher et al. 2015). The mutations in alpha actinin have been previously reported to increase the binding affinity of alpha actinin to F-actin in renal podocyte cells and increase the traction forces in these cells leading to a form of kidney damage known as focal segmental glomerulosclerosis (FSGS) (Ehrlicher et al. 2015). Our observations for the effect of RhoA and α-actinin overexpression on SC cell mechanics were similar to that of dexamethasone experiment as explained in chapter 5.

We then examined the role of vimentin in cortical cell mechanics by following the same approach as for the other cytoskeletally-active agents. Vimentin is a type III intermediate filament that is expressed in mesenchymal cells. Our incentive here was previously reported data from Guo et al. who used OMTC to probe the cortical stiffness in wild type (WT) and vimentin knock out (KO) mouse embryonic fibroblasts (MEFs). In their studies, Guo et al. did not detect a difference in OMTC measurements for WT and KO MEFs and concluded that vimentin doesn't play any role in cell cortex mechanics. However, we believed that OMTC might not measure the cortex stiffness. Our AFM results showed that, in contrast to conclusion from Guo et al., WT cells had significantly stiffer cortex as compared to KO cells, which highlighted the role of vimentin in cortex mechanics. However, to our surprise, the OMTC results suggested that KO cells were stiffer than WTs.

To reconcile the difference between the AFM and OMTC in all our studies, we created a finite element model for the probing of cell mechanics using AFM and OMTC to examine the effect of different parameters such as cortex stiffness, indentation/embedding depth, and probe size on the measurements from these techniques. The model of AFM was based on that developed by Vargas-Pinto et al. (Vargas-Pinto et al. 2013) while for OMTC simulations we followed the model of Mijailovic et al. (Mijailovich et al. 2002). The results from these simulations showed a significant effect of cortex stiffness and probe size on AFM measurements. The simulations also demonstrated that OMTC measurements are dependent on the cortex stiffness, subcortical stiffness and, more importantly, on bead embedding depth. Results from the modeling studies offered tentative explanation for the discrepancy between the AFM and OMTC data. Results from all these experiments along with the simulations are presented in Chapter 5.

Chapter 2: Common Techniques and Methods

2.1 Atomic Force Microscopy

2.1.1 Principles of the AFM

The underlying concept of AFM is based on using a laser beam to track the deflection of a probe that is interacting with a sample. An AFM probe consists of two components: a tip that is in contact with the sample and a cantilever, which the tip is mounted on. A piezoelectric actuator moves the probe towards the sample. The laser beam is illuminated on the back of the cantilever and the reflection is collected via a photo detector, which is responsible for monitoring the deflection of the cantilever (See Figure 2.1).

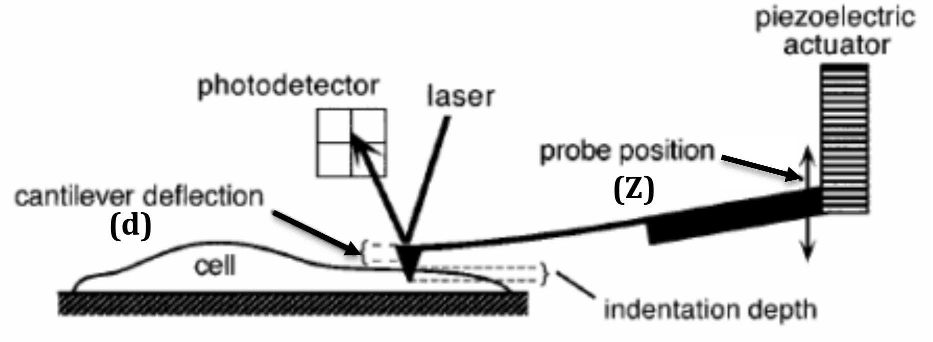

Figure 2.1: The basic components of AFM. (Image adapted from Costa 2006)

AFM can be used for imaging or force measurement purposes and has two operating modes: tapping mode or contact mode. In tapping mode, the tip oscillates in the vicinity of the sample surface while in the contact mode it is fully in contact with the sample surface. The contact mode is usually used for force measurement studies while tapping mode is more suitable for imaging experiments.

2.1.2 AFM force measurements

AFM contact mode is used to characterize the mechanical properties of a wide range of materials including soft materials like cells and tissues. In this mode, the AFM tip is used to indent a sample and then retracted yielding a ramp cycle that includes an extension (tip approaching the sample) and a retraction (tip retracting from the sample) curve. As the probe indents the sample, its deflection (d) is recorded as a function of its translational motion (z) (See Figure 2.1). The deflection can be related to applied force using Hooke's law, F=k*d, where "k" is the spring constant of the cantilever. AFM probes typically have a nominal spring constant, but the actual cantilever constant is determined using a calibration procedure known as "thermal tuning" that is based on the cantilever's mechanical response to thermal agitations from the Brownian motion of its surrounding fluid. The AFM measures the cantilevers fluctuations, as a function of time and a Fourier transform is used to obtain the Power Spectral Density in the frequency domain. A Lorentzian model is then used by the software to determine the spring constant of the cantilever (Hutter & Bechhoefer 1993). In addition to the spring constant, deflection sensitivity is determined by measuring the tip deflection for a given movement of the detection laser on the photo detector. Finally, the Young's Modulus of the sample is obtained by fitting an appropriate theoretical model to the force-indentation curve, the details of which are described in 2.1.4.

The viscoelastic properties of a cell are able to affect the AFM measurements if the tip has high approach or retraction velocity (A-Hassan et al. 1998). To avoid these viscous effects, it is recommended to keep the approach and retraction velocity below 1 µm/s (Carl & Schillers 2008). Hence, tip velocity was set to 800 µm/s for all AFM experiments. The AFM set up for measurements on cells (chapter 5) had a stage heater to keep the temperature of the media constant at 37°C where as the one for tissue measurements (chapter 3) lacked this feature. We measured the spring constant and deflection sensitivity of the cantilever before each experiment.

2.1.3 Cantilever selection and tip geometry

For force spectroscopy studies on cells, we have previously shown that cell stiffness measurements by pyramidal probes (20nm cap radius with a semi-included angle of 36°) are strongly influenced by the cell cortex while larger rounded probes (5µm radius) are much more affected by the subcortical structure of the cells (Vargas-Pinto et al. 2013). This is due to the fact that the strain field created by an AFM sharp probe is very localized and is mostly confined to the cortex while the rounded probe creates a much larger field that spreads throughout both the cell cortex and the underlying cytoplasm.

AFM tips can be mounted on cantilevers with different spring constants. Choosing the appropriate cantilever depends on the stiffness of the examined sample. It is recommended to use cantilevers of 0.01-0.1 N/m when probing soft biological material like cells and tissues (Costa 2006).

For our tissue mechanics studies described in chapter 3, we used rounded probes (Novascan Technologies, Ames, Iowa) with nominal diameter of 10μm mounted on a silicon nitride cantilever with nominal spring constant of 0.06 N/m.

For the cell biomechanics studies in chapter 5, we used both pyramidal (sharp) and rounded probes to characterize the cortical and subcortical stiffness of the cells as previously described (Vargas-Pinto et al. 2013). The pyramidal cantilevers were mounted on a 200 μm triangular cantilever with a nominal spring constant of 0.02 N/m (Olympus TR400PSA, Asylum Research, Goleta, CA). For rounded probes, 10μm spheres mounted on silicon nitride cantilevers with nominal spring constant of 0.01 N/m (Novascan Technologies, Ames, Iowa) were used.

2.1.4 Indentation data analysis and Young's Modulus extraction

Data from AFM measurements is in the form of tip deflection (d) as a function of the distance it travels (z). The indentation, δ, which is the net distance the tip indents into the

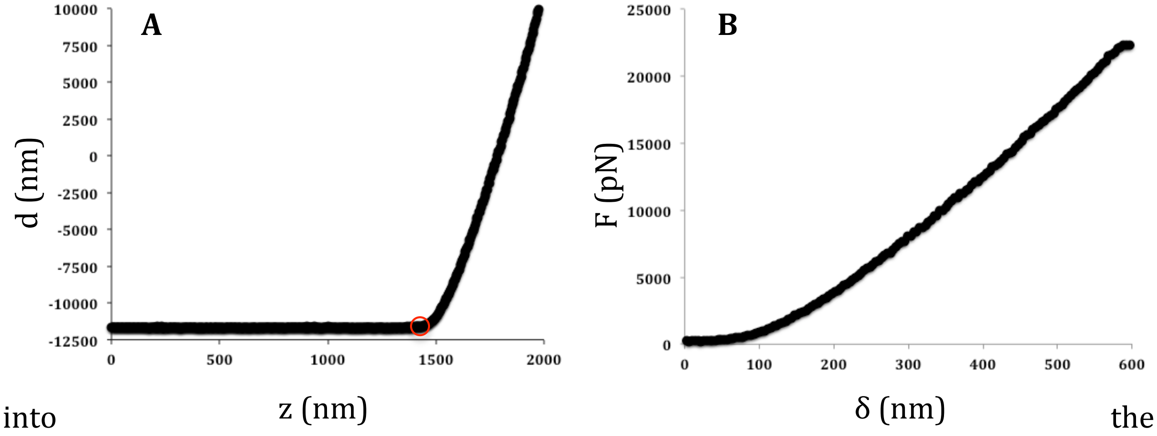

Figure 2.2: Example of the data from the AFM. [A] The tip deflection (d) is plotted as a function of translation (z) and a red circle marks contact point. **[B]** The contact point is translated to the origin and force (F) is plotted as a function of indentation (δ).

sample is then defined as $\delta = (z-z_0) - (d-d_0)$, where z_0 is the probe position in the z direction at the contact point and d_0 is the deflection of the tip at the initial contact point (Weissenhorn et al. 1993) (Figure 2.1). We used a method proposed by Crick and Yin to determine the initial contact point (z_0, d_0) (Crick & Yin 2007) and the indentation force (F) was calculated using Hooke's law as described in 2.1.2 (Figure 2.2).

The force measurements (F) as a function of indentation (δ) are used to calculate the Young's Modulus, E, as follows. Two different models are used that depend on the geometry of the tip. For the rounded probes, the Hertz model is frequently used (Dimitriadis et al. 2002). In this model, a rigid sphere indents a homogeneous, isotropic, linear elastic, semi-infinite half space and the indentation is assumed to be infinitesimal, frictionless, with no adhesion effects between the tip and the sample with the result that:.

$$F = \frac{4E\sqrt{R}}{3\ (1-\nu^2)}\delta^{3/2} \qquad (1)$$

where F= force, δ = indentation, E= Young's Modulus, ν = Poisson's ratio, R= tip radius.

To analyze the measurements from sharp (pyramidal) probes, we used a model for a blunt tip (Rico et al. 2005) as:

$$\mathrm{F} = \frac{2\mathrm{E}}{1-\upsilon^2}\left(\mathrm{a}\delta - \mathrm{m}\frac{\mathrm{a}^2}{\tan\theta}\left[\frac{\pi}{2} - \sin^{-1}\left(\frac{\mathrm{b}}{\mathrm{a}}\right)\right] - \frac{\mathrm{a}^3}{3\mathrm{R}} + \sqrt{\mathrm{a}^2-\mathrm{b}^2}\left[\frac{\mathrm{mb}}{\tan\theta} + \frac{\mathrm{a}^2-\mathrm{b}^2}{3\mathrm{R}}\right]\right) \qquad (2a)$$

where

$$\delta = \frac{a}{R}\left(a - \sqrt{a^2 - b^2}\right) + \frac{na}{\tan\theta}\left[\frac{\pi}{2} - \sin^{-1}\left(\frac{b}{a}\right)\right], \tag{2b}$$

instead of the classical model (Rico et al. 2005) where:

$$F = \frac{1.4906E\tan\theta}{2(1-\upsilon^2)}\delta^2 \tag{3}$$

with F=force, δ=indentation, E= Young's Modulus, ν=Poisson's ratio, θ=semi-included angle, R=spherical tip radius, b=R*cosθ, a=contact radius. For pyramids, m=√2/π and n=2√2/π (Lin et al. 2007). Equations (2) more realistically account for the geometry of a pyramidal tips as they don't have an exact pyramidal profile but instead, have a small rounded tip that smoothly extends to a tapered body as shown in Figure 2.3.

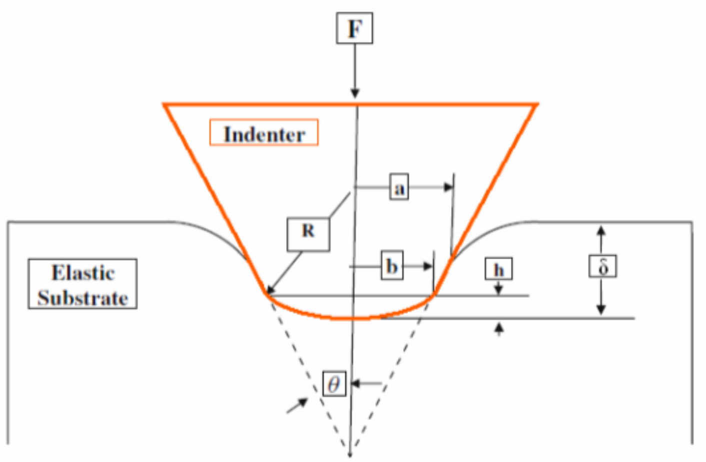

Figure 2.3: The actual profile of an AFM sharp probe indenting an elastic body. The probe has a pyramidal profile with a transition to a small sphere (R=20nm) at the tip. Image from Crick and Yin (2007).

Equation 2 applies the Hertz model to the points prior to the point of transition and incorporates a revised model for ideal pyramid (Eq. 3) for indentations that are larger than tip radius. Rico et al. (2005) indicated that use of this model should yield a modulus, E, relatively independent of indentation depth for linear elastic material, a claim we verified in our own studies (Rico et al. 2005).

In all of our studies, we assumed the tissue to be incompressible (ν=0.5), (Humphrey 2002)) and only the extension force curve was used to determine E as opposed to the retraction curve as the latter would be affected by adhesion forces between the AFM tip and the cell or tissue surface (Lin et al. 2007).

2.2 Optical Magnetic Twisting Cytometry (OMTC)

2.2.1 Background

Optical magnetic twisting cytometry is a technique that is used to probe the mechanical properties of the cells in which a torque (T) is applied to a ferromagnetic bead that is bound to the surface of the cell and the lateral translation of the bead, d, is recorded using a phase-synchronized video camera (Mijailovich et al. 2002) (Figure 2.4). The ratio of the applied torque to the bead displacement defines a modulus per unit length, g, with a unit of Pa/nm. This modulus can be then translated to the traditional shear modulus, G, using a geometric factor, β, as G= βg. The geometric factor (β) has the unit of length, depends on cell geometry and the bead embedding depth, and can be calculated using finite element models (Fabry et al. 2003).

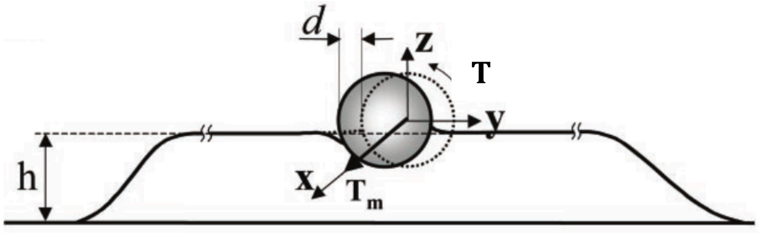

Figure 2.4: Schematic of the OMTC. Image from Mijailovic (2002).

2.2.2 Experimental methods

Ferromagnetic beads can bind to cells through two different methods. First, the beads can be coated with a synthetic peptide containing the sequence RGD (Arg-Gly-Asp). In this method the bead associates with the cell surface receptors, induces the assembly of the focal adhesions complexes (Wang et al. 1993), and recruits cytoskeletal proteins to the attachment site (Deng et al. 2004). Hence, it is believed that the RGD-coated ferromagnetic beads transmit the applied torque at the surface to the internal cytoskeleton and consequently probed deep inside the cell (Coughlin et al. 2006). Also, it is shown that the activation of integrins can alter cytoskeletal organization and affect cell stiffness or morphology (Na et al. 2008), which can introduce artifacts to the OMTC measurements.

The second binding method is based on coating the beads with poly-L-lysine (PLL). PLL binds to the cell surface through electrostatic forces and is none specific and integrin independent (Coughlin et al. 2006). Also, PLL binding does not induce the focal adhesion complex formation or cytoskeletal protein recruitment (Riveline et al. 2001). As a result, PLL coated beads are assumed to probe only the cortex, but not the internal cytoskeleton of the cell (Coughlin et al. 2006).

All OMTC studies described in this thesis were conducted by Dr. Chan Park in the Fredberg labortory at the Harvard School of Public Health. PLL coated beads were used in all experiments to bind the magnetic beads to the cells except in the experiments on mouse embryonic fibroblasts in which some experiments instead used RGD. The bead preparation, incubation, magnetization, and twisting was done following the detailed protocols described in the literature (Guo et al. 2013)(Fabry et al. 2003). For all experiments, cells were seeded to 96 well plates (Thermo Fischer Scientific, Grand Island, NY) and kept in the proper culture media (see 5.2.1) at 37°C. All measurements were done at a single frequency of 0.78Hz. Also, since the embedding depth was not measured in these studies, the results and conclusions are based on the modulus per unit length (g) rather than the absolute shear modulus (G).

2.3 Traction Force Microscopy (TFM)

2.3.1 Background

TFM is an experimental technique that is used to measure the traction forces in a cell. In this technique, cells are plated on a transparent substrate embedded with fluorescent microspheres. The traction forces from the cell will result in displacement of microspheres and a fluorescent/confocal microscope is used to record the microsphere displacement from the initial position (Figure 2.5). The displacement field along with the substrate stiffness and cell contour is then used to calculate the constrained traction field. Finally, the constrained traction field is used to calculate a scalar measure of cell contractility called the root mean square (RMS) traction (Butler et al. 2002).

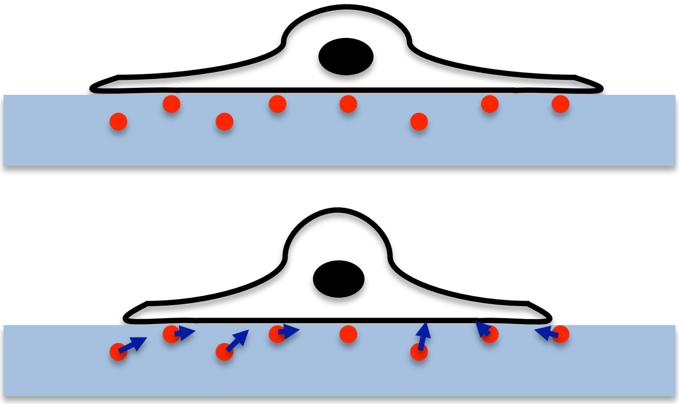

Figure 2.5: Schematic of the TFM with a cell plated on a hydrogel embedded with fluorescent microspheres. The schematic shows the location of the spheres before (top) and after (bottom) displacement by traction forces from the cell.

2.3.2 Experimental Methods

Different types of natural and synthetic hydrogels can be used to fabricate the substrate for TFM experiments, with polyacrylamide gels a frequent choice. The polyacrylamide gels are biocompatible and their stiffness can be adjusted to the desired levels by changing the concentration of the cross linker, bisacrylamide. All TFM studies were conducted by Dr. Chan Park and polyacrylamide gels were used as the substrate for all TFM experiments. The procedure for gel preparation and activation has been described in detail elsewhere (Zhou et al. 2012). Cell were seeded to 96 well plates (Thermo Fischer Scientific, Grand Island, NY) and seeding density and substrate stiffness varied among the experiments (see methods section in chapter 5). A Leica epifluorescent microscope was used to determine the location of the microspheres before and at the end of the experiments. The displacement field was then calculated using these images and RMS traction was extracted as described in 2.3.1.

2.4 Finite Element Modeling (FEM)

In our studies, FEM is used to model both AFM and OMTC. In chapter 4, it is described how FEM is used to simulate our in-situ AFM rounded probe measurements of the stiffness of SC cells and that of the substrate underlying these cells (their basement membrane and the JCT). In chapter 5, it is described how OMTC is simulated when a bead is bound to an SC cell in culture on a rigid substrate with a stiffer cortex and softer cytoplasm. It is also described in chapter 5 how FEM is used to examine the effect of tip size on AFM measurements on SC cell in culture on a rigid substrate with a stiffer cortex and softer cytoplasm.

We used ABAQUS/CAE 6.13 finite element software to create the model for our studies (Simulia, Providence, RI). The finite element analysis in ABAQUS can be done through either implicit or explicit schemes. When a model is submitted to ABAQUS for analysis, the software divides the solution process into arbitrary time increments. The explicit scheme uses the current state of the system to calculate the later state and is based on the central difference method. On the other hand, the implicit method iteratively solves an equilibrium equation, which includes both the current and later state of the system at each increment. While in general the implicit scheme is favored in solving quasi-static problems, like ours, the explicit scheme tends to be computationally less expensive and is more preferred for analysis of loading conditions involving contact and deformation (Harewood & McHugh 2007). Therefore we used the explicit scheme for all of our finite element analysis (Harewood & McHugh 2007).

The ideally symmetrical indentation of AFM probe on the tissue allowed us to use an axisymmetric model instead of 3D where all cell and tissue components were modeled as discs and the plane of symmetry was defined using the revolution axis of the probe. For OMTC modeling, we used a 3D geometry and cell was modeled as a bilayer cylinder. The radius of the discs/cylinder was determined such that the strain at the edge of the domain was less than 0.1% of the maximum strain near the probe. Cell and tissue components were assumed as homogeneous elastic incompressible materials (Mijailovich et al. 2002) where as AFM and OMTC probes were modeled as rigid spheres (Costa & Yin 1999). The Young's modulus of the cytoplasm was 3kPa (Mijailovich et al. 2002) and cortex thickness was 400nm as measured previously (Vargas-Pinto et al. 2013).

For all cases, interaction between the probe and the cortex was set to be no-slip (Mijailovich et al. 2002). No predefined stress field was assigned to any of the components and the domain side boundaries were allowed to move freely.

4-node bilinear axisymmetric quadrilateral elements were used to discretize the components. In order to create a finer mesh around the probe region, which is the region with highest deformed elements, and also to shorten the computational time, a bias factor was introduced to elements length (radial direction) in all components.

The introduction of bias factor leads to a gradual increase in size of elements that are further from the probe. The approach to determine the mesh size and bias ratio was to systematically reduce the size until the results became independent of the element size.

The apparent modulus, $E_{apparent}$, was defined as an average modulus for the cell as if it were homogeneous and behaved the same way as it did when cortex and cytoplasm had different Young's Modulus. To calculate $E_{apparent}$ for AFM, the reaction force of the probe and the indentation values were extracted from ABAQUS for each case. Then, the Hertzian model for spherical contact (see 2.1.4) was used assuming that the material was homogenous. For OMTC, ABAQUS was used to calculate $E_{apparent}$ since there is no exact solution for the bead rotation problem. To do so, the case in which the cortex and cytoplasm have equal modulus (3kPa) was taken as the baseline and the bead center displacement was measured. Then, the corresponding torque that would cause the same displacement for other cases where $E_{cortex} \neq E_{cytoplasm}$ was found. Finally, those corresponding torques were used to calculate $E_{apparent}$ for each case.

2.5 Statistical Data Analysis

To examine for a significant difference between the averages of two samples, Student's t-test assuming unequal variances was used at the significance level of 0.05. Also, to compare more than two averages, we used ANOVA at the significant level of 0.05. To examine for the relation between a dependent variable and multiple explanatory variables, standard linear regression with a significance level of 0.05 was used. Finally, a Z-test (significance level 0.05) was used to examine whether an average value was drawn from a certain population.

The statistical tests used in our studies assume a normal distribution for the data. We have previously shown that data from AFM measurements is not normally distributed and a logarithmic transformation is required to make the distribution normal (Overby et al. 2014). As a result, all AFM data was logarithmically transformed before mean calculation and statistical analysis. The mean was the calculated and AFM is reported as geometric means ± standard error around the geometric mean. Data for OMTC is collected from many beads that are attached to cell surface. This increases the variability in measurements and might cause the mean to be skewed by excessively large or small values. To overcome this issue, OMTC values are presented as median ± median absolute deviation, where the median absolute deviation is defined as the median of the absolute deviations from data's median. Finally, data for TFM is presented as mean of RMS ± standard deviation of RMS around the mean.

Chapter 3: In-Situ Stiffness Characterization of the Inner Wall Endothelium of Schlemm's Canal and its Substrate

3.1 Overview

Altered cell and tissue mechanics is a hallmark for the progression of many types of diseases. As a result, understanding the mechanics of cells and tissues and their homeostasis is crucial in understanding the pathogenesis of such diseases and development of effective therapeutics for them.

It has been suggested that the mechanobiology of SC cells is altered in glaucoma where they show elevated stiffness in subcortical region when tested in-vitro (Overby et al. 2014). Other groups have shown an elevated stiffness for the TM in glaucoma (Last et al. 2011), which underlies the basement membrane of the SC cells. It is possible that the elevated stiffness of SC cells in glaucoma is related to the increased stiffness of the glaucomatous TM (Russell & Johnson 2012), since it has been shown previously that cells feel and respond to mechanics of their substrate (Discher et al. 2005b). However, the SC cell mechanics have only been examined in-vitro and there has as yet been no study on the interaction between the mechanics of the SC cells and their substrate in-situ.

The goal of this work described in this chapter was to use AFM to examine the stiffness of normal and glaucomatous SC cells in-situ, and to also probe their substrate. We had two aims. First, we aimed to see whether our previous in-vitro observations on the elevated stiffness of glaucomatous SC cells could be confirmed in-situ. Secondly, we looked to confirm the previous reported results showing that

TM is significantly stiffer in glaucomatous eyes; confirmation of this latter conclusion was important because an artifact was identified in the technique used by the group that reported it (Last et al. 2011). We will discuss this artifact in section 3.2.3. In Chapter 4, we describe use of a finite element model (FEM) to simulate the AFM experiments and thereby examine the effect of cell cortex and substrate stiffness on the AFM measurements.

3.2 Methods

We sought to characterize the stiffness of SC cells and their underlying substrate in-situ. To do so, we used post mortem human eyes and dissected them to extract the inner wall tissue. We then used a fluorescent stain to mark and visualized SC cells on the tissue and used AFM to measure the stiffness of different regions of the tissue.

3.2.1 Human eyes

Postmortem human eyes were received from Illinois Eversight Eye bank and the laboratory of Dr. Stamer[1]. The eyes were procured within 12 hours of death, placed on buffer saline soaked gauze in sealed jars. The jar was placed in a sealed plastic bag chilled on a sealed bag of regular ice and arrived in our lab within 24 hours after death. All globes had at least 1cm of the optic nerve in tact. The characteristics of these globes can be found in Table 3.1. Upon arrival in our laboratory, globes were disinfected in 150ppm Wescodine® solution (Steris, Libertyville, IL) for 5 minutes

---

[1] Stamer lab received these globes from Miracle In Sight eye bank in North Carolina

and rinsed for 3 minutes twice with 0.9% sodium chloride irrigation solution (Baxter, Deerfield, IL).

Table 3.1: Specifications for human eye globes used in our studies.

Tissue ID	**Source**	**Cause of Death**	**Death Date-Time**	**Death-Procurement interval**	**Death-experiment interval**	**Age**	**Gender**	**Normal or Glaucoma**
G-M244638-OS	Eversight	Metastatic lung cancer	09/23/2015 23:49	4h41m	29h50m	55	F	N
2411-15-01 (OS)	Miracle In Sight	Multi system organ failure	9/28/2015 5:17	5h	9h58m	80	F	N
2411-15-01 (OD)	Miracle In Sight	Multi system organ failure	9/28/2015 5:17	5h	27h13m	80	F	N
2633-15-01 (OS)	Miracle In Sight	Anoxia	10/21/2015 10:57	3h38m	15h3m	83	F	N
2633-15-01 (OD)	Miracle In Sight	Anoxia	10/21/2015 10:57	3h38m	21h50m	83	F	N
G-M247220-OS	Eversight	Pulmonary embolism	11/04/2015 18:24	6h26m	23h36m	66	F	N
W4035-V0183000	Eversight	Myocardial infarction	01/05/2016 17:11	6h48m	25h30m	60	F	N
W4035-V0182000	Eversight	Lung cancer	02/09/2016 17:06	6h39m	22h40m	59	M	N
W4035-V0180000	Eversight	Myocardial infarction	02/14/2016 20:37	11h21m	23h16m	69	M	N
W4036-V0180000	Eversight	Aneurysm	04/07/2016 14:56	5h34m	23h4m	88	M	*G

* The glaucoma donor had bilateral cataract surgery with intraocular lens implants in 2010 and used travatan and brimonidine eye drops.

3.2.2 Perfusion methods

To further verify the status of the eye (normal or glaucoma), some of the globes were perfused to measure the outflow facility right after disinfected (see Appendix for results). This was only done for the last two normal globes we received and the only glaucomatous globe. Perfusions were done at 10mmHg for 30 minutes using the human eye perfusion protocol established in our laboratory (see Appendix). Figure 3.1 shows typical data from perfusion for a normal eye.

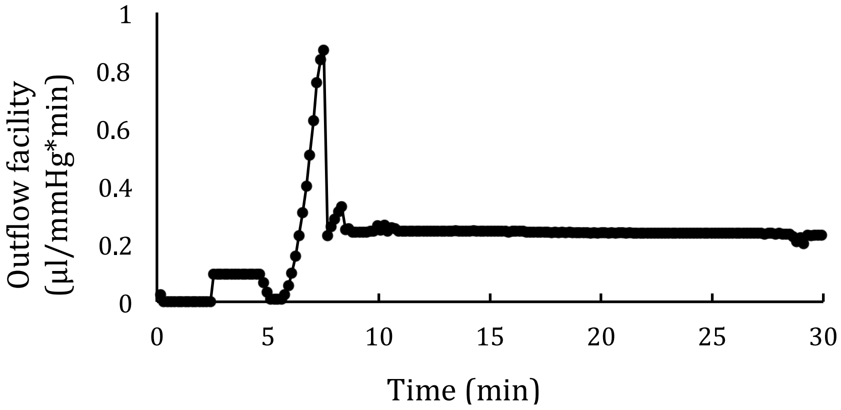

Figure 3.1: Plot for outflow resistance of a normal human eye (W4035-V0180000) perfused at 10mmHg for 30 minutes.

3.2.3 Dissection and sample preparation

The globe dissection and inner wall (IW) extraction was done based on a protocol developed in collaboration with Dr. Thomas Read at the laboratory of Dr. John Flanagan at Toronto Western Hospital (see Appendix). In all cases, the anterior segment of the globes were dissected into 4 quadrants: one quadrant was stored in CO_2 independent media (Thermo Fischer Scientific, Grand Island, NY) containing 10% Fetal Bovine Serum (FBS) (Atlanta Biologicals, Norcross, GA) and 1% Penicillin

Streptomycin (Thermo Fischer Scientific, Grand Island, NY) to prepare the sample for the AFM experiment, one quadrant was fixed in 2% formaldehyde and 2.5% glutaraldehyde (PH 7.4) for SEM studies, and two quadrants were stored in 4% paraformaldehyde (PH 7.4) for immunostaining and light microscopy studies. The optic nerve was stored in 2% formaldehyde and 2.5% glutaraldehyde (PH 7.4) for optic nerve counting studies conducted at the laboratory of Dr. Ernst Tamm at University of Regensburg. Thus far, the optic nerve counting is done on five normal globes and the one glaucomatous globe (see Appendix). Also, to make the best use of our only glaucoma globe, a larger piece of the quadrant was used for sample preparation (almost 3 times bigger) and more measurements were done on that sample as compared to typical sample size and number of measurements for the normal samples (see Appendix for sampling details).

3.2.4 Immobilization and staining

AFM measurements on biological samples need be conducted in an aqueous environment to preserve tissue properties. However, submerging small tissues in media results makes AFM measurements difficult as the tissue can move during the measurement. People have previously proposed different methods to overcome this challenge (Last et al. 2011). These techniques have included direct or indirect application of strong adhesives that potentially can change the mechanical properties of the probed samples significantly (Morgan et al. 2014). To avoid the potential side effects from application of adhesives, we mounted inner wall tissue samples on positively charged SuperflostPlus Gold slides (Thermo Fischer Scientific, Grand Island, NY) where the SC side of the tissue with cells on its surface was facing up[2]. The positively charged surface of the slide facilitates electrostatic adhesion between the negatively charged tissue and the slide; offers an adhesive free immobilization.

To allow for efficient adhesion, no media was added to the tissue for the first minute and then the tissue was then covered with 200µl of CO_2 independent media containing 10% (FBS) and 1% Penicillin Streptomycin.

We next stained the tissue with a nucleus marker in live cell to locate SC cells as described in 3.3.3. To do so, one drop of cell nucleus stain, NucRed™ Live 647 (Thermo Fischer Scientific, Grand Island, NY), was added to 500µl of CO_2 independent media containing 10% (FBS) and 1% Penicillin and the solution was used to cover the tissue for one hour at room temperature (manufacturer suggests a concentration of 2 drops/ml). The tissue was then rinsed with Dulbecco's phosphate buffer saline (DPBS) (Thermo Fischer Scientific, Grand Island, NY) for 3 minutes twice and covered with 200µl of CO_2 independent media containing 10% FBS and 1% Penicillin Streptomycin.

3.2.5 Tissue visualization and AFM measurements

AFM measurements were done at the laboratory of Dr. Hao Zhang at Northwestern University. Dr. Biqin Dong installed an upright home-built optical fluorescence

---

[2] We thank Dr. Ross Ethier at Georgia Tech for his suggestion on using Superflost slides.

microscope on a BioScope Catalyst BioAFM (Bruker, MA). As described in 3.3.3, a mercury lamp illuminated the tissue from the bottom and a 648nm band pass filter was used to exclude autofluorescence from the tissue. The illuminated sample was imaged by an ultra-long working distance 10x objective lens and an EM-cooled camera placed above the AFM for multi-contrast optical imaging. The plane of focus was manually adjusted to the top surface of the tissue to visualize the cells. The visualized tissue included regions with and without fluorescent signals (see Figure 3.6). In theory, the bright regions represent cell nucleus whereas dark regions are cell periphery or matrix areas; however, as we were at low magnification, the bright regions were cellular and dark regions, bare matrix, where cells likely had been removed in tissue preparations, or were regions of minimal staining. Indentations were performed in fluorescent (bright) and non-fluorescent (dark) regions at ramp sizes of 500nm, 1000nm, and most frequently, 2000nm to characterize the stiffness of both cell and matrix. The rationale for increasing ramp size was to further indent into the tissue to characterize the deeper substrate underneath SC cells. For all experiments, we used rounded probes (Novascan Technologies, Ames, Iowa) with nominal diameter of 10μm mounted on a silicon nitride cantilever with nominal spring constant of 0.06 N/m. The deflection sensitivity and spring constant were calibrated before each experiment as described in 2.1.2.

3.3 Preliminary Studies

3.3.1 Immunostain and SEM studies of the extracted tissue

To verify whether the inner wall has been exposed as intended and has remained intact after dissection, the extracted tissue was visualized under confocal and electron microscopes. For SEM, samples were fixed in 2% formaldehyde and 2.5% glutaraldehyde (pH 7.4) and prepared according to standard protocols (Leonard et al. 2012) and a Hitachi S3400N SEM was used to image the tissue. For confocal microscopy, the tissue was fixed in 4% paraformaldehyde solution, then rinsed with PBS twice and permeabilized with 0.2% Triton (Life Technologies, Grand Island, NY) for 5 minutes, then rinsed again with PBS twice. Afterwards, the tissue was stained for F-actin (60 minutes incubation with three volume per test of Alexa Fluor® 568 Phalloidin, Life Technologies, Grand Island, NY) and nucleus (30 minutes incubation with Hoechst 33342 (1:10000), Thermo Fischer Scientific, Grand Island, MA). The stained tissue was then mounted on microscope glass slides (Thermo Fischer Scientific, Grand Island, NY) using 10μl of fluorescence mounting medium (Dako, Carpinteria, CA) where the inner wall was facing up and a glass cover slip (22×22 No. 1.5, Thermo Fischer Scientific, MA) was placed on the tissue. The slide was cured in the dark at 4°C for 24 hours and afterwards the edge was covered with nail polish (Electron Microscopy Sciences, Hatfield, PA) and cured again in the dark at 4°C for one day. A two-photon confocal microscope with 63x oil immersion objective lens was used to image the tissue (Carl Zeiss, Thornwood, NY). Figure 3.2 shows typical results from scanning electron ([A]-[C]) and confocal [D] microscopy of the extracted IW tissue.

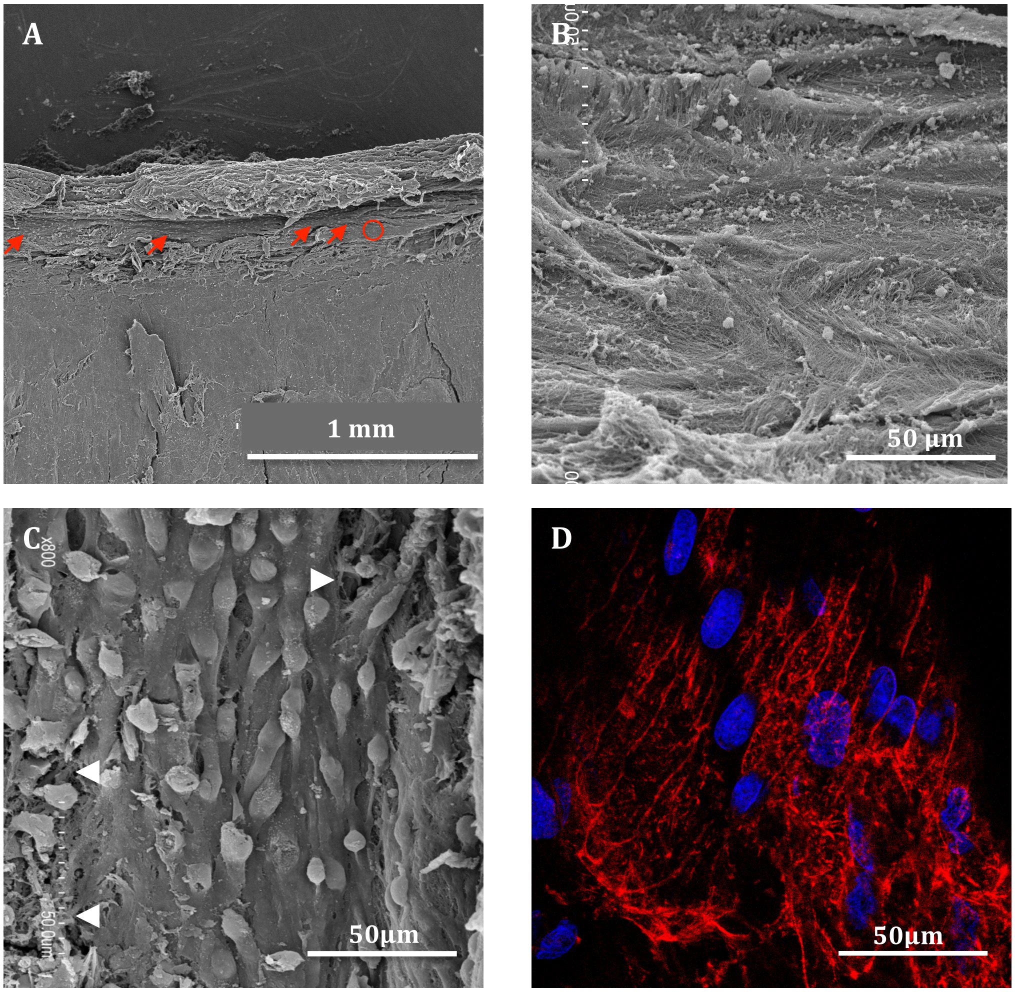

Figure 3.2: Scanning electron micrograph ([A]-[C]) and immunofluorescence image from confocal microscopy [D] of an extracted inner wall. The electron micrographs confirm the efficiency of the extraction technique [A], indicate the likelihood of cell detachment and removal during tissue extraction or sample preparation [B], and the possibility of tears upon tissue extraction [C] (white arrows). The confocal image demonstrates the same pattern as electron micrograph. Nuclei are blue and F-actin (red) shows a prominent cortex at the cell boundary.

The electron microscopy studies confirm that we successfully exposed the IW where SC cells can be located on the tissue (see red arrows in [A]). In addition, SEM results in [B] indicate the presence of regions with only matrix (see red circle in [A]), where the inner wall should be lined with SC cells. This artifact was presumably caused during tissue extraction. Finally, results in [C] shows a region covered with SC cells and demonstrates the possibility of tears in the tissue during tissue extraction and/or sample preparation (see white arrows). Data from confocal microscopy confirmed cell pattern in [C].

3.3.2 Stain selection and visualization set up

The primary purpose of stain selection studies was to come up with an approach that would allow us to mark SC cells and distinguish them from other cells and from their matrix. We first sought to stain SC cells and locate them on the tissue. Here, a major challenge was that there are several types of cells in the IW region (TM, JCT and SC cells and also cells of neighboring tissues), which means that to strain SC cells along, a specific SC marker who fluorescent signal would not be masked by background fluorescence from other cell types in the tissue. We examined the possibility of using CD31 that is a specific marker for endothelial cells as it is reported to be expressed in SC cells, but not TM cells in-situ (Stamer & Roberts 1998). To test the capability of CD31 for marking SC cells, these cells were seeded into two petri dishes (μ-Dish^{35mm,low,} bidi USA, Madison, WI) containing 600μl SC cell standard media (DMEM/Low glucose; Life Technologies, Grand Island, NY) with 10% fetal bovine serum (Atlanta Biologicals, Norcross, GA) and 1% penicillin/streptomycin (Life Technologies, Grand Island, NY)) and incubated for 24 hours. Afterwards, the two petri dishes were incubated with CD31 antibody (clone JC70A, 1:20) (Dako, Carpinteria, CA) for 4 hours and overnight respectively. Samples were then rinsed with DPBS twice and incubated with fresh SC cell standard media containing Alexafluor 647 (1:400) (Thermo Fischer Scientific, Grand Island, NY) for one hour and consequently with the nucleus stain, (Hoechst 33342 (1:10000), Thermo Fischer Scientific, Grand Island, MA), for 15 minutes. Cells were then rinsed with PBS and fresh media was added to each dish. Confocal microscope was used to visualize the cells.

As shown in the Figure 3.3, the signal intensity increased with incubation time. However, even in the overnight-incubated dish, the signal was relatively weak and the experimental visualization set up was not able to detect it. The weak signal intensity from cultured SC cells is consistent with the literature that notes these cells may stop expressing CD31 in-vitro (Stamer & Roberts 1998).

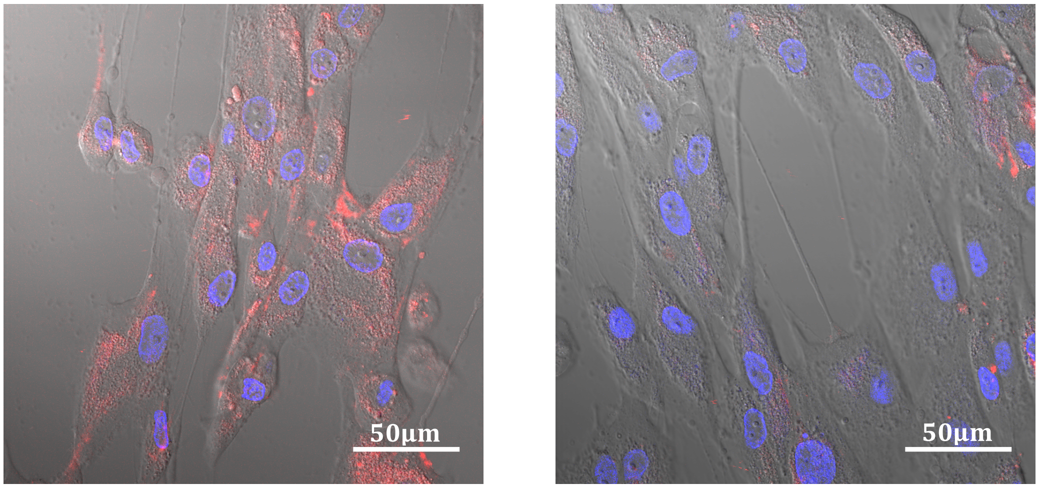

Figure 3.3: Projected confocal and phase contrast images for cultured SC cells incubated with CD31 (red) for 24 hours (left) and 4 hours (right). The nuclei are stained in blue and CD31 is red.

We next aimed to stain live SC cells for CD31 in-situ as they are shown to abundantly express CD31 in-situ (Read et al. 2006). A fresh piece of inner wall tissue was incubated with CD31 antibody for 4 hours (1:20) (clone JC70A, 1:20) (Dako, Carpinteria, CA) inside the incubator and then incubated with Alexafluor 647 (1:400) (Thermo Fischer Scientific, Grand Island, NY) for one more hour. When checked under a confocal microscope, the signal was still weak. Our speculation was that while CD31 is a membrane protein, the epitopes targeted by stains could still lie under the plasma membrane, which inhibits antibody's access to intracellular region in live and non-permeabilized cells. The rational for this speculation was that all previous immunostaining studies that successfully stained CD31 for SC cells in-situ were done on fixed and permeabilized, but not live cells. To test this, a piece of inner wall tissue was fixed in 4% paraformaldehyde, permeabilized with 0.2% Triton (Life Technologies, Grand Island, NY) for 5 minutes and then blocked in 10% normal goat serum (Life Technologies, Grand Island, NY) for 20 minutes to block for the non-specific binding prior to incubation with CD31. The tissue was then incubated with CD31 overnight and then with Alexafluor 647 (1:400) and Hoechst 33342 (1:10000) for one more hour. As shown in Figure 3.4, this time, the fluorescent intensity was significantly stronger indicating that CD31 is abundantly expressed in SC cells in-situ, though not accessible when cells are live and are not permeabilized.

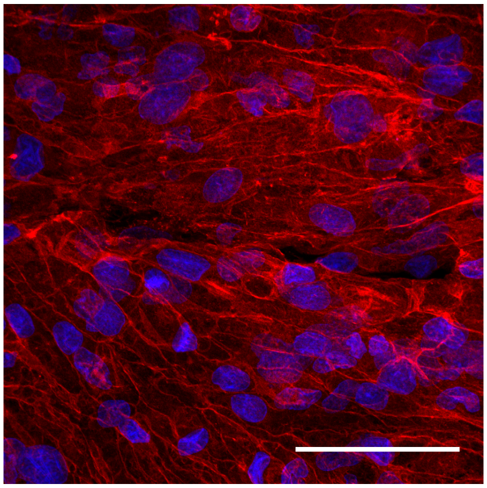

Figure 3.4: Results for immunostaining of a fixed and permeabilized inner wall tissue for nucleus (blue) and CD31 (red). The image shows a significant presence for CD31 in fixed and permeabilized SC cells in-situ.

We then chose to examine the possibility of using a nuclear stain to identify the SC cells. Nuclear stains require short incubation times and can be effectively used on both fixed and live cells (Molecular Probes™ 2010). While this should work to allow us to identify regions of the inner wall where the SC cells were relatively intact, this technique would label all cells in the sample. However, since SC cells lie on top of the sample, our goal as to have the focal plane of the microscope on this top layer to ensure that the fluorescent cells visualized were on this top layer (and thus were not TM or JCT cells deeper in the tissue).

A possible confounding factor that could make it more difficult to localize SC cells was tissue autofluorescence that is caused mainly by the fibrous elements in the extracellular matrix, particularly collagen. Collagen has an autofluorescence spectrum with highest intensity between 350 and 550nm (Wessendorf 2004). As a result, we chose a cell permeable nuclear stain with excitation/emission wavelength of 638/686 (NucRed™ Live 647) (Thermo Fischer Scientific, Grand Island, NY) to avoid this interference.

To examine whether NucRed™ Live 647 was effective for our experiments, the nucleus in live SC cells were stained both in culture and in-situ and visualized using our experimental set up in Dr. Zhang's laboratory. The primary visualization set up had a 633nm Helium-neon laser as the illumination source and a 647 band pass filter (the filter would only pass wavelengths higher than 647nm). To detect SC cells in-situ, the plane of focus was adjusted to the surface of the tissue. Figure 3.5 shows the visualization results for stained cells in culture and in-situ. Red circles mark the illuminated regions in wide field ([A], [C]) and fluorescent ([B], [D]) imaging modes. The Figure demonstrates that the stain effectively marks the nuclei of SC cells (both in-vitro and in-situ) and the imaging set up is capable to detect the signal (see [B] and [D]).

However, as marked by red circles in Figure 3.5, the field of view was too small relative to the size of the tissue/culture dish when using a laser as illumination source. This limited our control over the location of measurements with respect to the entire tissue size. To address this limitation and expand the field, the illumination source was changed from the laser to a mercury lamp and a 647-band pass filter was used to block out the autofluorescence effects.

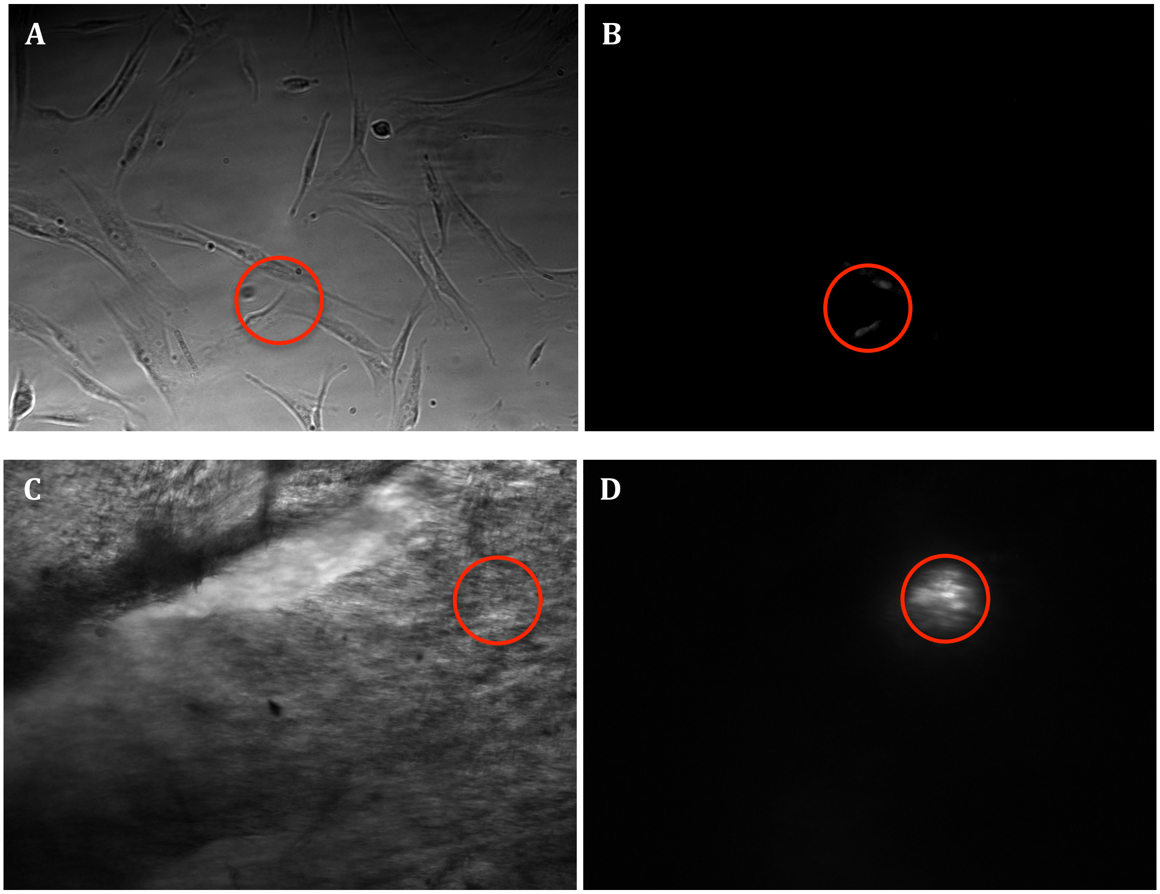

Figure 3.5: Visualization of nucleui for SC cells in culture ([A], [B]) and in-situ ([C], [D]) using NucRed™ Live 647. Red circles mark illuminated regions in wide filed ([A], [C]) and fluorescent ([B], [D]) imaging modes. The images show that NucRed™ Live 647 can efficiently stain the nucleus in SC cells ([B], [D]) and that our experimental set up is capable of detecting the fluorescent signal.

Figure 3.6 shows a stained inner wall visualized using a mercury lamp as an illumination source where an AFM cantilever is engaged to the tissue surface. The brighter regions (white arrows) are cell nucleus or light scatterings from the nuclei of the cells in layers underneath. The darker regions (black arrows), instead, are regions with perhaps less staining of the cell, tears in the tissue, or junctions of multiple cell peripheries.

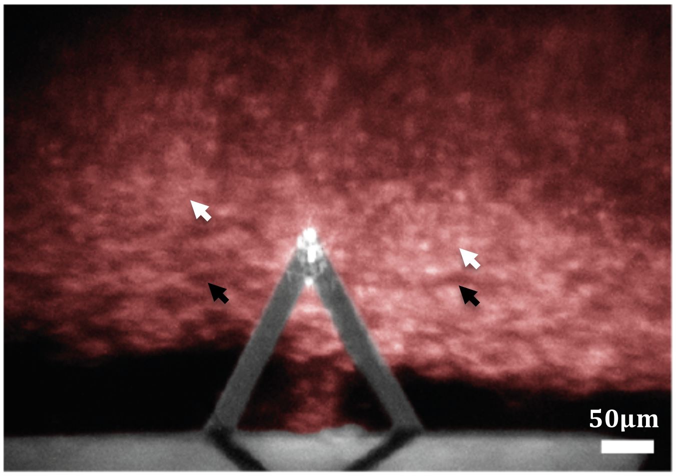

Figure 3.6: Visualization of SC cell nuclei in-situ using a mercury lamp and NucRed™ Live 647. White arrows point to brighter regions that represent cell nucleus or light scaterings from cells in layers underneath where as black arrows mark darker regions that are potentially cell periphries or tears in the tissue. The plane of focus is adjusted to the tissue surface and an AFM probe is in contact with the tissue.

3.3.3 Effect of staining on cell stiffness

To test whether labeling cells with NucRed™ Live 647 would affect their stiffness, Young's modulus of stained and unstained SC cells in culture was measured using 10µm rounded probes. Results in Figure 3.7 show that there is no significant difference (p=0.582) between the stiffness of control (unstained) (0.574±0.21 kPa, n=10) and stained groups (0.668±0.26 kPa, n=11) verifying the assumption that the stain does not change the stiffness of the cells.

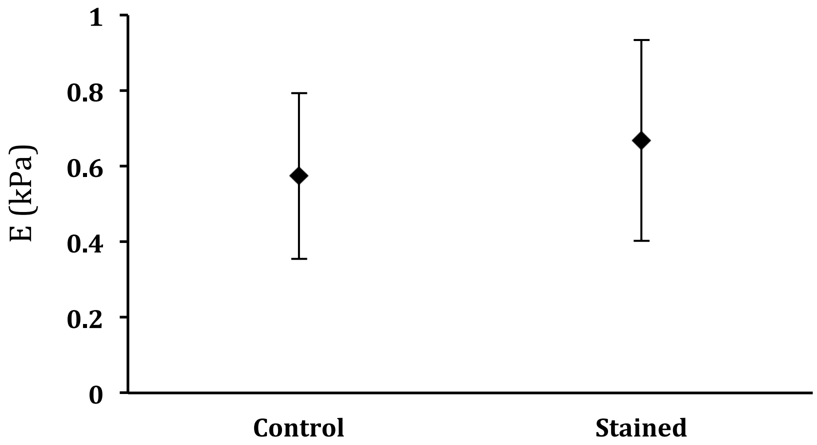

Figure 3.7: Effect of NucRed™ Live 647stain on the stiffness of SC cells. Comparison of the Young's modulus of control and cells labeled with NucRed™ Live 647 show that the stain doesn't change the stiffness of SC cells.

3.4 Experimental results

3.4.1 Young's modulus patterns and their frequency

AFM measurements were done on one glaucomatous (n=93) and 9 normal (n=280) samples. Single ramp cycles (as defined in 2.1.2) were performed in both dark and bright regions. The ramp size varied for the first five experiments on normal eyes (500nm, 1000nm, 2000nm) and was 2000nm for the rest of normal and glaucoma experiments (Table 3.2). We may note that (as described in 2.1) that the indentation is always smaller than ramp size and that a deeper ramp (2000 nm) already includes the information provided by shallower ones (500nm or 1000nm) and can provide additional information regarding the deeper regions inside the tissue. In tissue samples from normal eyes, there were 87 measurements at 500nm (n_{dark}=25, n_{bright}=62), 88 at 1000nm (n_{dark}=27, n_{bright}=61), and 105 at 2000nm (n_{dark}=43, n_{bright}=62) whereas all ramps for glaucomatous sample were 2000nm (n_{dark}=83,

n_{bright}=10) (see Table 3.2). Due to scarcity of the glaucoma globes, more measurements were done in the single glaucoma experiment to best use the only glaucoma tissue we had.

Table 3.2: The number of measurements for different ramp sizes

Tissue ID	500nm (n)	1000nm (n)	2000nm (n)	Normal/Glaucoma
G-M244638-OS	14	15	1	N
2411-15-01 (OS)	22	22	0	N
2411-15-01 (OD)	23	23	0	N
2633-15-01 (OS)	20	19	20	N
2633-15-01 (OD)	8	9	6	N
G-M247220-OS	0	0	26	N
W4035-V0183000	0	0	14	N
W4035-V0182000	0	0	21	N
W4035-V0180000	0	0	17	N
W4036-V0180000	0	0	93	G

We next determined the Young's modulus for each measurement as a function of indentation as described in 2.1.4. Five distinguishing patterns were seen as shown in Figure 3.8. In all patterns, the initial part (less than 50nm) is very noisy and usually shows high values. This has been attributed to uncertainties for contact point determination, and repulsive forces between the tip and the surface of the cell (Rico et al. 2005). In first pattern, P1, the values drop with increased indentation but rapidly plateau to a relatively constant value at a low value of modulus. This is similar to the pattern typically seen in in-vitro studies on endothelial cells when peripheral regions are avoided (see Figure 2 in (Vargas-Pinto et al. 2013)).

The next pattern, P2, includes a same initial plateau region that has an average value comparable to that of P1 but it is followed by a sharp rise in modulus with increasing indentation that reaches a second significantly higher asymptote. The third pattern, P3, also shares a similar initial plateau of comparable values with P1,but, unlike P1, the plateau is followed by a transition and unlike P2, it does not lead to a second plateau.

P4 is similar to P1, but he value of the plateau is much higher than that of P1, which distinguishes the two patterns from each other.

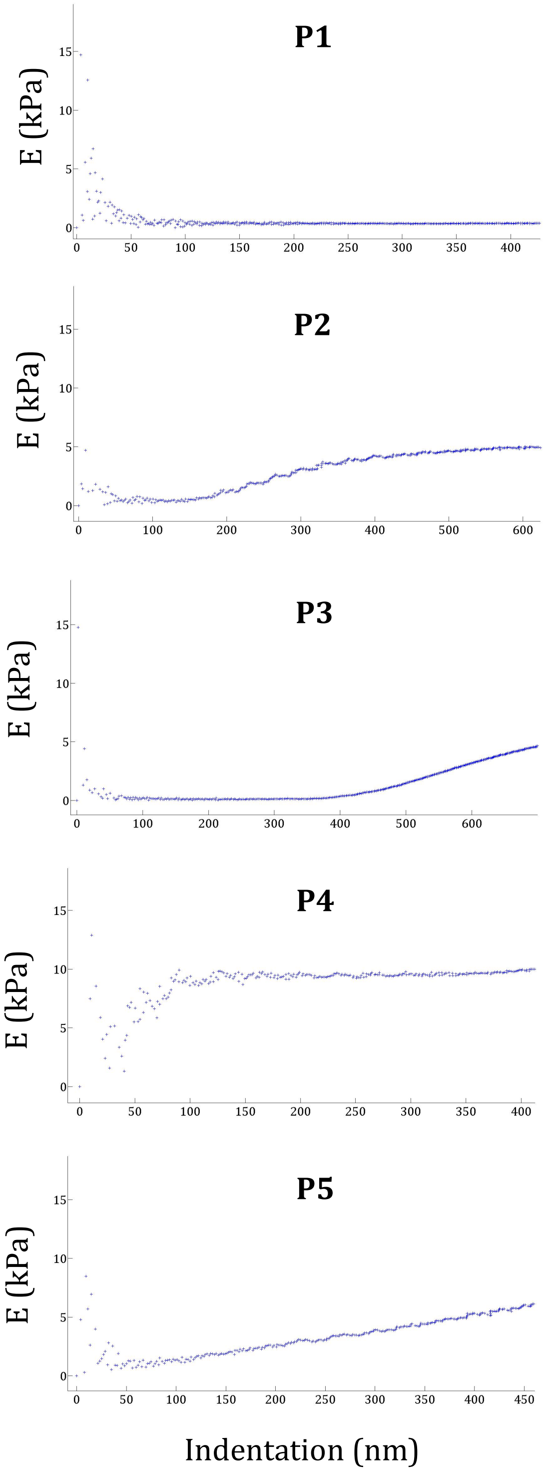

Figure 3.8: The patterns (P1-P5) of Young's modulus versus indentation. All patterns start with scattered data points. There is an initial plateau with lower modulus in P1-P3. P2 has a second plateau with higher modulus compared to the initial plateau in P1-P3. Same plateau occurs in P2. Finally, there is no plateau in P5.

In addition, the average value of the plateau in P4 is comparable to the second plateau in P2. Unlike first four patterns, the last pattern, P5, demonstrates a sharp transition that immediately occurs after initial noisy region. No asymptote is reached. However, the last value on the plot is comparable to last values in P2-P4. More examples of the pattern P1-P5 are shown in the Appendix.

To understand what might give rise to these different stiffness patterns, we first investigated the frequency of them in dark and bright regions. To do so, we analyzed the pattern frequency for ramp sizes up to 500nm, 1000nm, and 2000nm separately. As mentioned earlier, deeper ramps already include the information in shallower ones. Hence, to analyze the total 500nm ramp data for normal samples, the initial 500nm ramp data from 1000nm and 2000nm ramps were included in addition to data from 500nm ramps themselves. This same terminology was applied when analyzing other ramp sizes. Table 3.3 summarizes the frequency of each pattern in the dark and bright regions for all ramp sizes in normal and glaucoma samples. It is notable that while in the normal eyes, there were many more bright regions than dark, the opposite was true in the glaucomatous eye examined.

Table 3.3: Pattern frequency (n) in the dark and bright regions of normal and glaucoma samples. Data is presented based on the ramp sizes up to 500nm, 1000nm, and 2000nm.

		P1		**P2**		**P3**		**P4**		**P5**	
		Dark	**Bright**	**Dark**	**Bright**	**Dark**	**Bright**	**Dark**	**Bright**	**Dark**	**Bright**
500nm Ramp	**Normal**	14	62	1	3	33	68	11	18	36	34
	Glaucoma	13	0	1	0	18	7	24	0	27	3
1000nm Ramp	**Normal**	8	35	2	4	26	50	9	14	25	20
	Glaucoma	9	0	2	0	20	7	36	0	16	3
2000nm Ramp	**Normal**	5	19	1	2	16	22	6	8	15	11
	Glaucoma	9	0	4	0	18	7	39	0	13	3

To further characterize the pattern frequencies, for each ramp size, we calculated the percentage of pattern incidence for dark or bright categories separately as shown in Figure 3.9. Note that the percentage of bright region in each graph sum to 100% as do the dark regions; thus, the percentage of bright regions in each graph cannot be directly compared to the percentage of dark; only the relative patterns of P1-P5 can be compared.

Data for normal samples shows a similarity in pattern distribution between all ramp sizes where P1 is more prevalent in bright regions, P3 is almost equal between the bright and dark and P5 is more frequent in the darks. Compared to other patterns, P2 and P4 happen relatively less and are almost the same between dark and bright areas.

As mentioned earlier, P1 is similar to typical patterns seen when studying cells in-vitro. This is consistent with its higher incidence in bright regions that theoretically represent cellular regions.

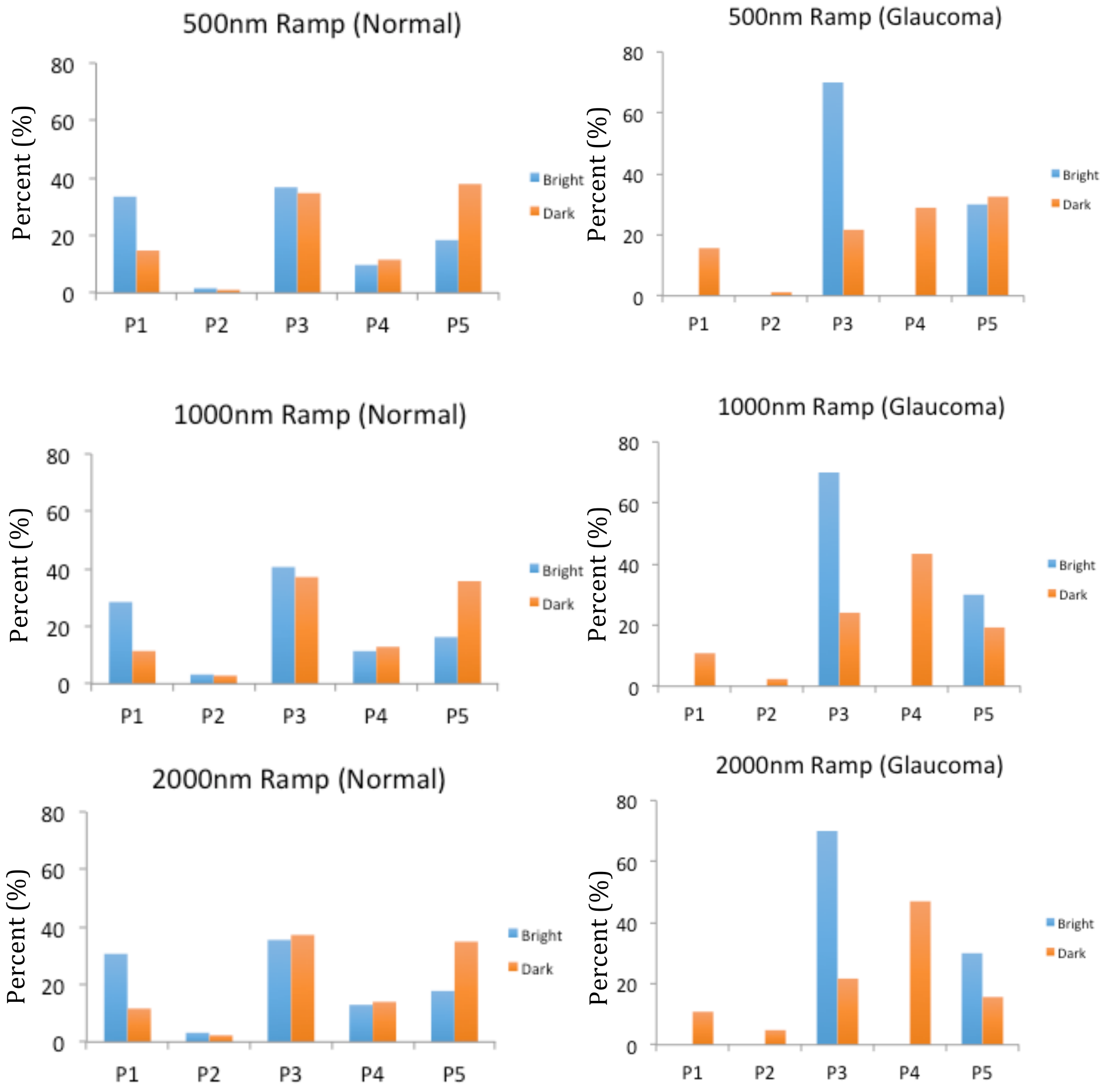

Figure 3.9: The categorized percentage (dark vs. bright) for the pattern incidence in nine normal and one glaucomatous sample. The percentage of pattern incidence in dark or bright regions is calculated separately.

We will show later in Chapter 4 that modeling results show patterns somewhat similar. Also we will show in 3.4.2 that the average Young's modulus in P1 is comparable to what has been previously reported for the stiffness of SC cells (Vargas-Pinto et al. 2013). Thus, we conclude that P1 is characterizing the mechanical behavior of SC cells.

Furthermore, we speculate that the initial plateau in P2 and P3 also correspond to cellular regions, as they are comparable to P1 in value. The modeling results in chapter 4 demonstrate that the transition in P2 and P3 to higher stiffness value with increased indentation is due to a stiffer substrate underneath soft cells. This also may explain the pattern seen in P5, but does not explain the absence of an initial plateau, which may be due the higher occurrence of P5 in dark regions that tentatively represent matrix regions where the cells were removed in tissue preparation, or measurement on the thin peripheral regions of the cells, which our studies in Chapter 4 suggest are dominated by cortex and matrix.. We will discuss in 3.4.2 that the average modulus for second plateau in P2 is comparable to previously reported values for the Young's modulus of TM (Last et al. 2011). This is also applicable to the plateau in P4, which may suggest that second plateau in P2 and the plateau in P4 are representative of the mechanical behavior of the trabecular meshwork, a conclusion we examine in more detail in chapter 4.

Data for the glaucoma sample shows that patterns P1, P2 and P4 only happen in dark regions, P3 and P5 happen in both dark and bright areas, and the frequency for each pattern is similar for different ramp sizes. As noted above, there were notably fewer bright regions in glaucomatous tissue as compared to a normal one. This is more evident from Table 3.3 where out of total 93 glaucomatous measurements only 10 were done on the bright regions, which was due to difficulties in finding those spots. This might be due to the glaucoma pathogenesis through which many of the outflow pathway cells may be dying or already dead and thus not stain at all. We may also note the caveat that all glaucoma measurements were done on only one globe as compared to normal measurements that were done on nine globes.

3.4.2 Young's modulus in the patterns

To quantitatively characterize the stiffness values measured as a function of indentation, we analyzed the modulus-indentation plots at three ramp levels of 500nm (n_{Normal}=280, $n_{Glaucoma}$=93), 1000nm (n_{Normal}=193, $n_{Glaucoma}$=93), and 2000nm (n_{Normal}=105, $n_{Glaucoma}$=93). To do so, we examined values corresponding to the average modulus of the initial plateau seen in P1-P3 (E_1: see [A] in Figure 3.10), the higher plateau seen in P2 and P4, (E_2: see [B] in Figure 3.10). We also calculated the value of the modulus on each plot at designated indentation depth of 200nm (n_{Normal}=259, $n_{Glaucoma}$=88), 500nm (n_{Normal}=113, $n_{Glaucoma}$=58), and 1000 nm (n_{Normal}=39, $n_{Glaucoma}$=33), which were called E_{final} and are marked as E_{200}, E_{500}, and E_{1000} respectively (recall that the ramp size is different than the indentation depth). E_{500} corresponds to the value of modulus at 500nm indentation (see arrow in Figure 3.10 [A]) (see Appendix for details).

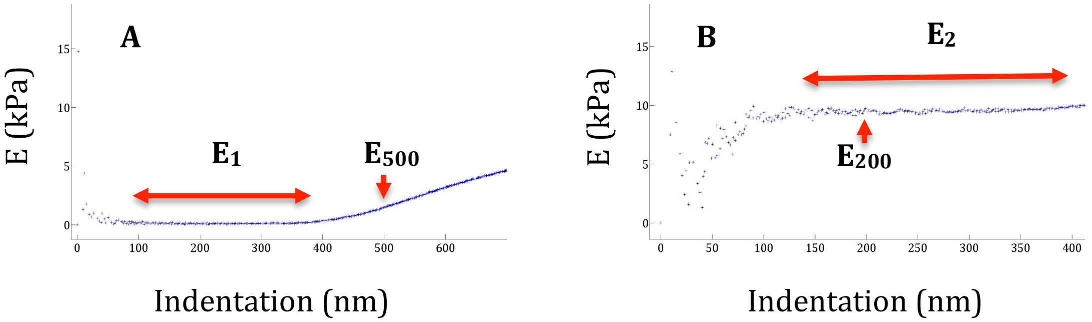

Figure 3.10: The average modulus for the initial plateau was named E1 [A], the after transition plateau in P2 and P4 with higher values named E_2 [B], and the modulus value at designated indentations of 200, 500, and 1000nm were named E_{200}, E_{500}, or E_{1000} (see the arrows in [A] and [B]).

We then calculated the overall averages for E_1, E_2, and E_{final} in dark and bright regions in normal (n=9) and glaucomatous (n=1) samples based on the criteria defined above and the results are shown in Figure 3.11.

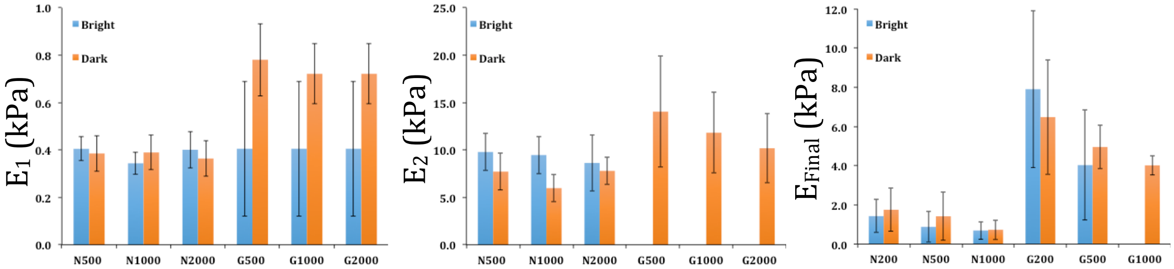

Figure 3.11: Average Young's modulus (mean±SE) for dark and bright regions in normal (n=9) and glaucoma (n=1) samples. From left to the right, the plots show the data for E_1 and E_2 for ramp sizes of 500nm-2000nm and E_{final} at indentation depths of 200,500, and 1000nm ("N" stands for normal and "G" stands for glaucoma). No significant difference was found between the dark and bright regions in neither normal eyes nor glaucoma sample at either indentation depth.

The average Young's modulus (mean±SE) of SC cells using rounded AFM probes (same probes as ours in this study and indentations less than 500nm) has been previously reported to be 1.24 ± 0.11 (kPa) for glaucomatous cells and 0.79 ± 0.10 (kPa) for normal ones in-vitro (Overby et al. 2014). Comparing the averages for E_1

(left plot) to in-vitro values, these values are lower than the in-vitro measured by Overby et al. The in-vitro measurements were done on SC cells cultured on plastic substrates that are much stiffer than the trabecular meshwork, which is the natural substrate for these cells. Cells in culture are expected to be stiffer when cultured on stiffer substrates (Discher et al. 2005b). As a result, we speculate that E_1 represents the in-situ stiffness of SC cells as measured by AFM.

The middle plot shows the results for E_2 where the average values are significantly higher compared to cellular stiffness range and similar to AFM value reported by Last et al. for trabecular meshwork. They reported an average modulus (mean±SD) of 4±2.2 (kPa) for normal TMs and 80.8±32.5 (kPa) for glaucomatous TMs. Comparison between the values of E_2 and the normal values reported by Last et al. suggests that E_2 may be reflective of the TM stiffness. However, we should note that our values of E_2 for the glaucomatous measurements, while relatively higher than measured in the normal samples, were much lower than that reported by Last et al (Last et al. 2011). Finally, the right plot includes the average value of the modulus at 200, 500, and 1000nm indentation. The data shows that the values for normal samples are notably lower as compared to their glaucomatous counterparts.

We used a t-test to compare the dark and bright values for the modulus within each group. The analysis showed that, at all indentation depths, there was no significant difference between the average modulus of dark and bright regions in either normal or glaucoma samples ($p>0.15$). As a result we merged the data for dark and bright regions to recalculate the averages for normal (n=9) and glaucoma (n=1) samples and used a Z-test to compare them as shown in Figure 3.12.

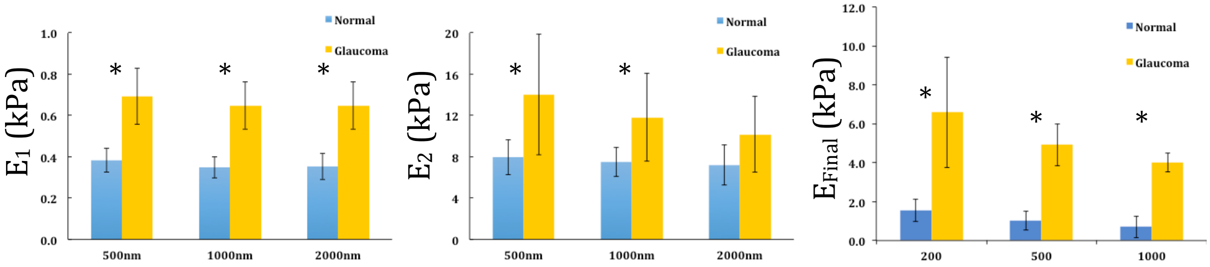

Figure 3.12: Average Young's modulus (mean±SE) for normal (n=9) and glaucoma (n=1) data sets. For all ramp sizes, the average modulus of E_1 and E_2 were significantly higher in glaucoma sample ($p<0.02$), except for E_2 at 2000nm ($p=0.12$). For all examined indentation depths, E_{final} was significantly higher ($p<0.0001$) for glaucomatous sample as compared to normal ones (Asterisks show statistically significant differences).

The comparison for E_1 showed that the average modulus for glaucoma sample was significantly higher than normal at all ramp sizes ($P<0.0001$), consistent with the finding of Overby et al. (2014).

The average values (mean±SE) for E_2 showed a similar behavior where the modulus was significantly higher in glaucoma sample at 500nm and 1000nm ramps ($p<0.003$), but there was no difference between normal and glaucoma averages at 2000nm ($p=0.12$).

We then examined to see how E_{200}, E_{500}, and E_{1000} would compare between normal and glaucomatous measurements. Here, the normal measurements led to surprisingly lower values even at indentation depths as high as 1000nm. This observation might imply that the immediate substrate of normal SC cells, its basement membrane, might be much softer than what we might have expected.

Comparing between glaucoma and normal samples, the plot clearly shows that regardless of the indentation depth, the overall average modulus (mean±SE) of glaucomatous sample was significantly higher than normal ($p<0.0001$).

Together, these observations suggest a stiffer TM in glaucoma sample as compared to normal, which is consistent with the data from Last et al. Nonetheless, our values for the glaucomatous TM are notably lower than what is reported by them. A stiffer TM in glaucomatous sample is also consistent with our observation for stiffer SC cells in-situ as its well known that cells tend to become stiffer when cultured on stiffer substrates (Discher et al. 2005a)(Solon et al. 2007). However, our data set for the glaucoma measurements is limited to only one sample and thus our conclusions are largely speculative.

3.5 Discussion

3.5.1 Rationale for developing our method

Last et al. (2011) presented important evidence that the trabecular meshwork of glaucomatous eyes is dramatically stiffer than that found in normal eyes. Our studies generally support this conclusion, although our preliminary evidence is based on a single glaucomatous globe whose TM stiffness was not as high as that measured in Last et al. Several caveats can be raised regarding the Last et al. study. First, they used cyanoacrylate glue to immobilize the tissue. Their group later showed that use of such adhesives can significantly change the mechanical properties of the probed sample and introduce artifacts (Morgan et al. 2014). A second caveat is that the average time from eye donation to AFM measurement was 17.5 days for normal eyes and 7.4 days for glaucomatous samples although the tissue sample were stored in corneal storage medium at 4°C during this time. While the medium could have kept the tissue viable, the long storage time before AFM experiment could have introduced significant changes to the structure and mechanics of tested tissues.

A final caveat is that the inner wall tissue is a highly heterogeneous structure that includes cellular (inner wall endothelium of SC) and connective tissue (TM) regions. This was our logic to analyze the data based on designated ramp sizes and indentations to make our measurements relatively comparable to each other.

These limitations were our incentives to develop a method that minimized artifacts but still allowed for simultaneous characterization of relatively fresh specimens of the inner wall endothelium of SC and the TM.

Our experimental results confirmed the presence of cellular and TM regions with distinct mechanics and proved that the suggested method is able to effectively distinguish between them. Through this technique, we could simultaneously estimate the stiffness of SC cells and TM in-situ. However, as we will discuss in chapter 4, all of our AFM measurements are influenced by both cell cortex and TM stiffness to some extent, which means that our extracted values for Young's modulus of SC cells and TM are estimations, but not absolute. We will further examine the effect of cortex and TM stiffness on AFM measurements in chapter 4.

3.5.2 Interpretation of Young' modulus

We examined the difference between dark and bright regions both in terms of frequency of P1-P5 patterns and values of elastic modulus. While we found that P1 patterns were more likely to be associated with bright regions and P5 more likely dark regions, this was not a strong association and was only seen in the normal globe, not the single glaucomatous globe. No statistical difference was seen in the elastic moduli between the dark and light regions. This is likely due to there being several causes for dark regions including areas of damage to the inner wall due to dissection, differential staining and possible cell death, especially in the glaucomatous globe.

For all ramp sizes, the values of E_1 were within the cellular stiffness range whereas the values for E_2 corresponded to TM stiffness. This observation implied that the initial plateau in P1-P3 is indeed likely to represent SC cell stiffness as compared to the plateau in P2 and P4 that is more likely to characterize TM stiffness. Using our method, we were able to measure the stiffness of these cells in-situ where the average modulus was 0.69 ± 0.14 and 0.38 ± 0.06 (kPa) for glaucomatous and normal SC cells respectively (500nm ramps) and the difference between the two was again significant ($p<0.0001$). The higher modulus in in-vitro measurements (Overby et al, 2014) was consistent with their higher substrate stiffness (plastic petri-dish) as compared to in-situ measurements where cells had a significantly softer substrate (TM).

The values for TM stiffness (from E_2) suggested that the TM from the glaucomatous globe was significantly stiffer than normal ones in 500nm and 1000nm ramps ($p<0.003$). While the difference for 2000nm ramps was not statistically significant ($p=0.12$), the glaucomatous TM modulus (10.18±3.66 kPa) was still notably higher than the total average modulus for normal TMs (7.2±1.95 kPa). While this finding is consistent with the conclusion from Last et al., their reported values for the glaucomatous TMs (80.8±32.5 kPa) are much higher than ours at any ramp size (the highest in ours is 14.04±5.84 (kPa) for 500nm ramps).

Comparing the last values of the modulus at different indentations (E_{200}, E_{500}, E_{1000}), we found the overall stiffness of the glaucomatous tissue to be much higher ($p<<0.0001$) than that of normal globes. While this finding is consistent with the conclusion from Last et al., their reported values are much higher than ours at any indentation size. We believe there are some factors that might be the reason for the discrepancy between our values and data from Last et al. First, using the cyanoacrylate glue to immobilize samples might have affected some of their measurements. However, the good agreement between our results for normal samples and results from Last et al. would seem to suggest otherwise. A second potential reason is the long death to experiment interval (average of 17.5 days for normal and 7.4 days for glaucomatous samples) in their studies. Here the speculation is that the long storage interval could have introduced significant changes to the structure and mechanics of the IW in glaucomatous globes whereas the healthy tissue might not been affected as much; in particular, they could have had significant cell death that might have been pronounced in the glaucomatous eyes. We should also note that the measurements from Last et al. were performed using rounded tips with 2μm radius where ours were done using larger probes (D=10μm). We will show in chapter 5 that the AFM tip size has a significant effect on the measurements where smaller tips tend to give higher modulus values. However, Last et al. used same tip size when making measurements on normal and glaucomatous TMs, and thus this cannot explain the discrepancy.

As mentioned earlier in the chapter, the outflow facilities for the last two normal eye globes and the glaucoma globe were measured in perfusion studies. The outflow facility for N8 and N9 were 0.21 and 0.25 (μl/mmHg*min) respectively where as it was significantly lower, 0.09 (μl/mmHg*min), for the glaucoma globe. Comparing SC cell stiffness values for these globes (see Appendix), it turns out that cells in N8 and N9 are significantly softer compared to the glaucoma sample. This observation suggests a tentative relation between in-situ stiffness of SC cells and the outflow facility yet, needs to be examined in much more detail.

3.5.3 Limitations and future directions

The first limitation for our experiment was the non-specificity of the stain that was used to mark the cell nucleus. While in most, but not all samples the stain was efficacious enough to stain the nucleus within a short period of time, it did not only stain the SC cells, but the entire cell population inside the tissue. As a result, the fluorescent light from the stained cells inside TM caused light scattering effects at the plane of focus, which made it difficult to distinguish between the dark and bright regions. This means that we cannot be sure that all the measurements on the bright regions are on SC cells. Similar limitation exists for dark regions that could be cells that did not stain, tears in the tissue, or junctions for multiple cell peripheries. Results from AFM measurements somehow confirm this uncertainty, as there was no statistically difference between the dark and bright measurements in almost all measurements. The ideal solution to resolve this issue would be to find a stain that is specific to live SC cells and can work in the time scales available to us for these experiments, or to use of a confocal microscope that allows exclusion of scattered light from out of focus planes.

The second caveat in our studies was lack of enough glaucoma samples. While we were able to include 9 normal globes in our study, we only had one glaucomatous globe due to scarcity of these globes and their very high research demands. This limitation restricts our comparison of normal and glaucomatous measurements to only one observation and doesn't allow for evaluation of variability in mechanics of glaucomatous tissues.

3.6 Conclusions

A novel method was developed to simultaneously characterize the mechanics of SC cells and TM in-situ. Data from our method verified the presence of cellular and tissue regions in the inner wall tissue and were capable to distinguish between their mechanical properties.

Using this technique, we could measure the stiffness of SC cells and TM in normal (n=9) and glaucomatous (n=1) eyes. We have previously shown that glaucomatous SC cells have higher stiffness compared to their normal counterparts in-vitro (Overby et al. 2014). Here, we used our new method and extended the previous conclusion to in-situ, where we found glaucomatous SC cells are still significantly stiffer than normal SC cells when residing on their original substrate (TM).

We also measured an average modulus for the TM in normal (n=9) and glaucomatous (n=1) samples and found a higher stiffness for glaucomatous tissue. This is consistent with previously reported data for the mechanics of TM in normal and glaucomatous eyes (Last et al. 2011).

We have before shown that the increased stiffness in cultured glaucomatous SC cells could impede pore formation in these cells in-vitro (Overby et al. 2014). Also, it has been shown that pore density is significantly reduced in glaucomatous eyes (Johnson et al. 2002), a phenomenon that would be expected to lead to increased outflow resistance (Overby et al. 2009). Thus, our studies are consistent with a hypothesis that the elevated flow resistance characteristic of glaucoma results from increased SC cell stiffness.

Chapter 4: Finite Element Analysis of AFM indentations on inner wall tissue

4.1 Overview

In chapter 3, we described methods and results for AFM measurements for stiffness characterization of the inner wall tissue. There were five distinct patterns for the Young's modulus when stiffness was plotted as a function of indentation (see Figure 3.8). In four patterns (P1-P4), we detected plateaus with either lower values in the cellular stiffness range or higher values that could represent tissue stiffness. Also, there was no plateau in one pattern (P5).

In this chapter, we describe a finite element model that simulates indenting the inner wall using a rounded AFM probe (D=10μm). The inner wall is modeled as a single SC cell lying on a trabecular meshwork (TM) of varying elastic modulus. The SC cell is modeled as a homogeneous soft cytoplasm with a cortex of variable modulus on top and bottom surface. We will then use this model to interpret our experimental measurements.

4.2 Methods

4.2.1 Model

We modeled AFM indentations on nuclear (thick) and peripheral (thin) regions of the cell, since we anticipated that we might see very different behaviors in these two cellular regions. Thus, two separate geometries were created, in each case, with an AFM indentation of a cell lying on an elastic TM. For each geometry, the cell (cortex and cytoplasm) and the TM were modeled as discs with 50μm radius. The radius is not physically reasonable (SC cells are typically 5-15 μm wide and 40-100 μm long, Johnson, 2006), but serves to keep this as a 2D problem. The radius of the discs was chosen such that the strain at the edge of the domain was less than 0.1% of the maximum strain near the tip. Figure 4.1 shows the schematic for indentations on nuclear [A] and periphery [B] region. The uppermost layer of the model is cell cortex. The thickness of the cortex in SC cells hasn't been characterized in-situ, but we have previously shown that cultured SC cells have an average cortex thickness of 400 nm (Vargas-Pinto et al. 2013). Next is the cytoplasm of the cell with a thickness of 4.5μm (Vargas-Pinto et al. 2014) for nuclear region [A] and 1μm (Johnson 2006) at cell periphery [B] and underneath that is another cortical layer, with the same properties as the cortex on top surface. The substrate underlying the cell, representing the basement membrane, JCT region and the rest of the trabecular meshwork, has a thickness of 100μm (Johnson 2006).

The indentation depth was set to 2μm to match the experimental conditions. However, for some cases with high cortex and TM modulus, and especially in peripheral region, the indentation had to be limited to a lower depth to avoid excessive element distortion that prevented convergence of numerical solution in ABAQUS. The Young's Modulus of the cytoplasm was assumed to be 1 kPa (Zeng et al. 2010) and the modulus of the cortex and TM each varied between 1 to 50 times the modulus of the cytoplasm.

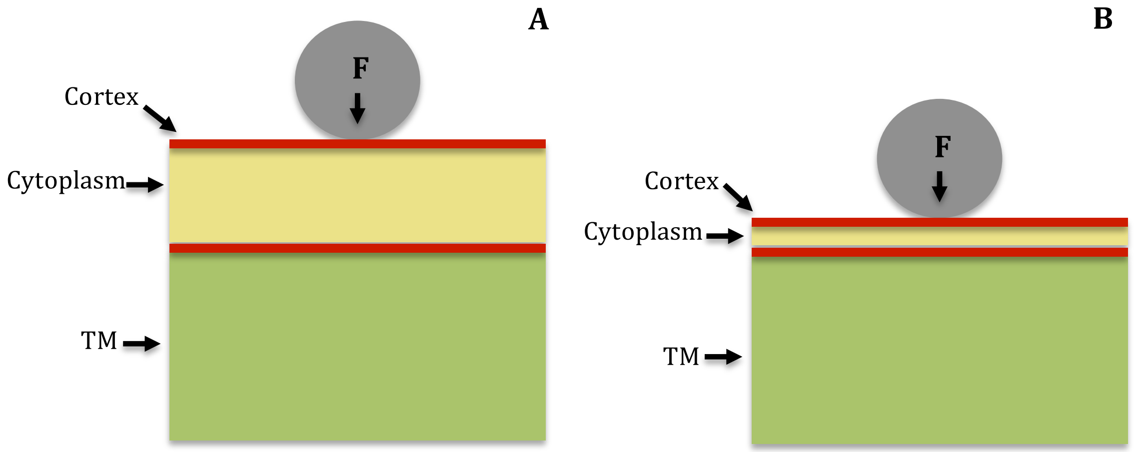

Figure 4.1: Schematic of the geometries used for AFM indentation on nuclear [A] and peripheral [B] regions of the cell. (drawings are not to scale)

4.2.2 Boundary conditions

The bottom surface of the TM was pinned for zero displacement. Top and bottom cortices were tied to the cytoplasm to create a no-slip boundary condition between the cortex and cytoplasm. The same condition was applied to the bottom cortex and the TM.

4.2.3 Mesh and element selection

The smallest and largest element lengths were 10nm and 500nm respectively. The element width (height direction) was kept constant in cortex and cytoplasm and a bias factor was introduced to the TM where the smallest and largest elements were 10nm and 200nm respectively. The initial guess for element size was from previous modeling (Vargas-Pinto et al. 2013). Table 4.1 shows the three examined cases to find the optimal element size for simulations.

Table 4.1: The examined cases for finding the optimal mesh size.

	Cortex and Cytoplasm		TM	
Case	Element Length (nm)	Element Width (nm)	Element Length (nm)	Element Width (nm)
1	10-500	10	10-500	10-200
2	20-500	20	20-500	20-200
3	40-500	40	40-500	40-200

The force vs. indentation curves for the three cases in table 4.1 are shown in figure 4.2 where cortex, cytoplasm, and TM have equal stiffness. The error between the case with smallest (case 1) and largest (case 3) elements was 0.017%. However, increasing the smallest element size from 40nm to 100nm led to errors higher than 0.5%. As a result, case 3 was chosen for the analysis.

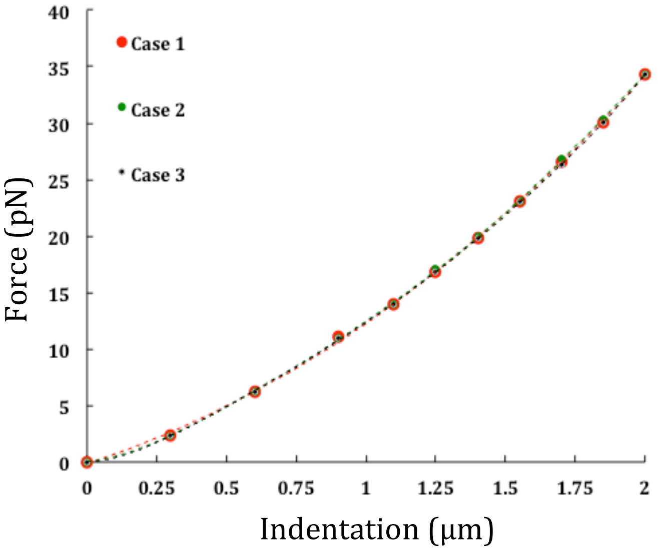

Figure 4.2: Mesh validation for AFM simulations. Results are shown for 3 different mesh sizes for the AFM probe (R=5μm) at $E_{cortex} = E_{cytoplasm} = E_{TM}$.

4.3 Results

Results for indentations on nuclear region are shown as $E_{apparent}/E_{cytoplasm}$ vs. indentation in Figure 4.3. The cortex modulus is constant for each graph whereas the TM stiffness varies between one to fifty times (1x-50x) the stiffness of the cytoplasm.

Starting from the plot for $E_{cortex} = E_{cytoplasm}$ (first plot from the top), it appears that when $E_{TM} = E_{cytoplasm}$ (lowest curve) the curve for $E_{apparent}$ slightly drops by increase in indentation depth and finally asymptotes to $E_{apparent}/E_{cytoplasm} = 1$ at indentations higher than 1.5µm. On the same plot, results for $E_{TM} = 2^* E_{cytoplasm}$ show a notable change for $E_{apparent}$ upon a relatively slight increase in TM stiffness where the apparent modulus at 2µm indentation is about 40% higher as compared to $E_{TM} = E_{cytoplasm}$. Further analysis of the

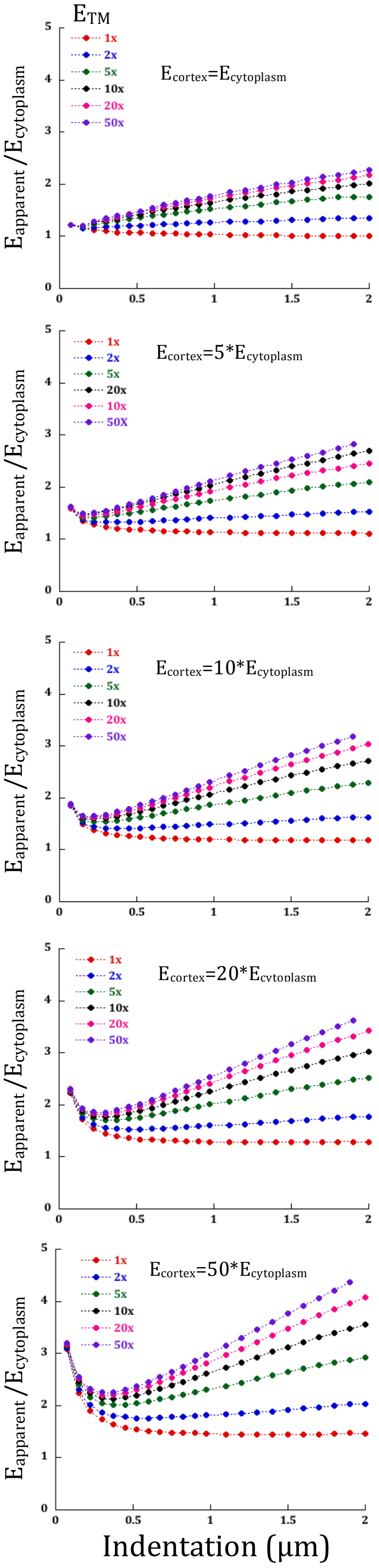

Figure 4.3: Calculated apparent modulus for indentations on the nuclear region for different cortex and TM stiffness. The cortex stiffness is 1-50 times the stiffness of the cytoplasm and the TM stiffness changes from 1-50 (marked as 1x-50x) times the stiffness of the cytoplasm.

$E_{cortex} = E_{cytoplasm}$ plot at higher values of $E_{TM} / E_{cytoplasm}$ (5x-50x) reveals a set of curves where each curve has a minimum. The minimum occurs at indentations of roughly 100nm-400nm and the extent of the rise for further indentations depends on TM stiffness where stiffer TMs cause a steeper increases. The observations for $E_{cortex} = E_{cytoplasm}$ are expandable to plots for other ratios of $E_{cortex}/E_{cytoplasm}$. For instance, at $E_{cortex} = 20*E_{cytoplasm}$, analysis for higher values of $E_{TM} / E_{cytoplasm}$ (5x-50x) shows that, again, there is a set of curves with more pronounced minimums around 100-400nm. An important point to notice is that in all plots, the curves start from a single point that is independent of TM stiffness. This suggests that the initial indentations are affected by the cortex stiffness to a high extent and are almost independent of TM mechanics; the curves diverge upon increase in indentation indicating that, as expected, TM stiffness becomes more important when indentation depth increases.

Results for indentation on the peripheral region of a cell are presented in Figure 4.4. As mentioned in 4.2.1, the indentation was limited in some cases to avoid excessive element distortion and non-convergence of the numerical solution in ABAQUS. Similar to the simulations of nuclear indentations, when $E_{cortex}=E_{cytoplasm}$, the curve for $E_{TM} = E_{cytoplasm}$ tends to slightly drop by increase in indentation depth where it asymptotes to $E_{apparent}/ E_{cytoplasm} = 1$ at indentations higher than 1.3µm. This behavior is common among all periphery plots where they tend to asymptote to E_{TM} after a progressively deep indentation. The pattern for $E_{TM} = 2* E_{cytoplasm}$ is also similar to nuclear indentations where a relatively small increase in TM stiffness could yield around 80% increase in apparent modulus (at 2μm indentation) as compared to E_{TM} = $E_{cytoplasm}$. Considering plots with stiffer cortex, for instance E_{cortex}=50*$E_{cytoplasm}$, we found a new pattern at E_{TM} =5*$E_{cytoplasm}$ where at relatively deep indentation, the curve tends to asymptote to the average value of $E_{apparent}$/$E_{cytoplasm}$=5.1, which is comparable to TM stiffness. An interesting point about all peripheral plots is that unlike nuclear indentations, their curves for higher ratios of E_{TM}/$E_{cytoplasm}$ (10x-50x) don't show minimums for small indentations except at E_{cortex}=50*$E_{cytoplasm}$; Instead, the modulus in majority of the curves rapidly increases after the indentation begins. This suggests that for peripheral aspect of the cell, TM stiffness has more effect on low indentation values of $E_{apparent}$ as compared to nuclear aspects.

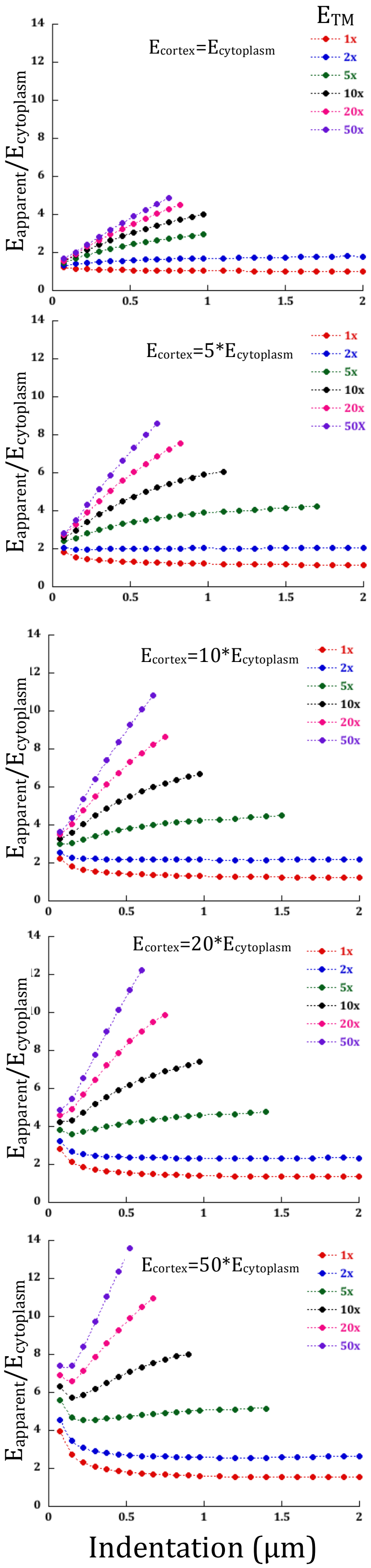

Figure 4.4: Calculated apparent modulus for indentations on the peripheral region for different cortex and TM stiffness. The cortex stiffness is 1-50 times the stiffness of the cytoplasm and the TM stiffness changes from 1-50 (marked as 1x-50x) times the stiffness of the cytoplasm.

Figure 4.5 shows the values of $E_{apparent}/E_{cytoplasm}$ for different values of cortex stiffness at a constant TM modulus ($E_{TM}=5*E_{cytoplasm}$) for both nuclear and peripheral regions. In both regions, the simulations show that increases in cortex stiffness leads to a systematic and significant increase in $E_{apparent}$, especially for shallow indentations. For instance, comparing the curves for $E_{cortex}=50*E_{cytoplasm}$ (50x) to $E_{cortex}=E_{cytoplasm}$ (1x), apparent modulus increases up to 156% (first data point on the curve) in the nuclear region [A]. The effect is more dramatic in the peripheral region where same comparison leads to up to 280% increase (first data point on the curve) [B]. These observations thus imply that cortex has a significant effect on both nuclear and peripheral measurements.

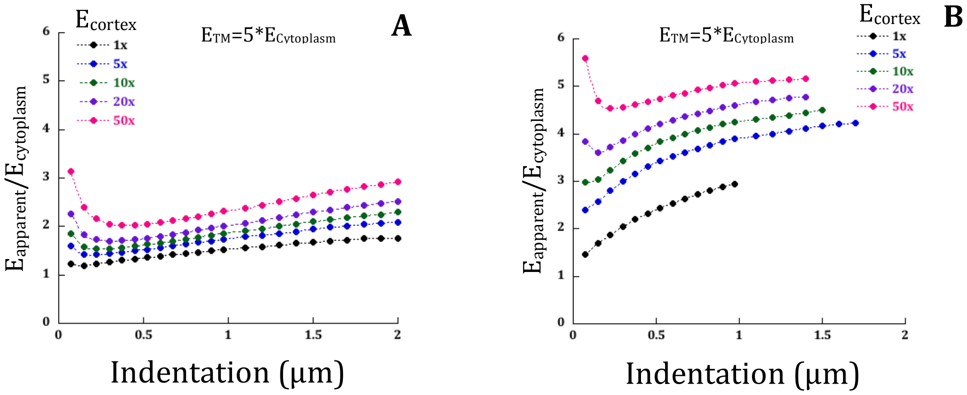

Figure 4.5: Calculated apparent modulus for indentations on nuclear (A) and periphery (B) regions with the same TM modulus but different cortex stiffness. The stiffness of the cortex is 1-50 times the stiffness of the cytoplasm and E_{TM}= $5*E_{cytoplasm}$. In some cases, indentations are limited to avoid excessive element distortion.

We finally examined for the effect of cytoplasm on measurements in nuclear and peripheral regions, where we selectively plotted $E_{apparent}/E_{cytoplasm}$ at

E_{cortex}=50*$E_{cytoplasm}$ for nuclear and peripheral regions (Figure 4.6). Results are presented for three different cases where E_{TM} is 1x, 5x, 50x $E_{cytoplasm}$.

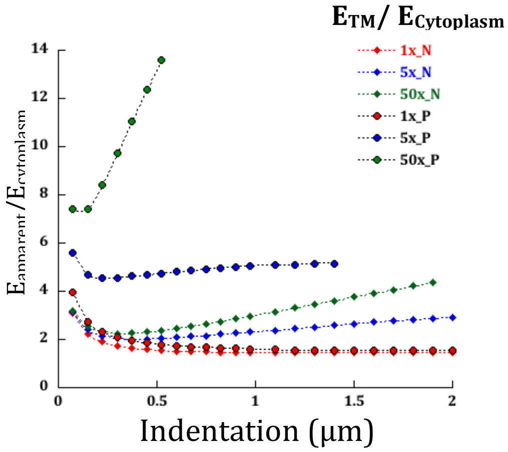

Figure 4.6: Effect of cytoplasm on measurements. Data for $E_{apparent}$ in nuclear (rhombus) and peripheral (circle) regions are plotted for cases where E_{cortex}=50*$E_{cytoplasm}$ and the relative stiffness of $E_{TM}/E_{cytoplasm}$ changes between 1-50. "N" is nuclear and "P" is periphery.

As seen from the plot, there is a minor difference between the nuclear and peripheral indentations for E_{TM}=$E_{cytoplasm}$. However, when E_{TM}=5*$E_{cytoplasm}$ and E_{TM}=50*$E_{cytoplasm}$, peripheral indentation gave very different results than did nuclear indentation. For E_{TM}=5*$E_{cytoplasm}$, the value of $E_{apparent}/E_{cytoplasm}$ at periphery region is very comparable to TM modulus after about 500nm indentation where as it is much lower for the nuclear regions even at higher indentation depths (see blue curves). This demonstrates how reduction in cytoplasm thickness in peripheral regions influences AFM measurements and causes more effect from TM stiffness on $E_{apparent}$. It also implies that the effect from cytoplasmic stiffness mainly influences the initial regions of indentation whereas deeper indentations are mostly dominated by TM mechanics. These same observations apply to E_{TM}=50*$E_{cytoplasm}$ in which values for

$E_{apparent}$ are notably higher for peripheral measurements and the increase in modulus values is faster due to reduced cytoplasm thickness.

4.4 Discussion

4.4.1 Effect of TM and cortex stiffness on AFM measurements

The computational simulations showed a significant effect of TM and cortex stiffness on AFM measurements in both nuclear and peripheral regions. As expected, Figures 4.3 through 4.5 show that for both nuclear and peripheral measurements, there is a positive correlation between the TM or cortex stiffness and $E_{apparent}$ where stiffer TMs or cortices lead to higher values of $E_{apparent}$ at all indentation depths.

The plots also suggest that all curves will asymptote to E_{TM} for a deep enough indentation. Figures 4.3 and 4.4 also show that at higher values of E_{TM}, curves are generated with a minimum, a behavior we have seen in some experimental measurements [see sample plots for P5 in Appendix]. The extent of the rise in the curve after the minimum point depends on TM stiffness and is higher at deeper indentations; this implies that the values at deeper indentations are mainly dominated by TM mechanics. Figure 4.5 shows that cortex stiffness influences measurements at all indentation levels. However, the initial values of $E_{apparent}$ are influenced the most. Thus, cortex stiffness is more influential for shallow indentations as opposed to TM stiffness that is more dominant for deeper indentations.

Figure 4.4 showed that indentations in peripheral region for E_{TM}=$E_{cytoplasm}$ behave similar to those of E_{TM}=$E_{cytoplasm}$ for indentations in the nuclear region. However, unlike the behavior in the nuclear region, for higher values of E_{TM}, most simulations of the indentations of the periphery of a cell did not exhibit a minimum in the curves. Instead, the curve had a rise immediately after the indentation began. In general, comparing similar cases between nuclear and peripheral indentations (Figure 4.6), it is evident that the latter are much more influenced by TM stiffness as compared to the former.

Also notable is the behavior for small indentations where $E_{apparent}$ is nearly independent of E_{TM} and only a function for E_{cortex}. This is particular true for the nuclear regions of a cell (Figure 4.3) but also largely true for the peripheral region (Figure 4.4). Overall, both indentations in both the nuclear and peripheral regions show that the values of $E_{apparent}$ are dominated by the stiffness of the cortex and cytoplasm for shallow indentations (less than perhaps 500nm) whereas for increase indentation depth the stiffness of the trabecular meshwork begins to strongly affect the results.

4.4.2 Comparison of the numerical results to experimental data

Data from AFM experiments results in five major patterns for the Young's modulus as described in 3.4.1. In this chapter, we aimed to reproduce these patterns using numerical simulations and examined the comparability between the simulation and experimental patterns. Here, our approach was to choose a proper value for $E_{cytoplasm}$

in numerical simulations to generate an $E_{apparent}$ with comparable values to modulus from the experimental results.

Simulation results in Figures 4.3 and 4.4 include patterns that are similar to the experimental pattern P1. To quantitatively match the simulation and experimental data for P1, we choose a value of 0.2kPa for $E_{cytoplasm}$ when E_{cortex}=10kPa and E_{TM}=0.2 kPa. We then extracted the curve for $E_{apparent}$ in both nuclear and periphery regions and plotted those curves versus an actual P1 graph from our experimental data as shown in Figure 4.7 [A].

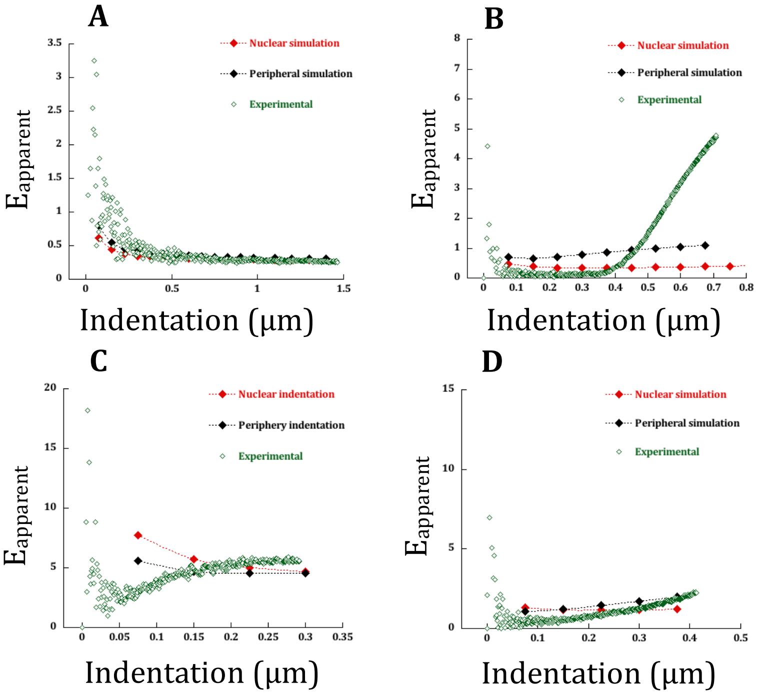

Figure 4.7: Comparison of the experimental data to computational simulations. The computational data patterns did not match the experimental data for P2 (not shown), P3 [B] and P4 [C]. However, for P1 [A] and P5 [D??], there were curves in nuclear and peripheral regions that reasonably matched the experimental data.

The plot shows a significant similarity between the numerical and experimental results at indentations deeper than 250nm. For indentations less than 250nm, the experimental results show higher values for the modulus. While these higher values could be due to higher cortex stiffness in experimental conditions, they can also be due to experimental noise, uncertainties in the contact point determination, and repulsive forces between the tip and the surface of the cell (Rico et al. 2005). Our conclusion from these observations is that P1 represents a cell with a stiffer cortex that is sitting on a TM with equal stiffness to cell cytoplasm. However, this condition is not very likely to occur in actual biological tissues.

We next moved to examine pattern P2. As explained in 3.4.1, P2 demonstrates a notable plateau at the first few hundreds of nanometers of the indentation that is followed by a transition and a second plateau. Results in Figures 4.3 and 4.4 show that none of the generated curves in our numerical simulations offered such pattern and thus, the model cannot explain this behavior.

Like P2, pattern P3 also starts with an initial asymptote that is followed by a significant rise. Data from the numerical simulation, especially in the nuclear region, show some level of similarity to P3. Nonetheless, none of these curves have a prominent asymptote as the ones in an experimental P3 curve. We hence plotted $E_{apparent}$ for nuclear region at $E_{coytoplasm}$=0.15kPa, E_{cortex}=7.5 kPa and E_{TM}=7.5 kPa and for periphery region at $E_{coytoplasm}$=0.1 kPa E_{cortex}=5 kPa and E_{TM}=2 kPa as shown in Figure 4.7 [B]. The plot shows that data from the nuclear simulation can only capture the initial plateau and fails to mimic the rise. For periphery, the initial plateau is much shorter as it is in the experimental data and the extent of the rise is much less compared to actual results. Thus, like P2, the model didn't give patterns analogous to P3.

For simulations in the nuclear region, we were unable to find parameters that gave curves similar to those seen with pattern P4. For peripheral curves though, we may note that the $E_{TM}=5*E_{cytoplasm}$ curves in periphery indentation (Figure 4.4) showed some similarity to P4. However, a closer examination of these curves show that they all tend to start to plateau at indentations equal or deeper than 1μm whereas in the experiments measurements that showed a pattern of P4 (see Figure 3.8 and plots in Appendix), the plateau begins after the first 200nm indentation, significantly different from the simulation results. To illustrate these differences, we plotted $E_{apparent}$ of the nuclear region at $E_{coytoplasm}$=2.5kPa, E_{cortex}=125kPa and E_{TM}=5 kPa and for periphery region at $E_{coytoplasm}$=1kPa E_{cortex}=50kPa and E_{TM}=5 kPa as shown in Figure 4.7 [C]. The results confirm that the model is not able to qualitatively match P4 and moreover, the required values for $E_{coytoplasm}$ to quantitatively match the experimental results are not with the experimental range for $E_{coytoplasm.}$ This latter fact suggests that P4 is a measurement on cell matrix rather than cell itself.

We finally compared data from simulations and the experiment for P5 as shown in Figure 4.7 [D]. Here, we chose $E_{cytoplasm\ =}$ 0.7kPa, E_{cortex}=7 $kPa_{,}$ and E_{TM}=35 kPa in indentations in the nuclear region and $E_{cytoplasm\ =}$ 0.22kPa, E_{cortex}=4.4 $kPa_{,}$ and E_{TM}=11 kPa for peripheral regions and compared the corresponding $E_{apparent}$ to a P5 graph from the experiments. Overall, the plot shows that the model was able to reproduce the pattern P5 to some extent, and especially for peripheral indentations deeper than 100nm. Here, we conclude that the pattern P5 may represent a cell with stiffer cortex sitting on a TM that is significantly stiffer than cell cytoplasm.

4.5 Limitations and future directions

In our modeling studies we assumed that the cortex of an SC cells has a uniform thickness of 400nm, which is based on previous in-vitro thickness measurements (Vargas-Pinto et al. 2013). However, cell cortex is a dynamic structure that regulates its mechanics and structure based on the cell microenvironment (Eghiaian et al. 2015). As a result, thickness estimations from in-vitro studies may not necessarily apply to in-situ situations where the cell microenvironment is significantly different. Further studies are required to test for the effect of cortex thickness on our results.

Another limitation in our modeling studies is the assumption of a homogeneous substrate underlying the SC cells that is certainly not the case. The immediate substrate of SC cells is their basement membrane, which is known to be discontinuous (Johnson & Tamm 2010) and have a thickness of perhaps less than a micron. Below this is the JCT which 10 μm thick (Johnson & Tamm 2010), and the corneoscleral and uveoscleral meshworks underlying the JCT; the total thickness of the regions is 100μm (Johnson & Tamm 2010). These regions have significant structural differences that potentially confer distinct mechanics to them. Yet, the mechanics of these distinct regions has not been examined. Future work should focus on studying the effect of this variation through a revised numerical model.

Finally, in this study we modeled the components as homogeneous isotropic elastic materials for sake of simplicity. Nonetheless, it has been shown that biological material such as cells and tissues, which go under large deformations, behave like hyperelastic materials (Yamada et al. 2010) and thus, elastic models may not accurately predict their behavior. As a result, future studies should focus on modeling the components as hyperelastic models such Neo-Hookean (Vargas-Pinto et al. 2014).

4.6 Conclusions

In this chapter, we sought to use FEM to better understand the data from AFM experiments. We modeled the inner wall tissue samples that we extracted and test as a layer of elastic cells with the included a cortex surrounding the cell, sitting on an elastic homogeneous TM. The simulation was done for nuclear and peripheral regions of SC cells and the apparent modulus was calculated for all studied cases.

Overall, results showed that in both nuclear and peripheral regions, the values of apparent modulus for shallow indentations are primarily influenced by cortex and cytoplasmic stiffness whereas deeper indentations are dominated by TM stiffness. The effect of TM is more dominant in measurements of the periphery of cells and the values of effective modulus are notably higher as compared to measurements in the nuclear region.

Results from simulations succeeded in matching the experimental data for P1 and P5 in both nuclear and periphery regions (see Figure 3.9). Our conclusion based on the modeling results is that the asymptote in P1 corresponds to cell stiffness and represents a cell with a stiff cortex that is sitting on a TM with equal stiffness to its cytoplasm. However, this situation (E_{TM}= $E_{cytoplasm}$) is not much likely to occur in actual biological tissues. P5 was also showed to be present in both periphery and nuclear regions. Our conclusion for P5 is that it could represent either the indentation on the peripheral region of a cell with stiffer cortex and TM or, perhaps this is a region where the cell was damaged during dissection, and these values characterize the matrix alone.

In contrast to P1 and P5, the model failed to generate patterns that were comparable to P2-P4. We speculate that this is due to significant heterogeneity of the TM that is composed of multiple layers of different structure and mechanics as described in previous section and future studies need to be done for addressing this.

Chapter 5: The Effect of Dexamethasone on SC Cell Mechanics and the Interpretation of Cell Mechanical Measurements

5.1 Introduction

We described the role of dexamethasone in steroid-induced glaucoma in chapter 1 and hypothesized that the pressure elevation caused by dexamethasone might be due to increased stiffness in SC cells. In this chapter, we describe studies whose aims were to understand the effect of dexamethasone treatment on the cytoskeleton and mechanics of SC cells using imaging techniques and the techniques described in chapter 2. Our AFM studies showed that sharp tips, which characterize the cortical regions of cells (Vargas-Pinto et al. 2013), measured significantly higher Young's modulus (E) for dexamethasone-treated SC cells whereas rounded probes, that characterize the subcortical cytoskeleton, did not show a significant change. Data from OMTC showed a marginally significant decrease in calculated modulus (g) of the dexamethasone-treated SC cells while TFM studies revealed a marginally significant increase in SC cell traction forces upon following dexamethasone treatment. These observations suggested that measurements from each of these techniques may be influenced by probe geometry and also the mechanics of the region it associates with. This was especially true for OMTC that has previously been described as a technique to characterize cortical stiffness (Guo et al. 2013), in contrast to our measurements.

Based on this, we developed a finite element model to characterize OMTC measurements in cells whose cortical stiffness is much greater than that of their underlying cytoskeleton, and compared these model predictions to those of our finite element model of AFM measurements in such cells. The models suggested that OMTC does not characterize cortical stiffness. We validated this conclusion by experimental studies in which we used cytoskeletally-active agents to induce the expression of RhoA and α-actinin in SC cells and measured their mechanical effects using AFM, OMTC, and TFM. We also explored the role of vimentin in cell mechanics. The latter studies were important as Guo et al. previously used OMTC to examine the cortical mechanics of wild type (WT) and vimentin knock out (KO) mouse embryonic fibroblasts (MEFs) and concluded that vimentin doesn't play a role in cortical cell mechanics (Guo et al. 2013) .

We found that OMTC behaves similar to AFM rounded probes and mainly characterizes the subcortical mechanics, consistent with our modeling results. However, we also found that OMTC measurements are influenced by bead embedding depth, which may explain differences found between OMTC and AFM measurements in cells.

5.2 Methods

5.2.1 Cell culture

Schlemm's Canal (SC) endothelial cells were isolated and cultured from post mortem enucleated human eyes at the laboratory of Dr. Stamer at Duke University

(Karl et al. 2005). Eyes with history of laser or anterior segment surgery and also eyes with any disease except glaucoma were excluded. Confluent cells were shipped overnight to our laboratory in T-25 flasks containing SC cell standard culture media, DMEM/Low glucose (Life Technologies, Grand Island, NY) with 10% fetal bovine serum (Atlanta Biologicals, Norcross, GA) and 1% penicillin/streptomycin (Life Technologies, Grand Island, NY). The media was changed upon arrival. SC cells between passages 3-5 were used for all experiments. The effect of passaging on mechanical properties of SC cells has been examined previously where cells were found to have consistent mechanical behavior up to passage 6 (Zhou et al. 2012). In addition, to confirm the consistency of the data across all passages, certain criteria were established for cells as follows: (i) cell size not greater than 20% of the average (100-150 μm long) (ii) doubling time per cell line (between 2-3 days) no longer than 20% of average doubling time when cell line was first received.

Table 5.1 provides the information on SC cell strains used in our studies. Cells were characterized glaucomatous based on the medical background and treatment information received from donor’s ophthalmologists, measured outflow facility, and optic nerve counts, with this information provided by Dr. Stamer's laboratory. The average number of optic nerve fiber count is around $1x10^6$ in normal eyes where this number decreases dramatically in eyes with glaucoma (Jonas et al. 1992).

Table 5.1: SC Cell strains used for this study.

Cell Line	Donor Age	Tissue Source	Glaucoma	Outflow Facility	Optic Nerve Fiber Count
SC 57g	78	Whole Eye	Yes	NA	NA
SC 60	58	Cornea	No	NA	NA
SC 62g	66	Whole Eye	Yes	NA	NA
SC 64g	78	Whole Eye	Yes	0.16	238,978
SC 67	44	Whole Eye	No	0.2	NA
SC68	30	Cornea	No	NA	NA
SC 69	45	Cornea	No	NA	NA
SC 71	44	Whole Eye	No	0.159	NA
SC 73	37	Cornea	No	NA	NA
SC 76	59	Cornea	No	NA	NA
SC 78	77	Whole Eye	No	NA	NA

NA: Not available, Outflow Facility unit is μL/min/mmHg.

Wild type (WT) and vimentin knock out MEFs were received from the laboratory of Dr. Goldman at Northwestern University. These cells are extracted from mouse embryo, immortalized based on standard protocols and can be used for around 15-20 passages before changing their phenotypic behavior (Xu 2005). MEFs were cultured in Dulbecco's minimal essential medium (Life Technologies, Grand Island, NY) supplemented with 10% fetal calf serum (FCS) (Atlanta Biologicals, Norcross, GA), 5 mM nonessential amino acids (NEAA) (Life Technologies, Grand Island, NY), and 1% penicillin/streptomycin (Life Technologies, Grand Island, NY).

All cell cultures were maintained under standard cell culture condition in a humidified incubator at 5% CO_2 and 37 °C, and media was changed every other day. Cells were passaged when they were around 80% confluent. For passaging, cells were washed with PBS (Life Technologies, Grand Island, NY) to remove the serum, then treated with trypsin-EDTA 0.25% (Thermo Fischer Scientific, Grand Island, NY), and passaged at a ratio of 1:3.

5.2.2 Confocal imaging and western blot studies

Normal and glaucoma SC cells were seeded onto glass cover slips (22×22 No. 1.5, Thermo Fischer Scientific, MA) 48 hours prior to fixation and then stained for confocal experiments. Cells were washed with PBS before fixation to remove the media. 100% methanol (Sigma, Milwaukee, WI) was used as the fixative for experiments where vimentin was the only cytoskeletal filament to be stained (Mendez et al. 2010). For all other immunofluorescent experiments, 4% paraformaldehyde (Electron Microscopy Sciences, Hatfield, PA) was used (pH=7.4) (Lei, Rajabi, et al. 2011). Methanol fixation was done by incubating cells with precooled methanol for 10 minutes inside a −20°C freezer, and for paraformaldehyde fixation, cells were fixed for 10 minutes at room temperature. Fixed cells were then rinsed with PBS twice, permeabilized with 0.2% Triton (Life Technologies, Grand Island, NY) for 5 minutes, then rinsed again with PBS twice. For cases where the secondary antibody was raised in goat (phosphorylated myosin and vimentin staining), samples were blocked in 10% normal goat serum (Life Technologies, Grand Island, NY) for 20 minutes to block for the non-specific binding prior to incubation with primary antibody. For all other cases, cells were incubated with Image-iT® FX Signal Enhancer (Life Technologies, Grand Island, NY) for 20 minutes prior to incubation with primary antibody. Cells were then rinsed with PBS twice and incubated with primary antibodies.

For dexamethasone experiment, cells were stained for F-actin (30 minutes incubation with one volume per test of Alexa Fluor® 568 Phalloidin, Life Technologies, Grand Island, NY), vimentin (30 minutes incubation with one volume per test of Alexa Fluor® 488 Conjugated Vimentin (D21H3) XP® Rabbit mAb, Cell Signaling Technology, Danvers, MA), the nucleus (15 minutes incubation with Hoechst 33342 (1:10000), Thermo Fischer Scientific, Grand Island, MA), and phosphorylated myosin (overnight incubation at 4°C with Phospho-Myosin Light Chain 2, Ser19 (1:100) followed by two washes with PBS and one hour incubation with goat anti rabbit IgG (H+L) Alexa Fluor 488 (1:400), Cell Signaling Technology, Danvers, MA). For RhoA and α-actinin experiments, cells were stained for F-actin (30 minutes incubation with one volume per test of Alexa Fluor® 568 Phalloidin), and the nucleus (15 minutes incubation with Hoechst 33342 (1:10000)).

Stained slides were mounted on microscope glass slides (Thermo Fischer Scientific, Grand Island, NY) using 6μl of fluorescence mounting medium (Dako, Carpinteria, CA) and cured in the dark at 4° for 24 hours. Afterwards, the slide edge was covered with nail polish (Electron Microscopy Sciences, Hatfield, PA) and cured at dark at 4° for one day.

A Zeiss 510 LSM inverted two-photon confocal microscope with objective lens of 10x (NA=0.3), 20x (NA=0.8), and 40x (water immersion, NA=1.2) and excitation sources of Ar (458, 488, 514 nm), HeNe (543 nm), HeNe (633 nm), 2-photon (690-1024 nm) was used to create confocal images from the samples (Carl Zeiss, Thornwood, NY). Images were created based on the optimal optical section. The thickness of the optical sections and laser intensity was kept constant during each experiment.

Western blot analysis was performed to examine changes in cytoskeletal protein expression for dexamethasone, α-actinin and RhoA experiments. For dexamethasone experiment, beta actin, alpha smooth muscle actin (SMA), vimentin, and tubulin were probed. There were four dexamethasone concentration groups (0, 0.01, 0.1 and 1μM) where each had a control with the equivalent level of ethanol concentration. A multiple linear regression model (Chapter 2) was then used to analyze the effect of dexamethasone and ethanol concentration on expression level of mentioned proteins (see 5.2.7). The loading volume for each well was 10μg and tubulin was the loading control. For alpha-actinin and RhoA infection studies, beta actin, actinin, tubulin, and vimentin were probed; in the α-actinin studies, gfp-labeled α-actinin was separately identified. The loading for each well was 10μg. However, the large variations in beta actin and tubulin levels in western blot indicated that they were unreliable loading controls. To address this issue, data for each well was normalized based on the total protein in that well before making comparisons. Kristin Perkumas performed all western blot studies in Dr.Stamer's laboratory at Duke University. Image Studio 4.0 was used to measure the signal intensity from western blot images (intensity extraction and analysis courtesy of Dr. Rudolf Fuchshofer, Universität Regensburg).

5.2.3 AFM force measurements

Cells were seeded on 60mm petri dishes (VWR, Batavia, IL) for AFM experiments. A BioScope II with NanoscopeV controller (Bruker, Santa Barbara, CA) coupled to an inverted fluorescent microscope with 10x (NA=0.3), 20x (NA=0.8) objective lens was used to make these measurements (Carl Zeiss, Thornwood, NY). Sharp and rounded probes were used to characterize the cortical and subcortical stiffness of cells as described in chapter 2. Indentation depths were kept below 500 nm to avoid any substrate effect (Rico et al. 2005) and measurements were done on regions well away from the nucleus and periphery.

5.2.4 Dexamethasone studies

To examine the effect of dexamethasone on the biomechanical behavior of SC cells, two normal SC cell strains (SC71, SC76) and two glaucomatous strains (SC57g, SC64g) were treated with dexamethasone. Fresh stock solution of 1mM dexamethasone (Sigma Aldrich, Milwaukee, WI) was prepared in ethanol as the vehicle. Four AFM dishes and confocal imaging cover slips were prepared for each strain to treat cells with 0, 0.01, 0.1 and 1μM concentrations of dexamethasone respectively. The ethanol concentration was 1μM in all groups for AFM, OMTC, and TFM studies. For western blot studies, each dexamethasone treatment group had a control with the same ethanol concentration as dexamethasone, but no dexamethasone. The treatment was continued for seven days to be consistent with the perfusion studies for glucocorticoid induced ocular hypertension (Mao et al. 2011) that require this time period to show an effect on outflow resistance. Media was replaced every other day and cells were nearly confluent at the end of the treatment.

After AFM, some samples (SC 76 and SC 57g) were then fixed and stained for imaging studies as described in 5.2.2. OMTC and TFM studies were performed by Dr. Chan Park. SC cells were seeded to 96 well plates (Thermo Fischer Scientific, Grand Island, NY) at a density of 2000 per well and were kept in SC culture media (containing 10%FBS and 1% pen/strep) throughout the experiments. Poly-L-lysine (PLL) coated beads were used for OMTC and the gel stiffness (E) was 1.8 kPa for the TFM studies.

5.2.5 Induction of α-actinin and RhoA expression

Four normal (SC69, SC71, SC73, SC76) and one glaucomatous (SC57g) cell strains were transfected with (i) an adenovirus with a Ubiquitin promoter driving GFP, (ii) a Ubiquitin promoter driving α -actinin with a GFP tag, or (iii) a Ubiquitin promoter driving RhoA; a fourth group (iv) consisting of non-transfected cells (no virus) was also used. Group (iv) served as a control for group (i) and the group (i) cells served as a control for both groups (ii) and (iii). However, the RhoA group only contained the ubiquitin promoter vector, but not the GFP tag, as opposed to the α-actinin group that had both. This has been a caveat in designing controls for the RhoA group and could have introduced additional variability to our results.

Kristin Perkumas performed the transfection procedure and cells were shipped to us in T-25 flasks overnight. The SC76 cells sent did not include group iii (RhoA promoter) and the SC 71 cells did not include group iv (non-transfected cells). AFM sharp and rounded probes were used to measure stiffness in single cells in each group and then imaging cover slips (SC76 and SC 57g) were fixed and stained as described in section 5.2.2.

OMTC and TFM studies were conducted by Dr. Chan Young Park who performed the experiments on one normal cell strain (SC 71) that included all four groups. SC cells were seeded to 96 well plates (Thermo Fischer Scientific, Grand Island, NY) at a density of 2000 per well and were kept in SC culture media (containing 10% FBS and 1% pen/strep) throughout the experiments. PLL-coated beads were used for OMTC and the gel stiffness (E) was 1.8 kPa for the TFM.

5.2.6 MEFs studies

We probed confluent WT and KO cells using AFM sharp and rounded probes using the protocol described above. Two sets of TFM and three sets of OMTC experiments were conducted by Dr. Chan Park. For the first TFM experiment, cells were seeded on 96 well plates (Thermo Fischer Scientific, Grand Island, NY) at low (1000/well) and high (10000/well) density and measurements were done in the presence and absence of serum (10%) in MEFs culture media (see 5.2.1). The Young's modulus of the gel was 1.8kPa. For the second TFM experiment, the seeding density was high (10000/well) and the Young's modulus of the gel was 8kPa. Also, the cells were tested in presence and absence of calf serum (overnight) with and without media replacement an hour before the experiment.

For the first and third set of OMTC experiments, cells were seeded to 96 well plates (Thermo Fischer Scientific, Grand Island, NY) at high density (10000/well) and tested in presence and absence of serum (10%). In both cases, the media was replaced with fresh media before measurements were made. A second OMTC experiment was conducted to replicate the experimental conditions of Guo et al. (Guo et al. 2013) where cells were seeded at very low densities (400/well).

For the first and second set of OMTC experiments only PLL-coated beads were used whereas for the third set both PLL and RGD coated beads were used.

5.2.7 Statistical analysis

The general statistical approach used is described in 2.5. In addition, for the dexamethasone experiment, a standard linear regression model was used to assess the effect of dexamethasone concentration, ethanol concentration, and disease status (normal or glaucoma) on stiffness, traction, or protein expression in SC cells. As mentioned in 5.2.4, ethanol concentration was constant for all groups in AFM, OMTC, and TFM studies, which rules out the effect from different ethanol concentration on AFM measurements. Hence, the model for these studies was:

$$\mathrm{E} = \alpha + \beta_1[\mathrm{Dex}] + \beta_2[\mathrm{Glaucoma}] + \beta_3[\mathrm{Glaucoma}] * [\mathrm{Dex}] \qquad (1)$$

where E is the modulus or traction force, “Dex” is the concentration of dexamethasone, and “Glaucoma” is equal to 1 for glaucomatous and 0 for normal cells. For the western blot analysis, two new terms “[Etoh]” and “[Etoh]*[Glaucoma]” were introduced to account for the tentative effects from variable ethanol (vehicle) concentration. The equation for this case was defined as:

$$\mathrm{I} = \alpha + \beta_1[\mathrm{Dex}] + \beta_2[\mathrm{Glaucoma}] + \beta_3[\mathrm{Glaucoma}] * [\mathrm{Dex}] + \beta_4[\mathrm{Etoh}] + \beta_5[\mathrm{Etoh}] * [\mathrm{Glaucoma}] \qquad (2)$$

where I is the signal intensity measured from western blot images, “Etoh” is the ethanol concentration, and “Dex” and “Glaucoma” are the same as in equation (1).

The regression analysis was done in backwards fashion where we started testing for significance of all betas and left out non-significant ones until the final correlation was obtained.

5.2.8 Finite Element Modeling

A. AFM Model

The average height around the nucleus region for SC cells in culture is reported to be around 5µm (Vargas-Pinto et al. 2013). Thus, the cell was modeled as a bilayer disc with a cortex (400nm) above a cytoplasm with a thickness of 4.6µm. The radius of the disc was determined to be 10µm based on the criteria defined in 2.4. The radius of AFM probes varied from 0.4µm to 5µm. The Young’s Modulus of the cytoplasm was set to be 3 kPa (Mijailovich et al. 2002) while the modulus of the cortex was varied between 3 to 300 kPa. Figure 5.1 shows the schematic for AFM simulations.

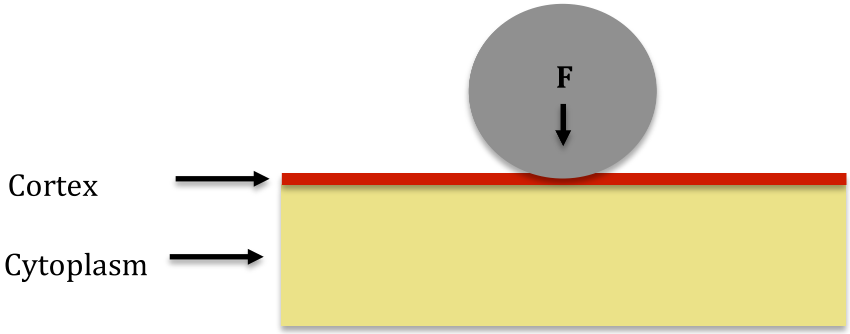

Figure 5.1: Schematic for the AFM simulations. A rounded AFM probe indenting the cell with a cortex and cytoplasm.

B. OMTC Model

To study the effect of cortex stiffness on OMTC measurements, we followed the approach of Mijailovich et al (Mijailovich et al. 2002) who used a 3D finite element model to examine the effect of cell height and bead embedding depth on OMTC measurements. In their model, the cell was assumed as a homogenous material. We extended their model to examine the effect of a cortex than was of greater stiffness than the underlying cytoplasm. Like our AFM model, cell had a cortex and a cytoplasm with 4.6μm thickness. The radius of the cell was chosen as 22.5 μm based on the criteria in 2.4. We further verified that increasing the radius by 50% did not make a significant change to the results (smaller than 0.13% of all measured parameters), but significantly increased the computational time by as much as 40%.

The ferromagnetic bead diameter was 4.5μm and bead was bound to the cortex. We examined embedding depth of the bead from 10-50% of the bead diameter (Fabry et al. 2001)(Zeng et al. 2010). The magnetic field applied in OMTC was modeled as a torque applied to the center of the bead causing the bead rotate around its central axis.

We allowed the Young's Modulus of the cytoplasm and cortex to be the same as in our AFM simulations (cytoplasm= 3 kPa; cortex varied between 3 to 300 kPa) to make our studies comparable to Mijailovich et al (Mijailovich et al. 2002) resulting in a cortex to cytoplasm stiffness ratio, $\frac{\mathrm{E_{Cortex}}}{\mathrm{E_{Cytoplasm}}}$, of 1-100. Figure 5.2 illustrates the schematic for the OMTC model.

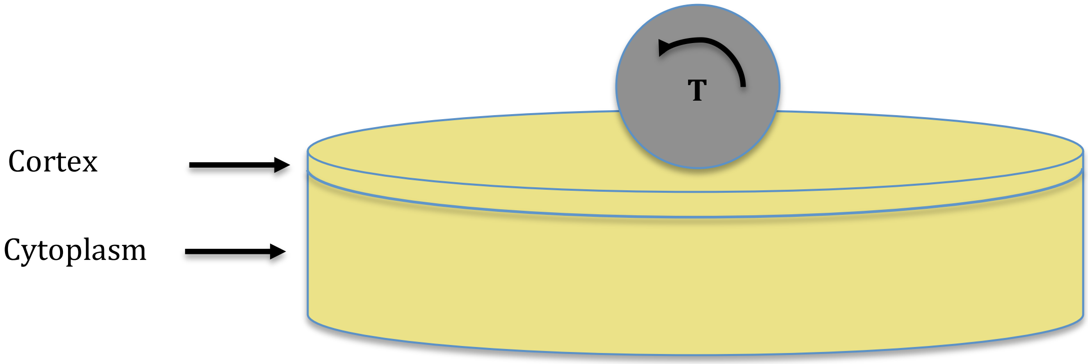

Figure 5.2: Schematic for the OMTC model. The bead is bound to cell cortex and an electromagnetic torque causes bead center to rotate along its central axis.

C. Boundary conditions

The bottom surface of the cell for both AFM and OMTC was pinned for zero displacement. Cortex was tied to the cytoplasm to create a no-slip boundary condition between the cortex and cytoplasm (Mijailovich et al. 2002). The maximum indentation for AFM was set to 400nm to match the data from the actual AFM experiment.

D. Mesh validation and element selection

Element selection and mesh validation was done as described in 2.4. The smallest and largest element lengths were 10nm and 400nm respectively. The element width (along the cell height direction) was kept constant at 20nm in the cortex and a bias factor was introduced to the width in the cytoplasm where the smallest and largest elements were 20nm and 200nm respectively. The initial guess for element size was based on previous modeling studies (Vargas-Pinto et al. 2013). Table 5.2 shows the three examined cases to find the optimal element size for simulations.

Table 5.2: Examined cases for finding the optimal mesh size for simulations.

	Cortex		**Cytoplasm**	
Case	**Element Length (nm)**	**Element Width (nm)**	**Element Length (nm)**	**Element Width (nm)**
1	10-400	10	10-400	10-200
2	20-400	20	20-400	20-200
3	50-400	50	50-400	50-200

The extracted force-indentation curves for various element sizes for the smallest AFM probe (R=400nm) and torque-bead center displacement curves for OMTC in the case of $E_{cortex} = E_{cytoplasm}$ are shown in Figure 5.3. The error between the smallest (case 1) and largest (case 3) element size was 0.023% and 0.05% for AFM and

OMTC respectively. However, increasing minimum element size to 100nm introduced errors as large as 1%. As a result, case 3 was chosen for the mesh.

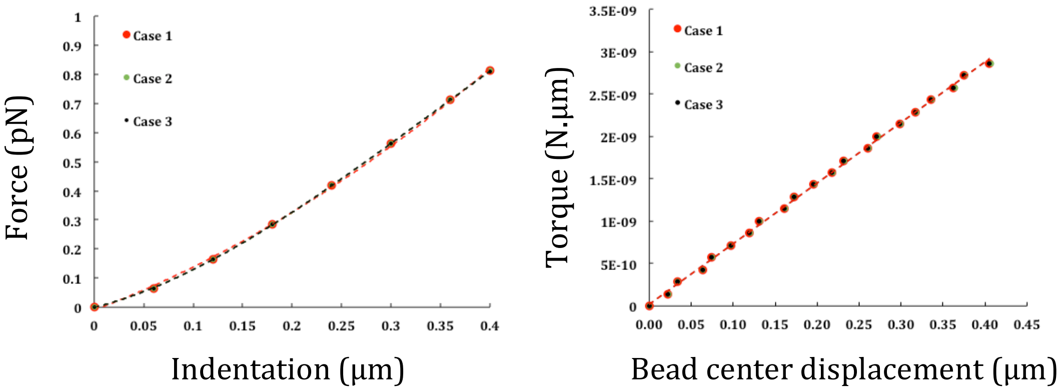

Figure 5.3: Mesh validation for AFM and OMTC simulations. Results are shown for 3 different mesh sizes for AFM probe (R=0.4μm) and OMTC (embedding depth of 10% bead diameter) for the case $E_{cortex} = E_{cytoplasm}$.

E. Calculation of the apparent modulus and effect of substrate

We calculated $E_{apparent}$ for AFM and OMTC simulations as described in 2.4. However, when calculating $E_{apparent}$ for the AFM simulation, we use the Hertz model that is for deformation of a semi-infinite domain and does not include substrate effects such as we will have in our simulations. To account for this effect, we used a correction factor due to Dimitraidis et al. (Dimitriadis et al. 2002) for analyzing indentations on incompressible materials using rounded probes, where the term in brackets is the proposed correction factor for the Hertzian equation:

$$F = \frac{16E}{9} R^{1/2} \delta^{3/2} [1 + 1.133\chi + 1.283\chi^2 + 0.769\chi^3 + 0.0975\chi^4] \qquad (3)$$

where F=force, E= Young's Modulus, δ=indentation, R=radius, $\chi = \sqrt{R\delta}/h$ and h is cell thickness.

We validated this equation by calculating the correction factor and compared the results to those from our finite element model as shown in Table 5.3 for the case when $\frac{E_{Cortex}}{E_{Cytoplasm}} = 1$. As expected, larger rounded probes are more influenced by the substrate as compared to smaller ones. In addition, the comparison shows that for probes with a radius of 1.5µm and larger, there is a very good agreement between our model and Dimitriadis et al. However, as the probe radius becomes smaller (1µm or less), the two models start to deviate and the difference between the correction factors increases. This is likely due to the fact that Dimitriadis et al.'s proposed correction factor is based on the Hertzian model that assumes a small ratio of indentation to indenter radius, which may not be the case for indenters with radius of smaller than 1.5µm. As a result, we used the correction factors from our FEM studies to correct for the substrate effect in our modeling studies.

Table 5.3: Correction factors for the substrate effect.

R (µm)	δ (µm)	h (µm)	Correction factor (Dimitriadis et al.)	Correction factor (Our FEM studies)	Difference (%)
5	0.4	5	1.44	1.44	0.08
2.25	0.4	5	1.27	1.23	2.88
1.5	0.4	5	1.21	1.17	2.92
1	0.4	5	1.17	1.10	5.30
0.75	0.4	5	1.14	1.07	6.03
0.4	0.4	5	1.10	0.97	12.06

Like AFM, the substrate effect can influence the simulations for OMTC measurements as well. However, since we used ABAQUS to calculate the apparent modulus for OMTC simulations, the substrate effect is already taken into account and no correction factor was necessary.

F. Reproducing the results from Mijailovic et al.

Mijailovich et al. previous modeled OMTC measurements assuming a homogenous cell. To verify our model, we first aimed to replicate the results by Mijailovic et al. and compared our results to theirs for the case when $E_{cortex}=E_{Cytoplasm}$. Mijailovic et al. determined the bead center lateral displacement (d) (see section 2.2.1) and thereby calculated the apparent shear modulus as:

$$G_{apparent} = \frac{T}{6d^*} \tag{4}$$

where T is the torque per volume (60 Pa) exerted on the bead and d* is the ratio of bead center displacement (d) to bead radius (R=2.25μm). They then relate $G_{apparent}$ to the absolute shear modulus ($G_{cell=}$1kPa: note that G=E/3) as:

$$G_{app} = \beta G_{cell} \tag{5}$$

where β is a geometrical factor that depends on bead embedding depth. Note that G_{app} is not analogous to E_{app} as the former is used to examine the effect of bead embedding depth while the latter is used to examine the effect of cortex stiffness. We followed the same approach as Mijailovic et al. and calculated the coefficient β for embedding depths of 10, 15, 20, 25, 35, 45, and 50% in cell with 5μm height.

Figure 5.4 shows the results from Mijailovic et al. and for our study for embedding depths of 10-50% of the bead diameter. In general, the plot shows good agreement between our data and the data from Mijailovic et al. However, the values from

Mijailovic et al. are slightly higher, especially at higher indentation depths. This could be due to the fact that we used ABAQUS for the FEM analysis where as they used the finite element program PAK. The plot demonstrates that the calculated values for the absolute shear modulus (G) strongly depend on the embedding depth and can differ by more than an order of magnitude depending on the estimations for the bead embedding depth.

To further investigate the effect of bead embedding depth, we sought to calculate the coefficient β for the cases where $E_{Cortex} \neq E_{Cytoplasm.}$ We followed Mijailovic et al. and defined β as:

$$\beta = (G_{apparent})/(G_{apparent})_{50\%\ embedding\ depth} \tag{6}$$

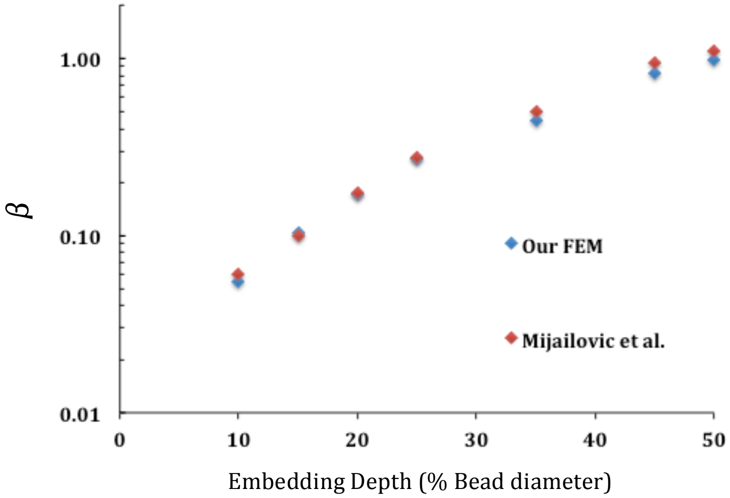

Figure 5.4: Calculated β coefficients from our FEM model and Mijailovic et al.

5.3 Finite Element Modeling Results

We first describe the results from the finite element modeling studies of AFM and OMTC, as they will assist in the interpretation of our experimental data.

5.3.1 AFM

FEM was used to study how the presence of a stiff cortex and geometry of the tip influences the modulus measured in AFM studies. The strain fields for the cases of $E_{cortex}/E_{cytoplasm} = 1$ and 50 for an AFM probe with 4.5μm diameter are shown in Figure 5.5.

From the figure, it can be seen that the strain field for $E_{cortex}/E_{cytoplasm}=1$ is more localized to the region near the cortex, as compared to $E_{cortex}/E_{cytoplasm}=50$ where it extends further into the cytoplasm.

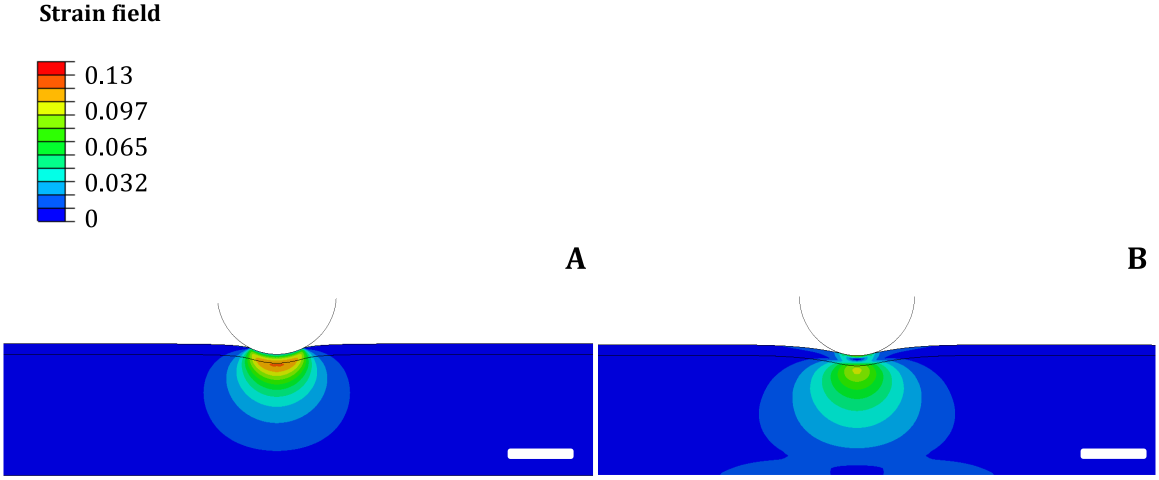

Figure 5.5: The strain field distribution in cortex and cytoplasm for cases where $E_{cortex}/E_{cytoplasm}=1$ [A] and 50 [B]. Tip radius is 2.25μm and the scale bar is 2.25μm.

Figure 5.6 shows a set of force indentation curves [A] and their corresponding apparent modulus plots [B] for the tip radius of 5μm. The figure shows that increasing in cortex stiffness elevates the magnitude of the force required for indentations, as expected, but the effect is relatively weak. From plot [B], one could see that higher cortex stiffness leads to higher values for the apparent modulus, but this effect is reduced for deeper indentations. The insert in [B] shows $E_{apparent}/E_{cytoplasm}$ for higher values of indentation. From the insert, it can be seen that the apparent modulus at an indentation of 400nm for $E_{cortex}/E_{cytoplasm}=100$ is approximately twice as much as $E_{cortex}/E_{cytoplasm}=1$.

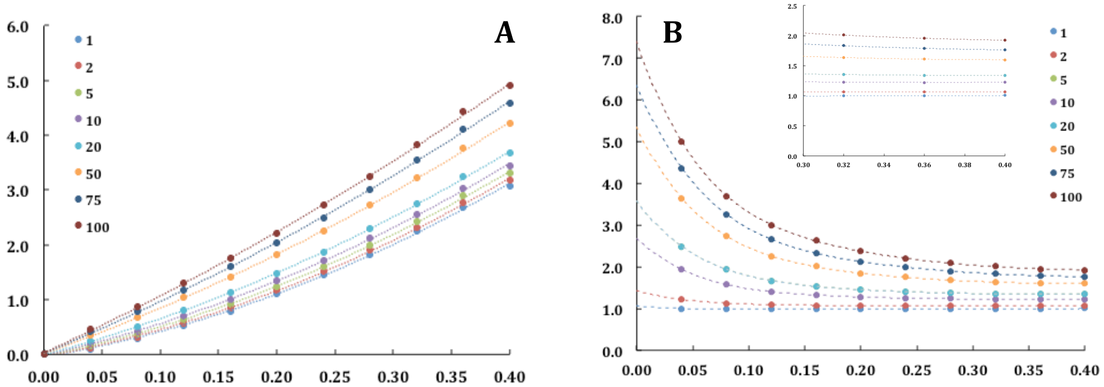

Figure 5.6: Force versus indentation [A] and $E_{apparent}/E_{cytoplasm}$ versus indentation [B] plot for R=5μm rounded tip model. Each curve corresponds to a different value of $E_{cortex}/E_{cytoplasm}$ ranging from 1 to 100.

Figure 5.7 shows the results for the strain fields for probes of R =0.4μm and 5μm diameter for the case of $E_{cortex}/E_{cytoplasm}$ =1. From the figure, it is evident that the strain field for 5μm probe extends much deeper into the cytoplasm as compared to that of 0.8μm, which is almost confined to the cortex and the immediately surrounding region. The strain values are higher for the smaller probe (R=0.4μm), with a maximum strain of approximately 32%, while for the 5μm probe it is approximately 8%. This is consistent with our previous studies where we found significantly higher strains for a sharp probe as compared to a larger rounded one (Vargas-Pinto 2011).

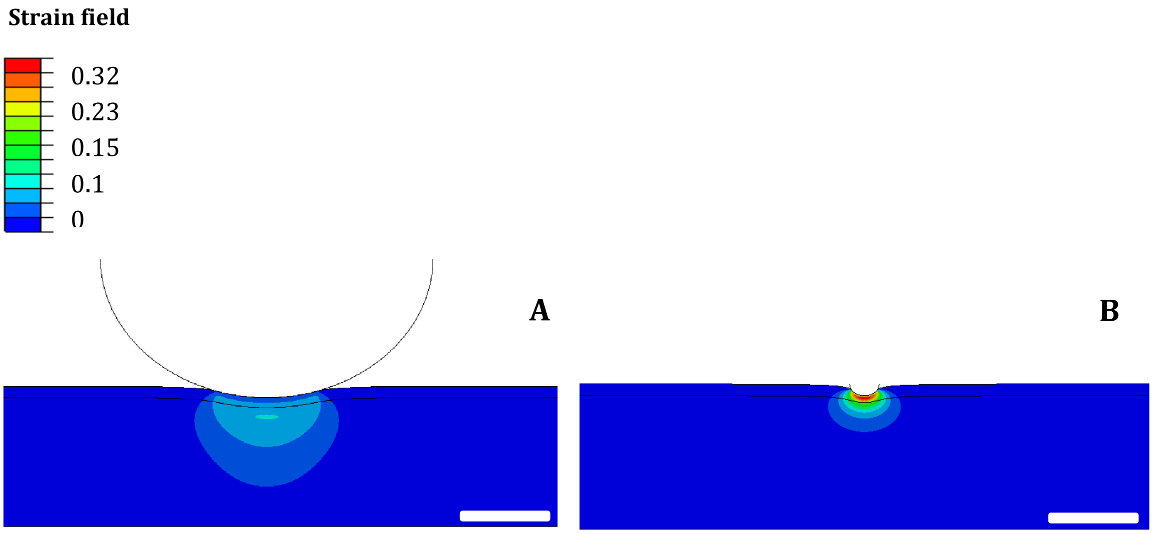

Figure 5.7: Strain field distribution in cortex and cytoplasm for R=5µm [A] and 0.4µm [B] rounded probes when $E_{cortex}/E_{cytoplasm}$ =1. The strain field is almost confined to the cortex for 0.8µm tip while it spreads through the cytoplasm for the 5µm. In addition to strain distribution, the smaller probe has significantly higher value of maximum strain compared to the larger probe. Scale bar is 3µm.

Figure 5.8 shows $E_{apparent}/E_{cytoplasm}$ as a function of $E_{cortex}/E_{cytoplasm}$ for all tip radii demonstrating that the cortex stiffness has the least influence on largest (5µm) AFM probe, consistent with our previous results (Vargas-Pinto et al. 2013). The cortex effect increases for smaller tip radii where the tips smaller than 1µm are strongly influenced. For example, when $E_{cortex}/E_{cytoplasm}$ = 50, the value of $E_{apparent}/E_{cytoplasm}$ for the smallest tip (R=0.4µm) is almost 3 times of that for the largest one (R=5µm). This is consistent with our previous findings that sharp tip AFM probes are much more influenced by cortex stiffness than are larger rounded probes (Vargas-Pinto et al. 2013). We did not investigate sharp tips in this study due to numerical issues for indentations deeper than 80nm. (Ng et al. 2007)(Vargas-Pinto et al. 2013).

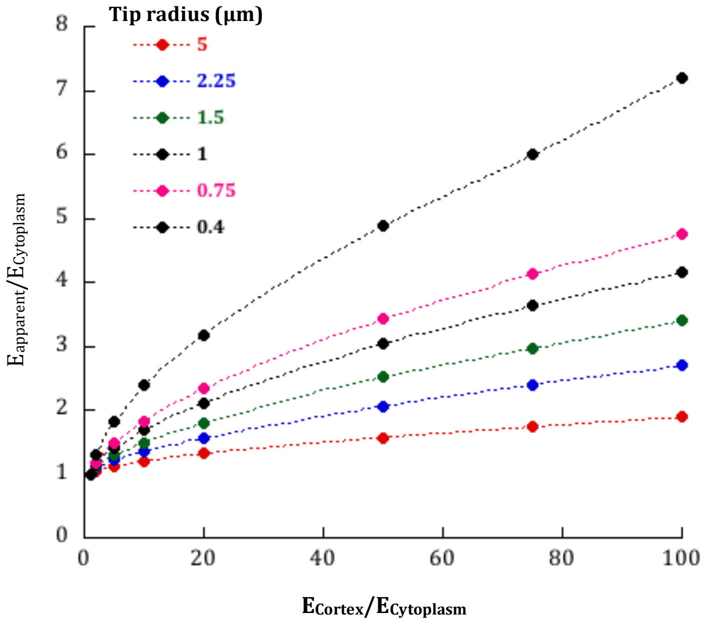

Figure 5.8: Effect of cortex stiffness and tip radius (0.4μm-5μm) on AFM measurements. Larger rounded AFM probes are less influenced by the cortex whereas smaller probes demonstrate more sensitivity.

5.3.2 OMTC

Figure 5.9 shows the strain fields for a 4.5μm diameter bead that is embedded at 10% of its diameter when $E_{cortex}/E_{cytoplasm} = 1$ [A] and 50 [B]. The figure shows that the strain field for $E_{cortex}/E_{cytoplasm}=50$ extends into the cytoplasm to a greater extent as compared to $E_{cortex}/E_{cytoplasm}=1$, indicating the former is relatively less influenced by cortical stiffness.

We then sought to examine the effect of bead embedding depth where we calculated the values for β (as described in 5.2.8) and plotted those (Figure 5.10) as a function of bead embedding depth when $E_{cortex}/E_{cytoplasm} = 50$ [Panel A] or 1 [Panel B].

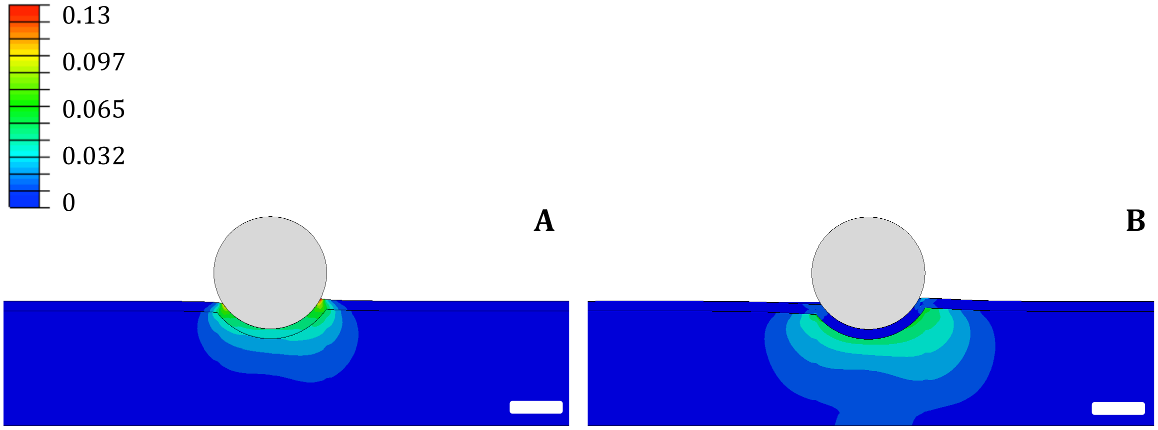

Figure 5.9: The strain field distribution in cortex and cytoplasm for cases where $E_{cortex}/E_{cytoplasm}$=1 [A] and 50 [B]. The strain field is more spread through the cytoplasm in [B] indicating a relatively smaller effect from cortex stiffness on $E_{apparent}$. Scale bar is 2.25µm.

The plot for $E_{cortex}/E_{cytoplasm}$ = 50 (Figure 5.10A) demonstrates a biphasic response as the effect from the cortex initially decreases as the embedding depth is increased and then rises again at an embedding depth of roughly 35%. The data shows that the embedding depth still influences $E_{apparent}$ in the presence of a stiff cortex. However, the extent of this influence is notably lower compared to $E_{cortex}/E_{cytoplasm}$ = 1 (Figure 5.9B), as first described by Mijailovich et al., where embedding depth could affect $E_{apparent}$ by more than an order of magnitude.

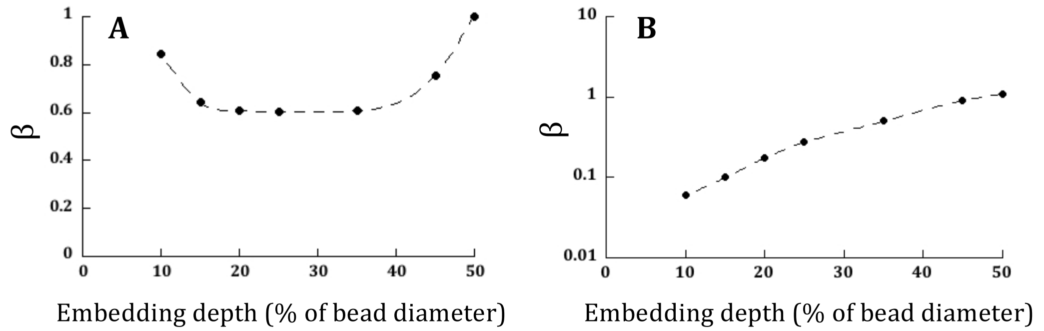

Figure 5.10: The effect of embedding depth on apparent modulus for the case of E_{cortex}/ $E_{cytoplasm}$=50 [A] and E_{cortex}/ $E_{cytoplasm}$=1 [B]. Overall, $E_{apparent}$ is less sensitive to bead embedding depth when cortex is much stiffer than the cytoplasm.

The apparent moduli for three embedding depths are plotted in Figure 5.11. Interestingly, the lowest effect of the cortex effect on $Ea_{pparent}$ occurs at 25% embedding depth, while stronger effects are seen at both 10% and 50% embedding (similar behavior is seen in 5.10A). This may be caused by deformation only in the cortex for shallow embedding depths, and significant cortical deformations for large embedding depths while in between these limits, the cytoplasm has greater influence. Furthermore, similar to AFM rounded probes (Figure 5.8), at all embedding depths, the influence from cortex stiffness on $E_{apparent}$ becomes less significant as the ratio of $E_{cortex}/E_{cytoplasm}$ increases.

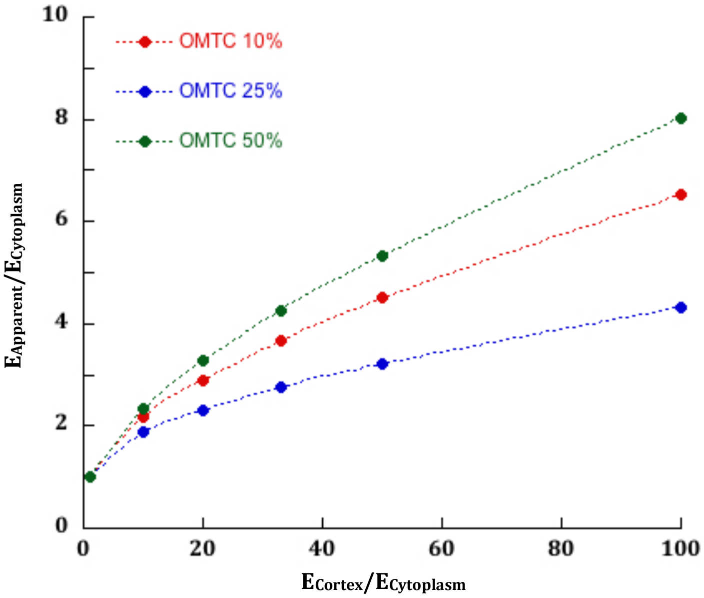

Figure 5.11: Effect of cortex stiffness on OMTC measurements for embedding depths of 10%, 25%, and 50% of the bead diameter. As seen with AFM, there is a reduced relative influence of cortex stiffness on $E_{apparent}$ as E_{cortex} increases.

5.3.3 Comparing AFM rounded probes and OMTC

Comparing the results from AFM to OMTC (Figure 5.12) shows that measurements from AFM larger rounded probes and OMTC are far less influenced by the cortex stiffness as compared to smaller AFM round probes and especially an AFM sharp probe. However, when comparing the OMTC to AFM rounded probes [B], overall, OMTC measurements are somewhat more influenced by the cortex stiffness as compared to AFM larger rounded probes. From these figures, one may conclude that while AFM sharp tips measure cell cortical mechanics and larger rounded tips probe the subcortical region, OMTC measurements are influenced by both cell body and cortex and thus, offer an aggregate modulus for the cell.

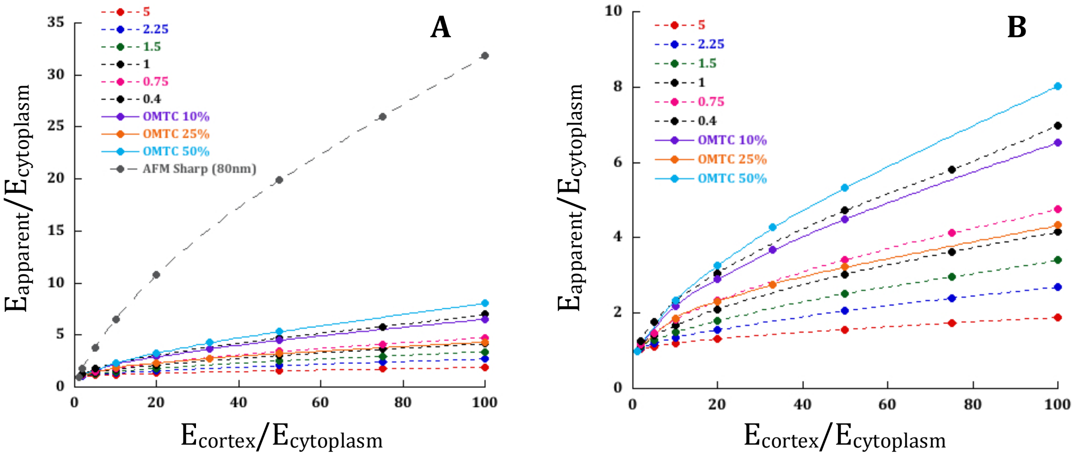

Figure 5.12: Comparison between the AFM and OMTC measurements with [A] and without [B] sharp tip data. (Sharp tip data from Vargas-Pinto et al., 2014, and are for 80nm indentation). AFM rounded probe radius varies between 0.4-5µm and indentation depth is 400nm. OMTC bead diameter is 4.5µm and the embedding depth changes from 10-50% of the bead diameter.

5.4 Experimental Results

5.4.1 Dexamethasone experiment

A. Imaging

Figure 5.13 shows the distribution of F-actin and P-myosin in confluent SC cells treated with dexamethasone (1µM) compared to controls. The image shows that while stress fibers and cortex are present in both control and treated cells (Figure 5.13A,D), the presence of F-actin tends to be more prominent at the cortex of treated cells (white arrows in 5.13D).

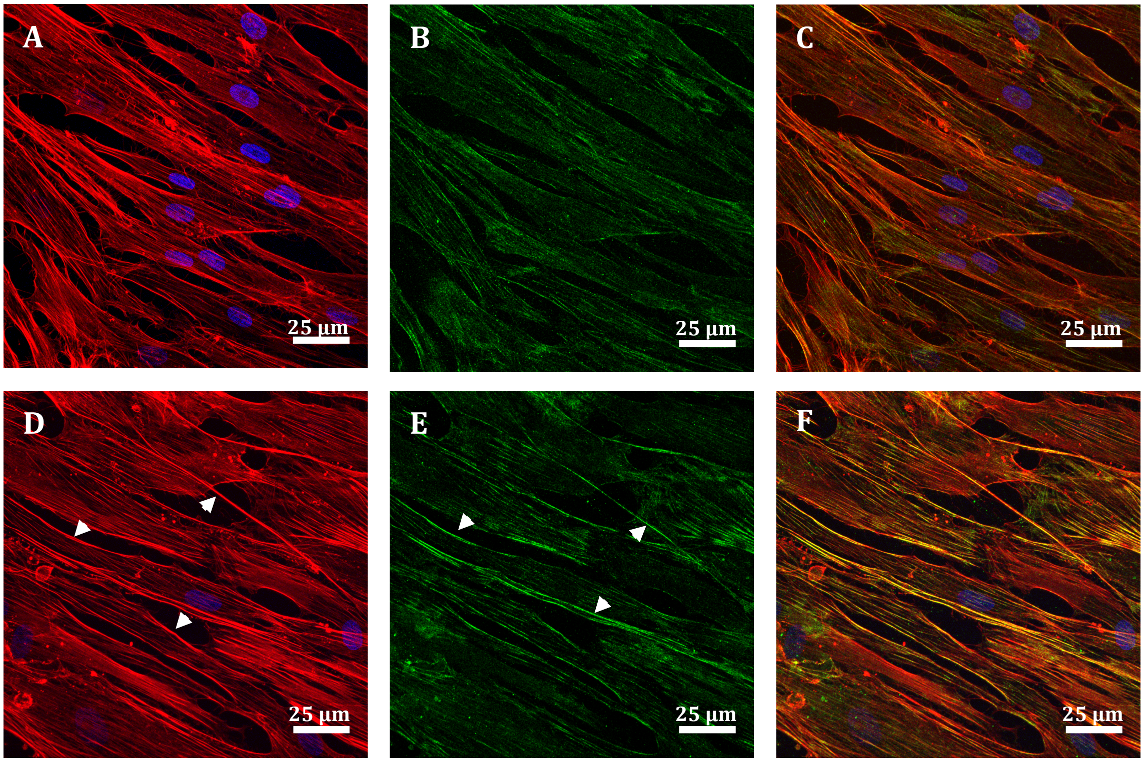

Figure 5.13: Confluent monolayer of control (top row) and 1µM dexamethasone treated (bottom row) SC cells; f-actin (red), phosphorylated myosin (green), nucleus (blue). Cortex and stress fibers are seen in both groups but the cortex is more prominent in treated SC cells (white arrows in D). Also, while p-myosin is present in both groups, it is more concentrated at the cortex of treated cells (white arrows in E). [C] and [F] are overlaid images.

In addition, P-myosin is present at the cortex and along stress fibers in both control and treated groups (5.13B,E) However, there are higher levels of P-myosin at the cortex of treated cells (white arrows in 5.13E) which localizes with the regions of more pronounced cortex as compared to controls.

To further characterize the effect of dexamethasone on the cytoskeleton of SC cells, the distribution of F-actin and vimentin was examined in non-confluent SC cells as shown in Figure 5.14.

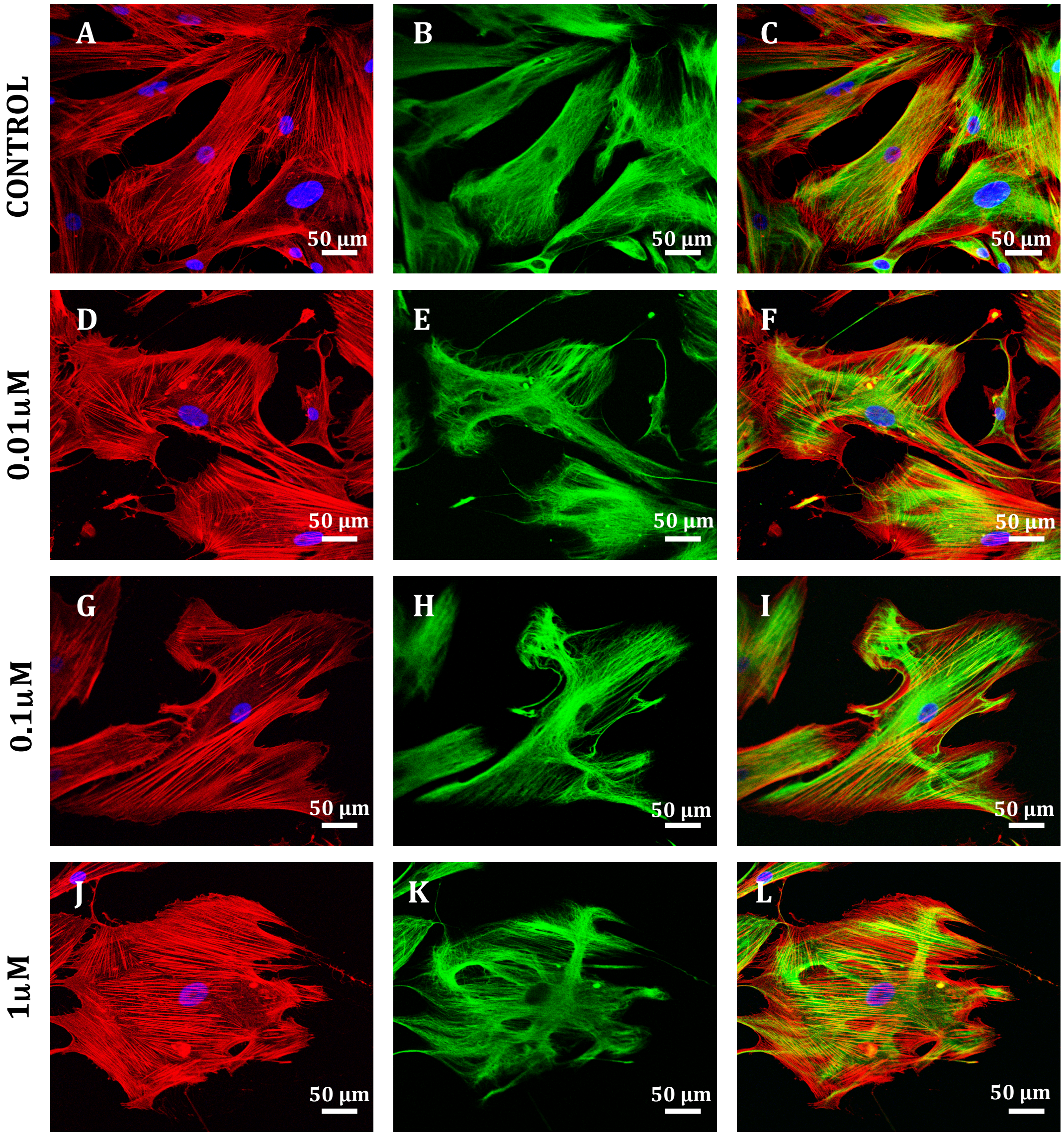

Figure 5.14: Immunofluorescent imaging of control and dexamethasone treated SC cells; f-actin (red: A,D, G, J), vimentin (green: B, E, H,K), combined (C, F, I, L), nucleus (blue). Dexamethasone treated cells showed higher levels of stress fiber formation [D], [G], [J] as compared to control cells [A]. In addition, while vimentin distribution looked uniform in control cells [B], bundling was detected in all treated SC cells [E],[H],[K] regardless of the treatment concentration.

Dexamethasone treatment (especially at 1µM) was associated with elevated stress fiber formation as previously reported for human trabecular meshwork (Clark et al. 2005)(Raghunathan et al. 2015) and alveolar epithelial cells (Puig et al. 2007).

Interestingly, while vimentin distribution was quite uniform in control cells, it had a significantly different distribution in dexamethasone treated groups with the formation of large vimentin filaments aggregates, a phenomenon called bundling (Charrier & Janmey 2015).

B. Western blot

The extracted signal intensities from western blot images for SC cells (see Appendix) are presented in Table 5.4.

Table 5.4: Signal intensity for the probed proteins in western blot

SC 64g							
	Control	Co 0.01	DEX 0.01	Co 0.1	DEX 0.1	Co 1.0	DEX 1.0
Beta actin	49400	32000	33900	32600	34200	42600	47200
SMA	58900	44400	51900	47200	40700	33200	35200
Vimentin	56100	38100	33400	34800	27900	33100	32700
Tubulin	51400	41200	38700	37300	31200	46000	32900
SC 76							
	Control	Co 0.01	DEX 0.01	Co 0.1	DEX 0.1	Co 1.0	DEX 1.0
Beta actin	32800	28500	27900	34500	42700	43100	46000
SMA	45000	45700	39500	45200	50500	46800	47900
Vimentin	31700	36800	38000	33000	44300	39200	49300
Tubulin	32800	31100	36200	38300	46600	41400	38400

As explained in 5.2.7, using a linear model ($I = \alpha + \beta_1[\text{Dex}] + \beta_2[\text{Glaucoma}] + \beta_3[\text{Glaucoma}] * [\text{Dex}] + \beta_4[\text{Etoh}] + \beta_5[\text{Etoh}] * [\text{Glaucoma}]$) for βactin showed a positive correlation between the protein level and ethanol, but not dexamethasone concentration ($p<0.0001$). Furthermore, increases in ethanol concentration also led to a decrease in SMA in SC64g ($p<0.001$) but had no effect on SC76. Dexamethasone treatment had a significant effect on vimentin expression in both SC64g and SC76 (p=0.006). Interestingly, the effect was opposite for normal and glaucoma lines where upon increase in dexamethasone dose, the protein level dropped in SC 64g while it increased in SC76 (p=0.01). Finally, for tubulin, there was no significant effect from dexamethasone or ethanol concentration on either cell line. We should mention the caveat that, these data were only collected once and should be replicated. Overall, the western blots indicate significant changes to the cytoskeleton in treated cells but the majority of the change are due to the ethanol, not the dexamethasone as shown for βactin and SMA. This highlights the importance of proper controls for ethanol when used as the vehicle for experiments. However, we point out that the ethanol concentration was equal in all our AFM, OMTC, and TFM experiments, which rules out the possibility of ethanol effect on those experiments.

C. AFM results

The average Young's modulus for dexamethasone experiment on SC cells using sharp and rounded probes are shown in Figure 5.15. Comparing the averages between control and 1μM groups, there was a significant difference in sharp tip measurements between the control and 1μM groups in all cell strains ($p<0.009$) while measurements using rounded tip did not show a significant difference ($p>0.25$).

Equation 1 in section 5.2.7 ($E = \alpha + \beta_1[\mathrm{Dex}] + \beta_2[\mathrm{Glaucoma}] + \beta_3[\mathrm{Glaucoma}] * [\mathrm{Dex}]$) was then used for the linear regression analysis. Results from the analysis showed a systematic increase in sharp tip measurements in both normal and glaucomatous SC cells upon increase in dexamethasone concentration ($p(\beta_1) < 0.05$). In addition, the analysis indicated a difference in sharp tip measurements between normal and glaucomatous cells ($p(\beta_2) < 0.02$). However, such behavior was absent in rounded probe measurements where there was no difference in stiffness at different concentrations (($p(\beta_1) > 0.8$) and normal and glaucomatous cells responded similarly (($p(\beta_2) > 0.45$). The analysis for both sharp and rounded probe measurements showed a similar effect of dexamethasone on normal and glaucoma cells (($p(\beta_3) > 0.5$).

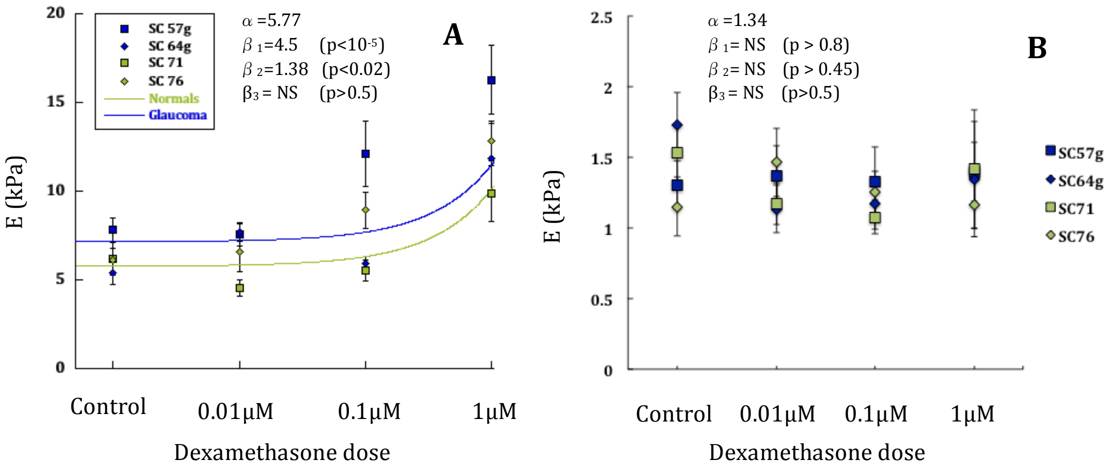

Figure 5.15: Average Young's modulus (mean±SE) measured by sharp [A] and rounded [B] probes for normal (SC 71, SC76) and glaucomatous (SC 57g, SC 64g) cell lines treated with dexamethasone. The green and blue lines correspond to the regression results for cases of statistical significance. For measurements from the sharp probe [A], the analysis shows a significant increase in stiffness by increase in dexamethasone dose (β_1) and indicates a different behavior for glaucoma cells as compared to normals (β_2). However, the effect from dexamethasone treatment on normal and glaucoma cells is the same (β_3). The analysis for the subcortical region showed no effect from dexamethasone treatment. Normal and glaucomatous cells behaved similarly and the dexamethasone effect showed no statistically significant differences between them.

D. OMTC and TFM results

Data from OMTC measurements on SC cells are shown in Figure 5.16. We first compared the averages for 1 µM and control group where the dexamethasone treatment caused a significant drop in modulus in all normal and glaucoma strains ($p<0.05$). Comparison of lower concentrations to controls led to mixed results.

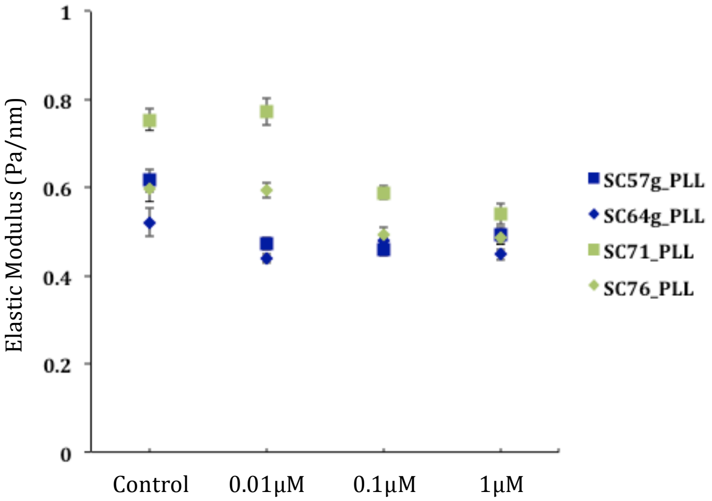

Figure 5.16: Measurements from OMTC (g) (median±MAD) for dexamethasone treated normal and glaucomatous SC cells. Data shows a marginally significant decrease (p=0.084) in cell modulus upon increase in concentration. PLL magnetic beads were used for the measurements.

The regression analysis showed a marginally significant decrease in modulus in both normal and glaucoma cell strains ($p(\beta_1) = 0.084$). Moreover, glaucomatous SC cells showed a lower modulus compared to normal cells ($p(\beta_2) < 0.05$). Like for the AFM, the analysis showed a similar effect of dexamethasone treatment for normal and glaucomatous cells (($p\ (\beta_3) > 0.25$). An interesting observation from OMTC experiment following dexamethasone treatment of the cells is that, overall, measurements from OMTC tended to behave oppositely from AFM sharp tip but were similar to results seen using AFM rounded tips.

Figure 5.17 shows the results from the TFM studies. Like AFM and OMTC, we first compared the averages for 1μm groups to their controls where overall, the traction forces were significantly higher in 1μm groups compared to their controls ($p<0.05$), except for SC 76.This observation is consistent with previously reported results showing that dexamethasone treatment (1 μM) results in elevated traction forces in alveolar epithelial cells (Puig et al. 2007). Data from the regression analysis showed a marginally significant correlation between increased traction and dexamethasone concentration $(p(\beta_1) = 0.092)$. Similar to AFM and OMTC, glaucomatous cells responded differently $(p(\beta_2) = 0.006)$ and dexamethasone had the same effect on cell strains $(p(\beta_3) > 0.95)$.

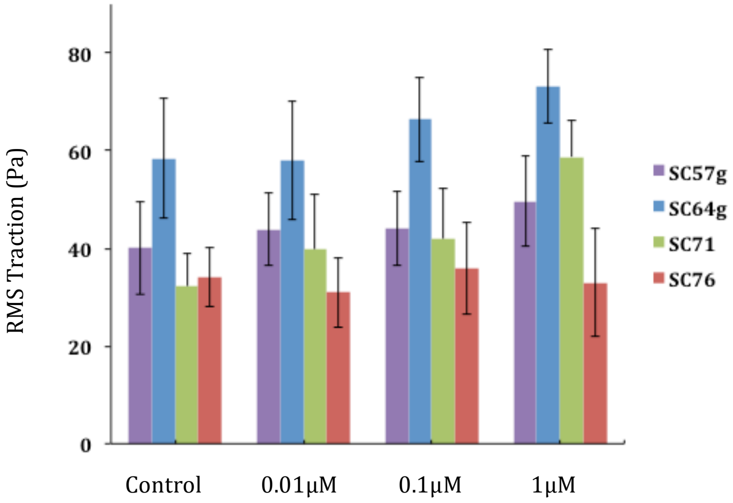

Figure 5.17: Results from TFM (mean±SD) for dexamethasone treated SC cells. Traction forces are significantly higher in 1μM group except for SC 76.

5.4.2 α-actinin and RhoA experiment

A. Imaging results

The F-actin distribution was visualized in control, gfp, α-actinin, and RhoA groups at low [A-D] and higher [E-H] magnifications (Figure 5.18). As expected, prominent cortex along with stress fibers were present in the cytoplasmic region of most of cells in all four groups. Cells in the gfp group (panels B, F) looked to have similar F-actin distribution to control cells (panels A, E). However, in the alpha-actinin group, infected cells showed an altered morphology where they looked rounded as compared to uninfected cells that looked more spread (Figure 5.18 C, G). The altered morphology in α-actinin-infected cells was also different compared to the other three groups.

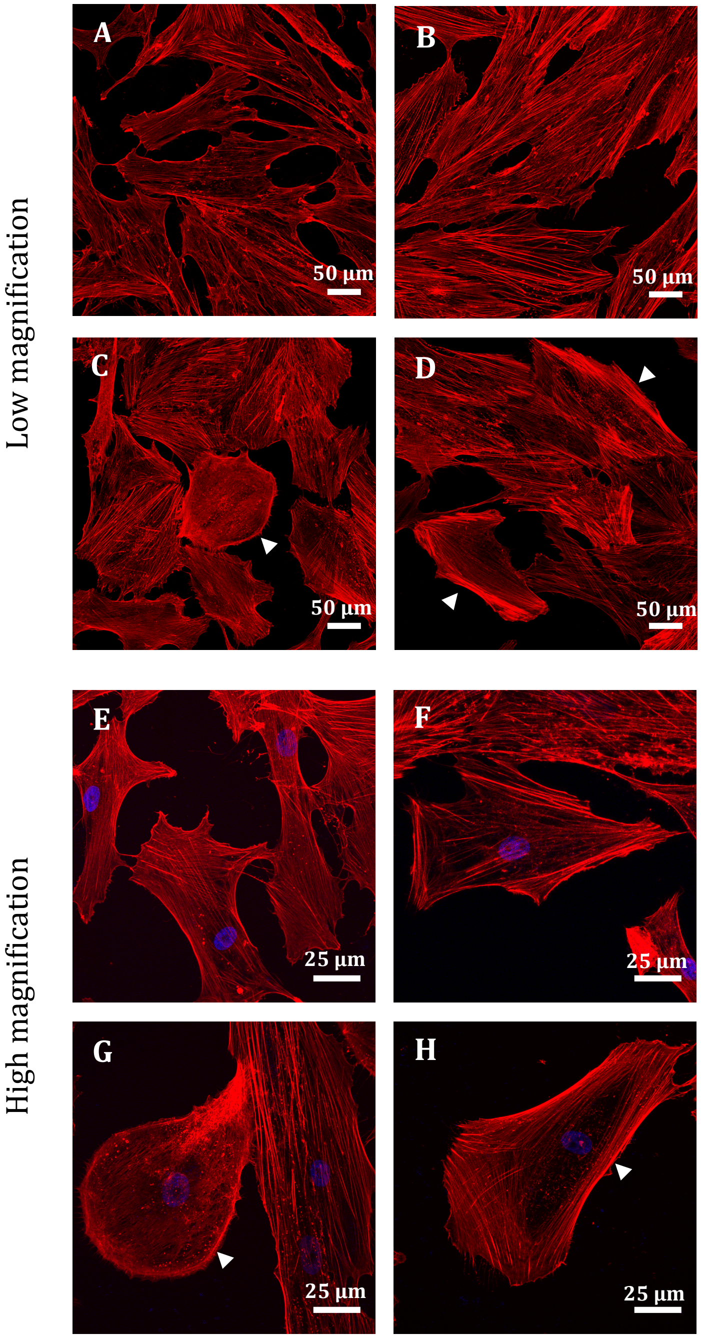

Figure 5.18: Confocal images of control [A, E], gfp [B, F], actinin [C, G], and RhoA [D, H] SC cells at low (20x) and higher (40x) magnifications; f-actin (red), nucleus (blue). Control and gfp groups had similar F-actin distribution and cortex structure [A, B, E, F]. The actinin-infected cells showed an altered morphology and had a relatively thicker cortex (white arrows in C and G). The RhoA images showed the presence of cells with significant accumulation of stress fibers at peripheral regions (white arrows in D) and more prominent cortex (white arrows in H).

Figure 5.19 shows α-actinin-infected cells (at high and low magnifications) with a high green fluorescent intensity juxtaposed to uninfected cells with weak or almost no fluorescent signal. Interestingly, the α-actinin-infected SC cells appear to have a thicker cortex as compared to uninfected cells.

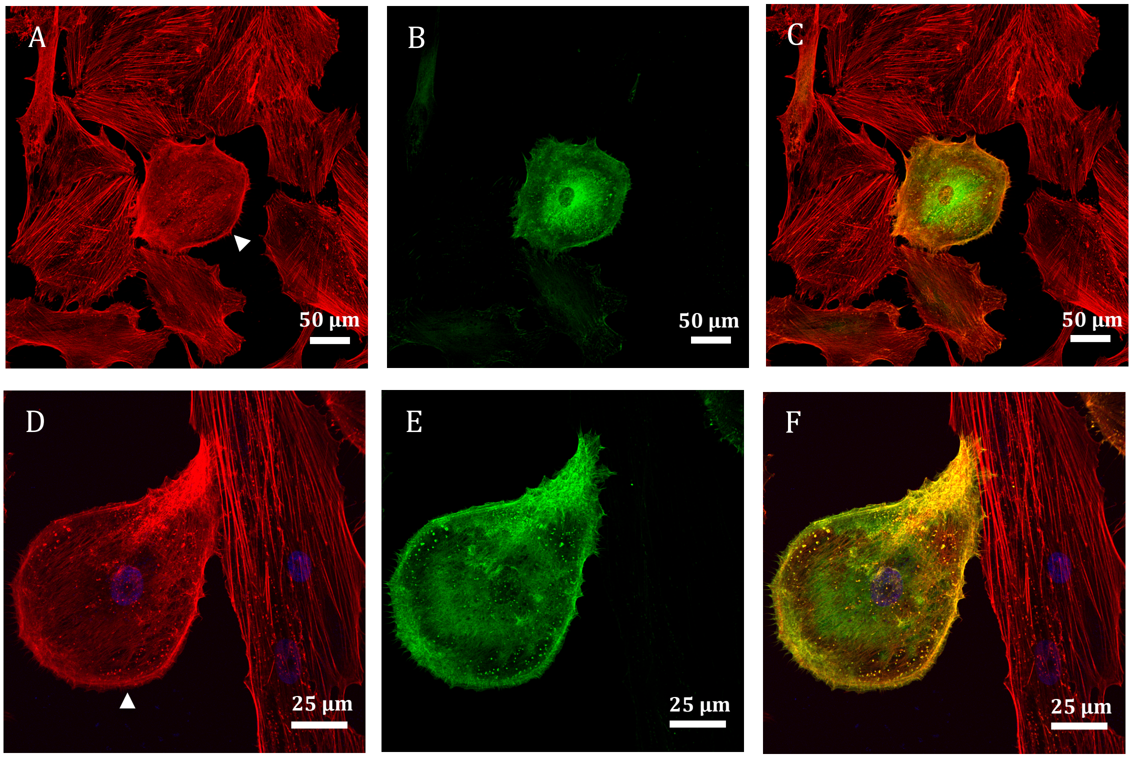

Figure 5.19: Confocal images of SC cells transfected with GFP labeled α-actinin: f-actin (red:A, D), GFP (green: B, C); combined (C, F), nucleus (blue). Only alpha actinin transfected cells showed a green fluorescent signal [B and E]. Infected cells also had altered morphology and increased cortical thickness (white arrows in A and D).

As mentioned earlier, the RhoA infected cells did not have a gfp tag that would enable us locate them. However, imaging results for this group showed the presence of cells with peripheral regions of highly dense F-actin where the cortex was much thicker compared to all other groups (see arrows in Figure 5.18 D, H). We speculate that these cells are could be the RhoA-infected cells. However, an objective approach such as using fluorescent tags for marking RhoA infected cells is needed to examine this question.

B. Western blot

The signal intensities from the western blot image (see Appendix) are shown in Table 5.5. From the table, there is notable difference in protein levels between control and gfp group for both cells strains. This observation emphasizes the potential effects from the ubiquitin promoter vector and gfp tags on protein expression levels and confirms that the gfp group is the appropriate control for the other two infected groups (α–actinin and RhoA).

Table 5.5: Signal intensity for probed proteins in western blot.

SC 57g				
	Control	GFP	Actinin	RhoA
α–Actinin (Intrinsic)	12800	42100	30000	76400
α–Actinin (Induced)	-	-	33700	-
Vimentin	43000	34600	22700	58500
bActin	48100	29400	10400	48100
Tubulin	72800	108000	66800	124000
Total Protein	90100	91000	92100	57100
SC 73				
	Control	GFP	Actinin	RhoA
α–Actinin (Intrinsic)	9570	21400	29100	45400
α–Actinin (Induced)	-	-	65100	-
Vimentin	21100	50600	73600	72700
bActin	50600	74300	57000	65900
Tubulin	58300	121000	128000	174000
Total Protein	126000	70600	82100	58800

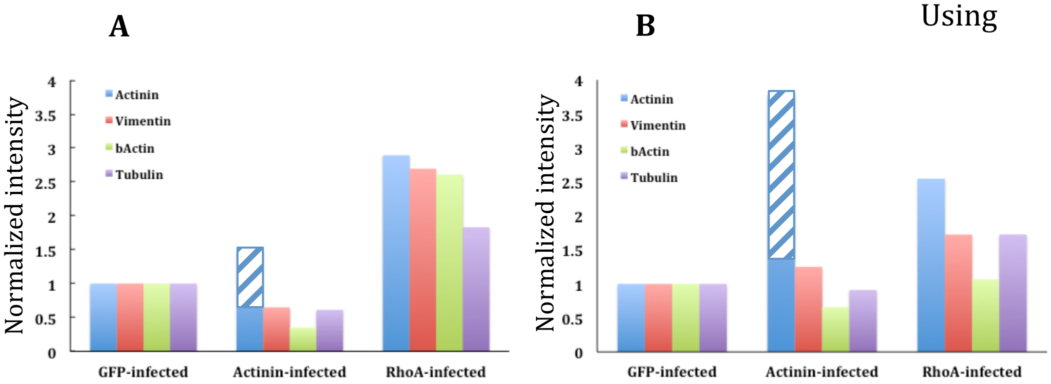

Figure 5.20: Normalized signal intensities from the western blot image for SC57g (A) and SC 73 (B). The overexpression of alpha-actinin has mixed outcomes whereas RhoA overexpression elevates the level of expression for all probed proteins. For the actinin level in the alpha- actinin infected group, the solid blue represents the intrinsic alpha- actinin level and the crosshatched shows the induced alpha- actinin level.

Using this assumption, intensities for protein expression in α-actinin and RhoA infected SC cells were normalized based on the intensity of protein expression in the gfp-infected cells as shown in figure 5.20. Note that two pools of α-actinin are in the α-actinin-infected cells: the induced α-actinin (with GFP-label from the infection) and intrinsic α-actinin (that is inherent to cells of each group and is not GFP labeled). The data shows mixed results for the α-actinin-infected group in the two cell strains. In both there is the expected significant increase in α-actinin; however while SC57g shows a significant decrease (30-65%) in other probed proteins, for SC73, tubulin remains almost the same, while there is a 35% decrease in beta-actin and 10-20% increase in actinin and vimentin. Results are more consistent for RhoA with both cell strains showing a robust increase for all protein levels (6-190%).

C. AFM results

Figure 5.21 shows the averages for all four groups tested with sharp [A] and rounded [B] probes. We compare the gfp and control groups (n=4) to examine the overall effect from gfp and Ubiquitin promoter vector on cell stiffness. The comparison showed no effect on either cortical (p=0.38) or subcortical (p=0.16) stiffness.

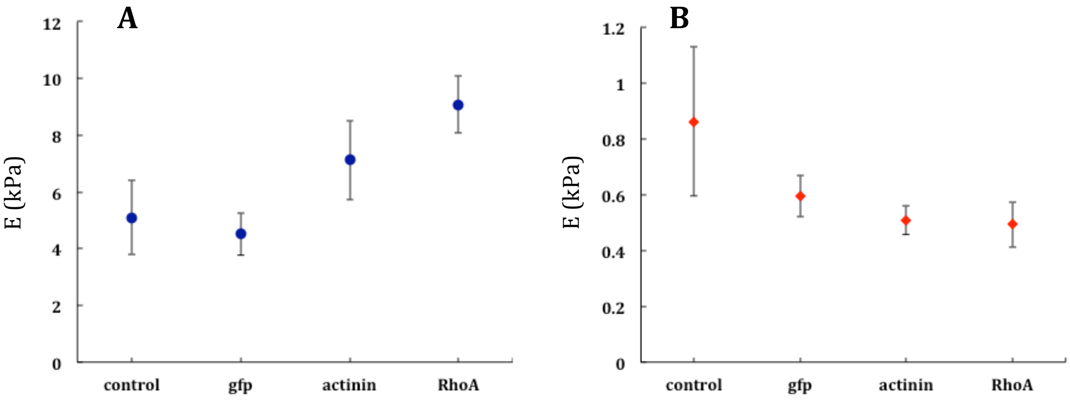

Figure 5.21: Overall average Young's modulus (mean±SE) for sharp [A] and rounded [B] probe for control, gfp, alpha actinin, and RhoA groups. The sharp tip measurements showed significantly increased stiffness in alpha actinin (p=0.026) and RhoA (p=0.009) transfected cells as compared to the gfp. Nonetheless, values from the rounded probe didn't show any difference between these groups (p>0.15).

Measurements using a sharp tip showed significant increase in cell stiffness for the α-actinin (p=0.026) and RhoA (p=0.009) transfected cells as compared to the gfp transfected ones. However, no difference was seen with rounded tips when comparing either alpha=actinin (p=0.32) and RhoA (p=0.16) to the gfp control.

The average Young's modulus for sharp and rounded probes is shown in Figure 5.22 for each cell strain. As measured by the sharp probe, transfection of SC cells with α-

actinin led to a significant increase in the stiffness of SC57g, SC69, and SC71 ($p<0.015$), a marginally significant increase in SC73 ($p=0.1$) and no change in SC76 ($P>0.2$) compared to gfp-transfected cells. In addition, comparison of the values from sharp probe for gfp and RhoA showed a significant increase in the stiffness of SC 57g, SC69, and SC73 ($p<0.02$) and a marginal increase in SC71 ($p<0.09$).

However, measurements from the rounded probe showed no significant difference between the stiffness of gfp and alpha actinin transfected cells except for SC73 ($p<0.006$). The same trend occurred for gfp versus RhoA where only SC69 showed a significant drop ($p=0.048$).

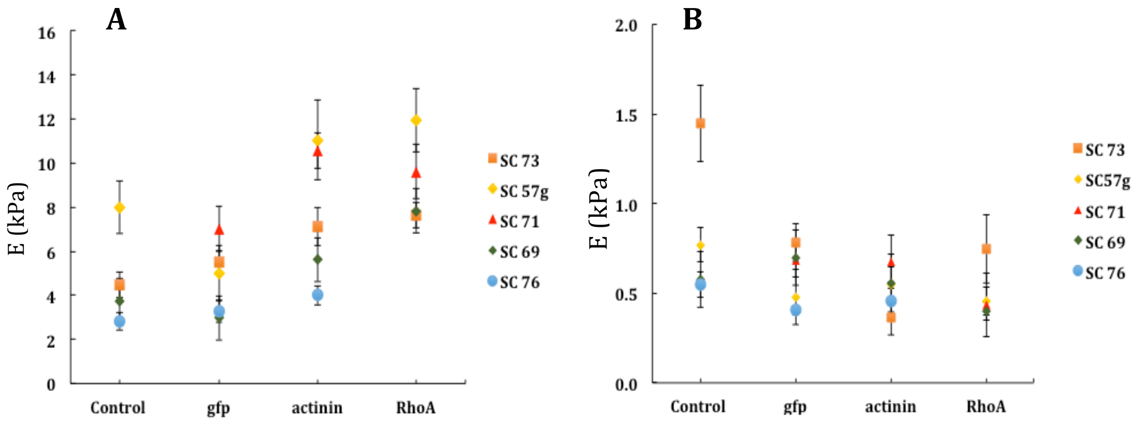

Figure 5.22: Average Young's modulus (mean±SE) for sharp [A] and rounded [B] probes for control, gpf, alpha actinin, and RhoA groups. Overall, measurements from the sharp probe demonstrate an elevated stiffness in alpha actinin and RhoA transfected groups while the rounded probe indicates no change in cell stiffness.

D. OMTC and TFM results

Data from OMTC are shown in Figure 5.23. Comparison between the control and gfp transfected cells showed a small but significant drop in cell modulus caused by gfp (p<0.001), in contrast to results from AFM sharp and rounded probes. Also, when compared to gfp, the modulus in actinin and RhoA show a marginally significant (p=0.09) and significant (p=0.02) drop, respectively. Again, OMTC measurements for actinin and RhoA tend to move in the opposite direction of AFM sharp probes, consistent with the observation from the dexamethasone experiment, but similar to the rounded tip results.

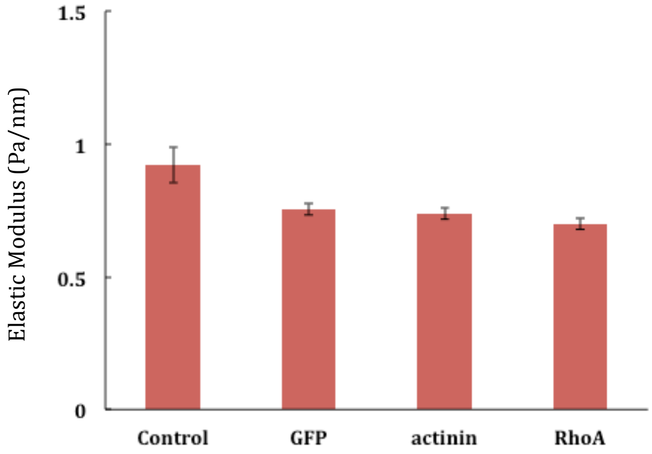

Figure 5.23: Average elastic modulus (g) from OMTC (median±MAD) for control, gfp, actinin, and RhoA transfected SC cells (SC 71). The modulus is lower in actinin (p=0.09) and RhoA (p=0.02) infected SC cells as compared to gfp.

Figure 5.24 shows data from TFM. The plot shows no difference in traction forces between control and gfp transfected cells (p=0.35). Also, the overexpression of alpha-actinin does not affect SC cell contractility (p=0.75). Finally, RhoA transfected SC cells showed a significant increase (p<0.05) in traction forces as compared to gfp cells. This observation is consistent with previously reported results for epithelial MDCK cells (Reffay et al. 2014).

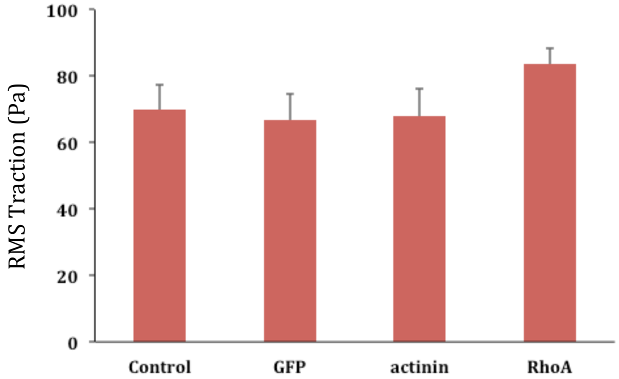

Figure 5.24: Results from TFM measurements (mean+SD) for control, gfp, actinin, and RhoA transfected SC cells (SC 71). Traction forces were significantly higher in RhoA transfected cells ($p<0.05$) as compared to other groups.

5.4.3 MEFs experiment

The primary purpose from MEFs experiments was to examine the role of vimentin in cell mechanics. Imaging studies have previously shown an intact vimentin meshwork in WT MEFs as compared to a completely eliminated vimentin meshwork in KOs (Guo et al. 2013). In addition, western blot analysis has confirmed the same expression level for the other two cytoskeleton proteins, actin and tubulin, in WT and KO MEFs (Guo et al. 2013). Based on these results, we did not conduct imaging or western blot analysis for these cells and moved directly to mechanical characterization.

A. AFM results

Two separate AFM experiment were done to characterize the stiffness of the MEFs. For the first experiment, AFM sharp probe led to stiffness values of 6.3±1.85 kPa and 3.27±0.61 kPa for WT and KO cells, respectively ($p=0.022$) while values from the second experiment were 9.27±2.42 kPa and 4.58±0.78 kPa for WT and KO (p=0.012) respectively. The AFM rounded probe gave an average stiffness of 1.18±0.16 kPa for WTs and 0.87±0.08 kPa for KOs (p=0.083) in the first experiment and 0.74±0.11 kPa for WTs and 0.47±0.08 kPa for KOs (p=0.064) in the second experiment, in each case showing a marginally significant decrease. Pooling the two experiments gave similar results, but the result for the rounded tips was no longer marginally significant (p_{sharp}=0.039, $P_{rounded}$ =0.36).

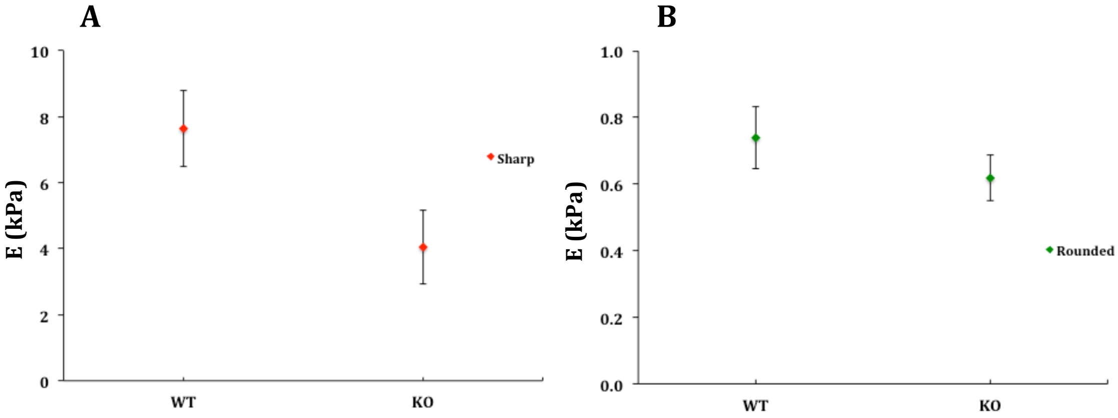

Figure 5.25: Average Young's Modulus (mean±SE) from the sharp (A) and rounded (B) probes in wild type and vimentin knock out MEFs. Sharp tip measurements showed a significantly lower stiffness for KO cells whereas values from rounded probe had no significant change.

B. OMTC and TFM results

Results from the first OMTC experiment using PLL coated beads are shown in Figure 5.26. Surprisingly, in both presence and absence of calf serum, confluent KO cells had significantly higher modulus as compared to the WTs (p<0.0001).

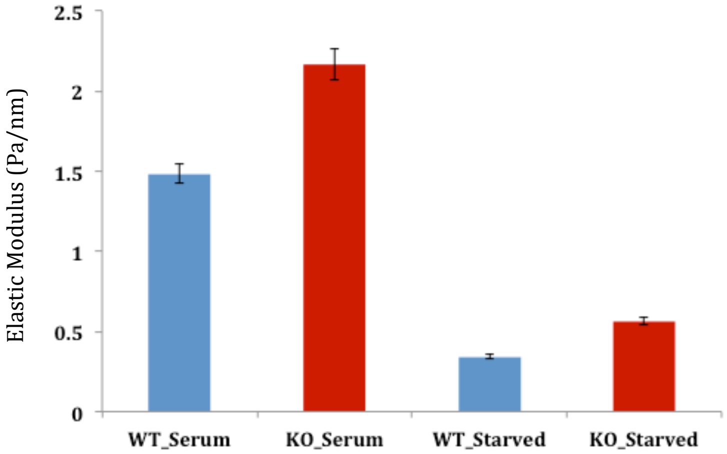

Figure 5.26: Average elastic modulus (g) from OMTC (median±MAD) for confluent wild type (WT) and knock out (KO) MEFs in serum free (starved) and serum containing (serum) media. KO cells had higher modulus compared to WTs in both groups ($p<0.0001$). PLL coated beads were used for the measurements.

This observation becomes more puzzling when comparing it to data from AFM where both sharp and rounded probes indicated a significant and slight drop in stiffness of KO cells. This was also in contrast to what Guo et al. (Guo et al. 2013) reported where they saw no difference between WTs and KOs when used OMTC with PLL beads to probe single WT and vimentin KO MEFs (Guo et al. 2013). It is noteworthy that Guo et al. received these cells from the same laboratory as did we (Dr. Robert Goldman), which rules out the tentative variability from using different cell sources.

We sought to fully replicate the experimental condition in Guo's work as described in 5.2.6 and conducted an OMTC experiment using PLL beads on sparsely seeded MEFs as opposed to the first OMTC experiment that was done on confluent cells. The outcome is shown in Figure 5.27 where single KO cells again had significantly higher moduli compared to wild types ($p<0.02$). While this observation is the same as we found in confluent cells, it is still in contrast to what was reported by Guo et al (Guo et al. 2013). However, it is notable that even though Guo et al did not find a significant difference in the stiffness of WT and KO cells using OMTC, the KO stiffness was greater than WTs at all tested frequencies below 10Hz (including our tested frequency, 0.78Hz).

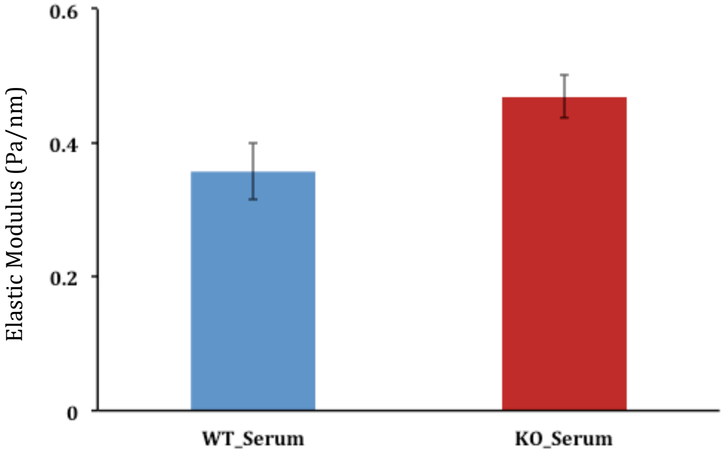

Figure 5.27: Average elastic modulus (g) from OMTC (median±MAD) for single wild type (WT) and knock out (KO) MEFs in serum containing media. Single KO cells had higher modulus compared to WTs (p<0.02), which was the same behavior in confluent cells.

We finally sought to see if using RGD coated beads could lead to different observations since the different bead attachments are known to influence OMTC measurements (Coughlin et al. 2006). Figure 5.28 shows the results for the third OMTC experiment where both PLL and RGD coated beads were used to probe confluent WT and KO cells.

The PLL experiment with serum showed no significant difference between WTs and KOs (p=0.8), consistent with Guo et al. However the serum-starved KOs were stiffer than WTs ($p<0.001$), the same observation as in the first experiment. Surprisingly, data from RGD coated beads showed an opposite pattern where WTs were significantly stiffer than KOs in both serum ($p<0.05$) and serum free groups ($p<0.001$). This observation is in contrast to our PLL data and also results reported by Guo et al. The discrepancy between PLL and RGD coated beads has been previously mentioned in the literature (Coughlin et al. 2006) and we will discuss these observations further in the discussion section.

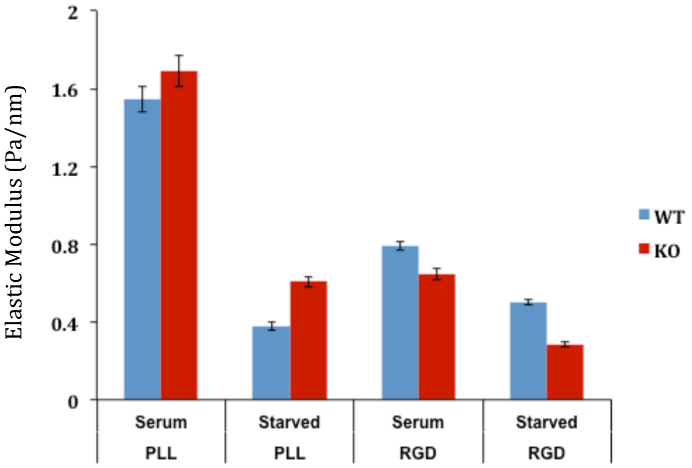

Figure 5.28: Average elastic modulus (g) from OMTC (median±MAD) for confluent wild type (WT) and knock out (KO) MEFs in serum free (starved) and serum containing (serum) media. Both PLL and RGD magnetic beads were used for the measurements. For PLL experiment, KOs had significantly higher modulus in the absence of serum ($p<0.0001$) while the behavior was opposite in the RGD experiments in both presence and absence of serum ($p<0.05$).

Results from the first TFM experiment ($E_{substrate}=1.8kPa$) on the MEFs are shown in Figure 5.29 that shows that WT cells have higher traction forces compared to the KOs in both serum and serum-starved groups. The difference in these forces were statistically significant for high-density (10000/well) seeded cells ($p<0.03$) while at low density seeding (1000/well), it was significant for serum free group ($p<0.05$) and marginally significant in presence of serum ($p<0.065$).

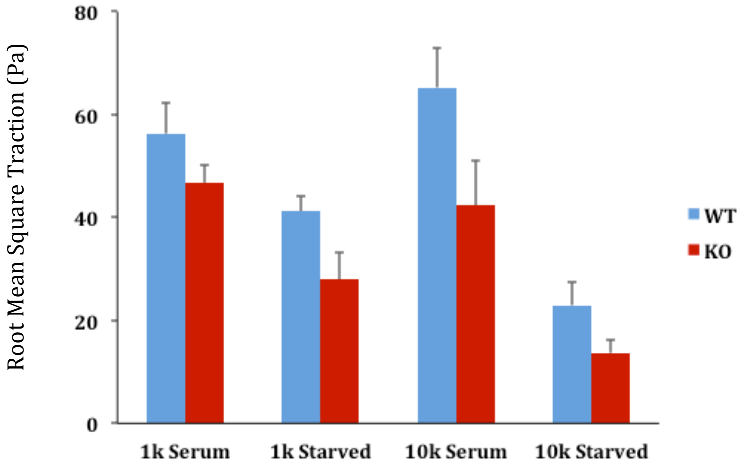

Figure 5.29: Results from TFM measurements for low (1000/well) and high (10000/well) seeding density of MEFs in serum free and serum containing media. Overall, traction forces were significantly higher in wild type cells as compared to knockouts.

Figure 5.30 shows the results for the second TFM experiment ($E_{substrate}$= 8kPa) where WTs again show higher contraction forces in both presence ($p<0.001$) and absence of the serum ($p<0.01$). The results also indicate that media replacement didn't affect cell behavior in either serum containing ($p<0.001$) or deprived ($p<0.05$) groups.

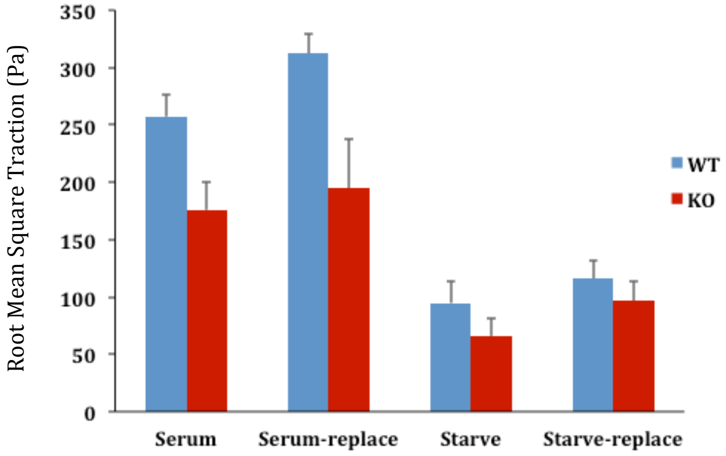

Figure 5.30: Results from TFM measurements for high density (10000/well) seeded MEFs in serum free and serum containing media. Traction forces were significantly higher ($p<0.05$) in wild type cells as compared to knockouts in presence and absence of serum.

5.5 Discussion

In the studies described in this chapter, we used experimental analysis and numerical simulations to show the role of cytoskeleton in regulating the mechanics in SC cells and MEFs. Our results for SC cells show that dexamethasone, α-actinin and RhoA all altered the cytoskeleton and changed the mechanical behavior in these cells. We also found that WT and vimentin KO MEFs have significantly different mechanical properties. A summary of our functional measurements is shown in Table 5.6.

Table 5.6: Summary of Functional Measurements

Experiment	AFM		OMTC		TFM
	Sharp	Rounded (10μm)	PLL	RGD	
Dexamethasone (SC cells)	↑	↔	↓	NM	↑
Actinin (SC cells)	↑	↔	↔	NM	↔
RhoA (SC cells)	↑	↔	↓	NM	↑
Vimentin KO MEFs	↓	↔	↑	↓	↓

“↑“ : significant increase, “↓“: significant decrease
“↔ ”: No change or marginally significant, “NM”: not measured

The measurements using sharp AFM tips on SC cells indicated that each of the cytoskeletally-active agents we used cause the cell cortex to become stiffer, a result consistent with our imaging studies. TFM largely tracked the results from AFM sharp tips. In contrast, measurements with a round AFM tip showed little change of cell stiffness with any of these agents, while OMTC measurements showed either a small decrease or no change; qualitatively, OMTC measurements showed no agreement with the AFM sharp tip measurements, but were somewhat similar to those measure with AFM round tips. These findings were not consistent with literature suggestions (Guo et al. 2013) that OMTC largely characterizes the behavior of the cell cortex.

Our FEM studies also showed that OMTC measurements characterize an aggregate measurement of cell stiffness as opposed to being dominated by the cortex. Our modeling studies also suggested that embedding depth could be a confounding variable when using OMTC to compare the stiffness of different cell types. In this section, we discuss the basis of these conclusions.

5.5.1 Interpreting measurements from AFM and OMTC

The FEM results showed that measurements using AFM rounded probes are influenced by both tip radius and cortex stiffness. Overall, smaller AFM probes are more sensitive to the cortex stiffness and their associated strain field is mostly confined to the cortex whereas larger probes demonstrate lower sensitivity to cortical stiffness and have strain fields that spread deeper into the cytoplasm (Figures 5.5-8). This is consistent with our previous findings for the AFM sharp and large rounded probes that showed very high and lower sensitivity to cortical stiffness, respectively (Vargas-Pinto et al. 2013). The imaging studies along with the AFM data for dexamethasone-treated, actinin-infected, and RhoA-infected cells confirmed our conclusions from the FEM for AFM analysis where changes in cortical structure influenced measurements from AFM sharp probe while rounded probes showed little sensitivity.

Guo et al. (2013) previously used optical tweezers to probe the mechanics of deeper cytoplasmic regions in MEFs where they found a 50% reduction in cytoplasmic modulus in vimentin KO cells (Guo et al. 2013). However, as shown in Figure 5.25, the AFM rounded probes found only small differences in modulus between WT and KO cells. This observation emphasizes the fact that while measurements from larger AFM rounded probes are less influenced by cell cortex, they likely do not represent the mechanics of deeper cytoplasm, but instead subcortical regions that are immediately underneath the cortex.

Modeling results for OMTC suggested that measurements using this technique give strain fields and measurements similar to larger AFM rounded probes (Figure 5.9) but are somewhat more affected by cortical stiffness (Figure 5.12B); however, our modeling results suggest that OMTC measurements are not strongly affected by cortical stiffness to the extent that sharp tips and small rounded tips are (Figure 5.12A). The effects of dexamethasone, α-actinin and RhoA that all affect cortical stiffness would appear to confirm that OMTC is not strongly affected by cortical stiffness.

The results of AFM and OMTC measurements (with PLL-coated beads) are in sharp contrast to one another as the latter measurements suggest that vimentin KO MEFs have a higher stiffness that WT cells; it is hard to imagine how KO cells could be stiffer than WT cells, since vimentin is thought to play a structural role in the cell (Mendez et al. 2014). We suggest an alternate explanation. If bead embedding depth is higher in KO MEFs as opposed to WT MEFs, then this could increase the apparent cell stiffness of the KO cells; this could be true for MEFs with or without a prominent cortex (Figure 5.10); we note that we do not know the extent to which MEFs do or do not have a prominent cortex. We suggests that OMTC is a useful technique for measuring changes in cell stiffness cause by drugs, since the bead is embedded into the cell before the drug is administered and presumably this is not significantly changed by the drug. However, comparing the stiffness of different cells types may require measurement of bead embedding depth since there is no reason to expect these are comparable in different cell types. We are currently exploring such measurements in KO and WT MEFs.

Finally, we also note in Table 5.6 that the outcome from OMTC measurement is opposite for PLL and RGD coated beads when probing MEFs. This observation has been previously reported by other researchers (Coughlin et al. 2006). PLL-coated beads bind to cell cortex electrostatically and are just associated with the cortex while RGD coated beads bind to integrins at cell surface and thereby are connected to and probe the deep cell cytoskeleton. Because of this, binding of RGD activates the cell, which can change its mechanical characteristics (Price et al. 1998). Thus, PLL-coated beads are thought to be better probes of cell mechanics (Na et al. 2008).

5.5.2 Effect of dexamethasone on mechanics of SC cells

Ocular use of dexamethasone can cause ocular hypertension and steroid-induced glaucoma in some individuals (Clark et al. 1995) (Jones & Rhee 2006). Dexamethasone treatment has also been found to increase cell stiffness in several studies (Lam et al., 2007; Puig et al., 2007; Raghunathan et al. 2015). In chapter 1, we hypothesized that the stiffness of SC cells increases upon dexamethasone treatment and through our AFM studies, we found that dexamethasone significantly increases cell stiffness as measured by sharp tip. However, results from the rounded probe showed no change in cell modulus, suggesting that cell cortex is probably the primary site of action for dexamethasone. OMTC measurements on SC cells treated with dexamethasone showed a marginally significant drop in cell modulus when examined by a regression model and a significant drop when control and 1μm groups were compared (Figure 5.16). Imaging results (Figure 5.13) showed increased F-actin and phosphorylated myosin at the cortical level, potentially increasing cortical stiffness and tension. This could be due to recruitment of F-actin from the cytoplasmic area to the cortical region, a behavior that could potentially explain the small decrease in subcortical stiffness as measured by rounded probe and also elevated traction forces as measured by TFM. Overall, dexamethasone treatment significantly changed the cytoskeleton and elevated the stiffness in SC cells. This is consistent with our hypothesis for steroid induced glaucoma where we proposed the increased intraocular pressure (IOP) could be due to elevated stiffness of these cells, which is capable of impeding pore formation (Overby et al. 2014).

5.5.3 Effect of alpha-actinin and RhoA overexpression on mechanics of SC cell

Our results show that the effect of induction of α-actinin and RhoA on SC cell mechanics expression is similar to that of dexamethasone. Results from use of the sharp tip indicate a significant increase in cortical stiffness upon overexpression of these proteins. This is in agreement with imaging results in Figure 5.18, which indicate elevation in cortical thickness for both groups. On the other hand, like dexamethasone, subcortical stiffness measurements were either unchanged or slightly decrease in α-actinin-infected and RhoA-infected cells.

OMTC measurements showed a marginally significant drop in stiffness in α-actinin-infected group and significant reduce in the modulus of RhoA-infected cells. The TFM data showed no change in traction forces for the actinin-infected cells. However, RhoA-infected SC cells showed significantly higher traction forces as compared to the gfp-infected ones. One incentive for our studies was to examine the possibly of using viral vectors to alter the stiffness of SC cells for possible clinical use. Results from our studies confirmed that we could modulate the mechanics of SC cells.

5.5.4 The role of vimentin in cell mechanics

As described in 5.5.1, Guo et al. previously used optical tweezers and showed a significant drop in cytoplasmic stiffness in vimentin KO MEFs (Guo et al. 2013). They also probed cells with OMTC using PLL beads where they found no difference between WT and KO cells and concluded that vimentin did not play a major role in determining cell cortex stiffness. However, when we replicated the same experimental condition as Guo et al. (see 5.2.6) and performed OMTC using PLL coated beads on WT and KO MEFs, we found that KO cells were significantly stiffer than WTs. A closer examination of the data from Guo et al. revealed that KO cells were also slightly stiffer than WTs in their studies, although this difference was not statistically significant. Our measurements using AFM sharp probes indicated instead a significant drop in cortical stiffness in KO cells, as compared to the WTs. Moreover, data from AFM sharp probe highlights vimentin's role in cortical mechanics; in particular, loss of vimentin causes a decrease in cortical stiffness. This is a new finding and in disagreement with Gao et al. (2013) who suggest that vimentin is not involved in determining cortical stiffness. Cell migration is known to depend on generation of traction forces (Solon et al. 2007) and vimentin KO cells are shown to lose their migration capability (Mendez et al. 2010), which is consistent with our AFM sharp tip and TFM data. Future studies should examine the distribution of vimentin in the cortical region of KO and WT MEFs.

5.6 Summary and Recommendations

In this chapter, we discussed the role of cytoskeleton in mechanics of SC cells and MEFs. Through our dexamethasone studies, we found that the cortical stiffness and traction forces are elevated in SC cells upon dexamethasone treatment; these mechanical changes are concurrent with significant changes in F-actin and vimentin distribution. The increased stiffness and traction in SC cells is consistent with reported results for other dexamethasone treated cell types (Puig et al. 2007). Those are also consistent with our hypothesis for steroid induced glaucoma where we speculated increased IOP might be a result of increased stiffness in SC cells that can potentially impede pore formation. Future studies may focus on using technique developed in Chapter 3 to characterize the mechanics of SC cells and TMs of steroid induced glaucomatous eyes *in-situ*.

Data from RhoA- and a-actinin-infect SC cells emphasized how changing F-actin cytoskeleton can influence the mechanics in SC cells, and like dexamethasone, have a strong effect on the cell cortex. Our data confirmed that viral vectors can promote RhoA and actinin expression in SC cells, which in turn resulted in higher cortex stiffness and traction forces in these cells.

Our studies on MEFs revealed a significant role for vimentin in regulating cortex stiffness. This was in contrast to the conclusion from Guo et al. (Guo et al. 2013) who used OMTC to examine cortex mechanics in these cells and concluded vimentin had no such effect. As concerned with SC cells and glaucoma, the significance in understanding how vimentin can modulate cell mechanics is that we have previously demonstrated an elevated subcortical stiffness in glaucomatous SC cells (Overby et al. 2014) and our western blots in this study show that vimentin is abundantly expressed in these cells. We also confirmed in this study that changes in SC cell cytoskeleton can significantly alter their mechanics. These observations promote the notion that vimentin could potentially contribute to elevated subcortical stiffness of glaucomatous SC cells. This is a topic for future direction in studying the mechanobiology of SC cells in glaucoma.

To address the differences between the AFM and OMTC measurements, we created a finite element model to investigate effects of cortex stiffness and probe size/embedding depth on measurements from these two methods. The modeling results indicated that OMTC behaves similar to rounded AFM probes and is only moderately influenced by cortical stiffness, as opposed to AFM sharp tips which are strong affected. The model also showed notable effect from bead embedding depth on OMTC measurements, which can potentially explain the differences between the behavior of OMTC and AFM rounded probes.

Chapter 6: Conclusions

An elevated intraocular pressure that is caused by increased aqueous humor outflow resistance frequently characterizes primary open angle glaucoma. The general consensus is that the bulk of resistance to the outflow in the normal eye occurs in the immediate vicinity of the inner wall endothelium of the Schlemm’s canal (SC) and this is also where the elevated flow resistance characteristic of glaucoma is generated.

Aqueous humor enters Schlemm's canal by passing through pores in the endothelial lining of the canal. These pores form as a result of large deformations in these SC cells, and their density is significantly reduced in in the inner wall of glaucomatous eyes. Our hypothesis has been that increased stiffness in SC cells leads to reduced cellular deformation and thereby reduced pore formation leading to increased outflow resistance and elevated intraocular pressure. We have previously shown a correlation between the stiffness of SC cells and reduced pore formation in perfused SC monolayers *in-vitro* and the primary purpose of this thesis was to expand these observations to examining SC cell mechanical properties *in-situ*.

Cells adjust their properties, and in particular their mechanics, to the stiffness of their substrates. Physiologically relevant studies for SC cell mechanics require that these cells be characterized in the natural environment, and on their physiological substrate. As a result, the main focus of this thesis was to establish a technique that allowed for simultaneous characterization of SC cell and their substrate mechanics *in-situ.*

Sections of inner wall of Schlemms' canal were extracted from postmortem normal and glaucoma human eyes and stained to locate SC cell on tissue surface. Atomic force microscope was used to characterize the stiffness of cells and their underling matrix. Results from experiments on both normal and glaucoma samples could be described by five distinct patterns, P1-P5, for the effective modulus as a function of indentations. The modulus in the patterns showed large variability with some values typical of those measured in cells, and other higher, potentially characteristic of the underlying tissue.

To further understand these patterns, we developed a finite element model (FEM) and examined the effect of the stiffness of cortex and of the underlying tissue (the basement membrane, juxtacanalicular connective tissue and the rest of the rest of the trabecular meshwork) on the AFM measurements. The FEM was able to reproduce qualitatively and quantitatively the patterns P1 (essentially that of an SC cell) and perhaps that of P5 (most effected by the substrate), but not P2-P4. Our model gave us insights into interpretation of the experimental data. Together, the numerical simulations and experimental data demonstrated that measurement with a low modulus represented SC cell stiffness and while higher measurements reflected the modulus of the substrate of these cells.

Consistent with our previous *in-vitro* observations (Overby et al. 2014), the *in-situ* results showed a significantly higher modulus in SC cells from the single glaucomatous eye we examined, as compared to the normals. In addition, the SC cell substrate in the glaucomatous eye was stiffer than that of the normal samples. This is also consistent with previously reported results for TM stiffness in normal and glaucomatous eyes (Last et al. 2011) and indicated the possible interplay between SC cell and TM mechanics (Russell & Johnson 2012). Our conclusions for glaucoma experiment were on only one glaucomatous globe and future studies are required to validate our conclusion.

The second aspect of the studies described in this thesis was our examination of the effect of dexamethasone on the cytoskeleton and stiffness of SC cells, and related studies about the interpretation of measurements of cytoskeletal mechanics. We proposed that the increased outflow resistance in steroid induced glaucoma might be due to increased stiffness of SC cells that can potentially impede pore formation and reduce pore density. Imaging along with AFM, TFM, and OMTC studies were used to characterize the cytoskeleton and cell mechanics in control and dexamethasone-treated SC cells. Imaging studies revealed a major change in the distribution of F-actin and vimentin in dexamethasone-treated SC cells as compared to their controls, and suggested significant changes to the cortical regions of the cells. Measurements from AFM sharp probe showed that dexamethasone treatment significantly elevated the cortical stiffness in SC cells whereas the rounded probe showed little change in their subcortical stiffness. TFM results demonstrated increased traction forces in dexamethasone-treated SC cells. In contrast, OMTC showed a marginally significant drop in the stiffness of treated cells. Overall our dexamethasone studies confirmed our hypothesis of increased stiffness of SC cells in steroid treated cells. This became an incentive to further investigate how changing the cytoskeleton in SC cells can modulate their mechanics.

To do so, we used the viral vectors developed by Dr.Stamer to induce the expression of RhoA and α-actinin in SC cells and performed the same experimental procedures as we did in dexamethasone studies. Imaging studies indicated a significant change in the F-actin cytoskeleton in RhoA and α-actinin infected SC cells, similar to those seen with dexamethasone, and emphasizing cortical changes. Results from these experiments showed that cortex stiffness was significantly higher in both RhoA and α-actinin infected SC cells, but the subcortical stiffness show little or no change. TFM showed increased traction forces in RhoA-infected, but not the α-actinin-infected group. Similar to dexamethasone-treated SC cells, OMTC showed a lower modulus for RhoA and α-actinin infected SC cells.

We next investigated the role of vimentin in cell mechanics. Our incentives for this study were two-fold. First, we have previously demonstrated an elevated subcortical stiffness in glaucomatous SC cells (Overby et al. 2014) and vimentin is abundantly expressed in these cells; thus it could potentially play a role in altered mechanics of glaucomatous SC cells. Secondly, we aimed to examine the general consensus that suggests OMTC measures the cortex stiffness (Guo et al. 2013)(Coughlin et al. 2006) as data from previous two experiments suggested that notion may not be true. Guo et al. used OMTC to characterize the stiffness of wild type (WT) and vimentin knock out (KO) mouse embryonic fibroblasts (MEFs) and found no significant difference concluding that vimentin plays no role in regulating cell cortex mechanics. Following the same experimental approach as our studies with dexamethasone, alpha-actinin and RhoA, we found that vimentin plays a significant role in cell cortex mechanics, in disagreement with the results of Guo et al (2013). Surprisingly, OMTC measurements suggested that KO cells were stiffer than WTs, which is unlikely, as vimentin has been shown to contribute significantly to cell mechanics.

In all of the experiments described in chapter 5, we saw a difference between the AFM sharp tip results (characterizing cortical stiffness) and OMTC data; there were also some difference between the AMF round tip results (characterizing subcortical stiffness) but these were not as dramatic, except in the case of the MEFs, where OMTC gave this particularly usual result of KOs having higher stiffness than WTs.

We explored this issue in some depth using a FEM to examine the effect of cortex stiffness, probe size and embedding depth on AFM and OMTC measurements. The numerical simulations suggested a significant effect from cortex stiffness on both AFM and OMTC measurements. The model confirmed that AFM sharp probes and rounded probes of small radius are more influenced by the cortex stiffness and thus characterize the stiffness of that region as opposed the larger rounded probes that primarily probe the subcortical stiffness. More importantly, the results suggested that OMTC behaves similar to AFM rounded probes and is more influenced by the subcortical mechanics of the cell and less so by the cortex. This is in contrast to the general consensus and conclusion from Guo et al. that OMTC characterizes the cortex. Finally, our model suggested that OMTC measurements are also influenced by bead embedding depth and that this might be the reason for the discrepancy between the OMTC and AFM data in our experimental results. Hence, it is recommended that future studies using OMTC behavior to compare the stiffness of different cell types need to measure bead embedding depth at the same time, particularly if those studies are done on different cell type.

References

A-Hassan, E. et al., 1998. Relative Microelastic Mapping of Living Cells by Atomic Force Microscopy. *Biophysical journal*, 74(3), pp.1564–78.

Allingham, R. & Kater, A. de, 1992. The relationship between pore density and outflow facility in human eyes. *... ophthalmology & visual ...*, 33(5), pp.1661–9.

Bill, A. & Svedberg, B., 1972. Structure of the trabecular meshwork and the canal of Schlemm. *Trans Am Acad Ophthalmol Otolaryngol*, 70(5), p.777.

Butler, J.P. et al., 2002. Traction fields, moments, and strain energy that cells exert on their surroundings. *American Journal of Physiology Cell Physiology*, 282(3), pp.C595–C605.

Carl, P. & Schillers, H., 2008. Elasticity measurement of living cells with an atomic force microscope: data acquisition and processing. *Pflügers Archiv : European journal of physiology*, 457(2), pp.551–9.

Charras, G.T. et al., 2006. Reassembly of contractile actin cortex in cell blebs. *The Journal of cell biology*, 175(3), pp.477–490.

Charrier, E.E. & Janmey, P.A., 2015. Mechanical Properties of Intermediate Filament Proteins. In *Methods in Enzymology*.

Clark, A.F. et al., 2005. Dexamethasone alters F-actin architecture and promotes cross-linked actin network formation in human trabecular meshwork tissue. *Cell motility and the cytoskeleton*, 60(2), pp.83–95.

Clark, A.F. & Wordinger, R.J., 2009. The role of steroids in outflow resistance.

Experimental eye research, 88(4), pp.752–9.

Clark, a F. et al., 1995. Dexamethasone-induced ocular hypertension in perfusion-cultured human eyes. *Investigative ophthalmology & visual science*, 36(2), pp.478–89.

Costa, K.D., 2006. Imaging and probing cell mechanical properties with the atomic force microscope. *Methods in molecular biology (Clifton, N.J.)*, 319, pp.331–61.

Costa, K.D. & Yin, F.C., 1999. Analysis of indentation: implications for measuring mechanical properties with atomic force microscopy. *Journal of biomechanical engineering*, 121(5), pp.462–71.

Coughlin, M.F. et al., 2006. Filamin-a and rheological properties of cultured melanoma cells. *Biophysical journal*, 90(6), pp.2199–205.

Crick, S.L. & Yin, F.C.-P., 2007. Assessing micromechanical properties of cells with atomic force microscopy: importance of the contact point. *Biomechanics and modeling in mechanobiology*, 6(3), pp.199–210.

Deng, L. et al., 2004. Localized mechanical stress induces time-dependent actin cytoskeletal remodeling and stiffening in cultured airway smooth muscle cells. *American journal of physiology. Cell physiology*, 287(2), pp.C440-8.

Dimitriadis, E.K. et al., 2002. Determination of elastic moduli of thin layers of soft material using the atomic force microscope. *Biophysical journal*, 82(5), pp.2798–810.

Discher, D., Dong, C. & Fredberg, J., 2009. Biomechanics: cell research and applictions for the next decade. *Annals of biomedical …*, 37(5), pp.847–859.

Discher, D.E., Janmey, P. & Wang, Y.-L., 2005a. Tissue cells feel and respond to the stiffness of their substrate. *Science (New York, N.Y.)*, 310(5751), pp.1139–43.

Discher, D.E., Janmey, P. & Wang, Y.-L., 2005b. Tissue cells feel and respond to the stiffness of their substrate. *Science (New York, N.Y.)*, 310(5751), pp.1139–43.

Eghiaian, F., Rigato, A. & Scheuring, S., 2015. Structural, Mechanical, and Dynamical Variability of the Actin Cortex in Living Cells. *Biophysical Journal*, 108(6), pp.1330–1340.

Ehrlicher, A.J. et al., 2015. Alpha-actinin binding kinetics modulate cellular dynamics and force generation. *Proceedings of the National Academy of Sciences of the United States of America*, pp.1–6.

Ellingsen, B.A. & Grant, W.M., 1971. The relationship of pressure and aqueous outflow in enucleated human eyes. *Invest Ophthalmol*, 10(6), pp.430–437.

Ethier, C.R. et al., 1986. Calculation of flow resistance in the juxtacanalicular meshwork. ARVO Abstracts. *Investigative Ophthalmology and Visual Science*, 24(3), p.135.

Ethier, C.R., 2002. The inner wall of Schlemm's canal. *Exp Eye Res*, 74(2), pp.161–172.

Ethier, C.R., Johnson, M. & Ruberti, J., 2004. Ocular biomechanics and biotransport. *Annual review of biomedical engineering*, 6, pp.249–73.

Fabry, B. et al., 2001. Scaling the microrheology of living cells. *Physical review letters*, 87(14), p.148102.

Fabry, B. et al., 2003. Time scale and other invariants of integrative mechanical behavior in living cells. *Physical review. E, Statistical, nonlinear, and soft matter physics*, 68(4 Pt 1), p.41914.

Freddo, T. & Johnson, M., 2008. Aqueous humor outflow resistance. *The Eye's Aqueous Humor*, 62, pp.161–192.

Gasiorowski, J.Z., Murphy, C.J. & Nealey, P.F., 2013. Biophysical cues and cell behavior: the big impact of little things. *Annual review of biomedical engineering*, 15, pp.155–76.

Guo, M. et al., 2013. The role of vimentin intermediate filaments in cortical and cytoplasmic mechanics. *Biophysical Journal*, 105(7), pp.1562–1568.

Harewood, F.J. & McHugh, P.E., 2007. Comparison of the implicit and explicit finite element methods using crystal plasticity. *Computational Materials Science*, 39(2), pp.481–494.

Hotulainen, P. & Lappalainen, P., 2006. JCB : ARTICLE. , 173(3), pp.383–394.

Humphrey, 2002. *Cardiovascular solid mechanics*,

Hutter, J.L. & Bechhoefer, J., 1993. Calibration of Atomic-Force Microscope Tips. *Review Of Scientific Instruments*, 64(7), pp.1868–1873.

Jackson, W.M. et al., 2008. Over-expression of alpha-actinin with a GFP fusion protein is sufficient to increase whole-cell stiffness in human osteoblasts. *Annals of biomedical engineering*, 36(10), pp.1605–14.

Johnson, M., 2006. "What controls aqueous humour outflow resistance?". *Experimental eye research*, 82(4), pp.545–57.

Johnson, M., Chan, D. & Read, A., 2002. The pore density in the inner wall endothelium of Schlemm’s canal of glaucomatous eyes. *... ophthalmology & visual ...*, pp.2950–2955.

Johnson, M. & Tamm, E., 2010. Biomechanics of aqueous humor outflow resistance. pdf [Accessed March 14, 2014].

Johnson, M.C. & Kamm, R.D., 1983. The role of Schlemm’s canal in aqueous outflow from the human eye. *Investigative Ophthalmology and Visual Science*, 24(3), pp.320–325.

Jonas, J.B. et al., 1992. Human Optic-Nerve Fiber Count and Optic Disk Size. *Investigative Ophthalmology & Visual Science*, 33(6), pp.2012–2018.

Jones, R. & Rhee, D.J., 2006. Corticosteroid-induced ocular hypertension and glaucoma: a brief review and update of the literature. *Current opinion in ophthalmology*, 17(2), pp.163–167.

Karl, M.O. et al., 2005. Differential P1-purinergic modulation of human Schlemm’s canal inner-wall cells. *American journal of physiology. Cell physiology*, 288(4), pp.C784-94.

Kersey, J.P. & Broadway, D.C., 2006. Corticosteroid-induced glaucoma: a review of the literature. *Eye*, 20(4), pp.407–416.

Kizhatil, K. et al., 2014. Schlemm’s canal is a unique vessel with a combination of blood vascular and lymphatic phenotypes that forms by a novel developmental process. *PLoS biology*, 12(7), p.e1001912.

Last, J. a et al., 2011. Elastic modulus determination of normal and glaucomatous human trabecular meshwork. *Investigative ophthalmology & visual science*, 52(5), pp.2147–52.

Lautenschläger, F. et al., 2009. The regulatory role of cell mechanics for migration of differentiating myeloid cells. *Proceedings of the National Academy of Sciences of the United States of America*, 106(37), pp.15696–15701.

Lei, Y., Rajabi, S., et al., 2011. In vitro models for glaucoma research: effects of hydrostatic pressure. *Investigative ophthalmology & visual science*, 52(9), pp.6329–39.

Lei, Y., Overby, D.R., et al., 2011. Outflow physiology of the mouse eye: pressure dependence and washout. *Investigative ophthalmology & visual science*, 52(3), pp.1865–71.

Leonard, D.N., Chandler, G.W. & Seraphin, S., 2012. *Scanning Electron Microscopy*,

Lin, D.C., Dimitriadis, E.K. & Horkay, F., 2007. Robust strategies for automated AFM force curve analysis--I. Non-adhesive indentation of soft, inhomogeneous materials. *Journal of biomechanical engineering*, 129(3), pp.430–40.

Mao, W., Tovar-Vidales, T. & Yorio, T., 2011. Perfusion-cultured bovine anterior segments as an ex vivo model for studying glucocorticoid-induced ocular hypertension and glaucoma. *... ophthalmology & visual ...*, 52(11), pp.8068–75.

Mendez, M.G., Kojima, S. & Goldman, R.D., 2010. Vimentin induces changes in cell shape, motility, and adhesion during the epithelial to mesenchymal transition. *FASEB journal : official publication of the Federation of American Societies for Experimental Biology*, 24(6), pp.1838–1851.

Mendez, M.G., Restle, D. & Janmey, P. a., 2014. Vimentin Enhances Cell Elastic

Behavior and Protects against Compressive Stress. *Biophysical Journal*, 107(2), pp.314–323.

Mijailovich, S., Kojic, M. & Zivkovic, M., 2002. A finite element model of cell deformation during magnetic bead twisting. *Journal of Applied …*, 93(4), pp.1429–1436.

Molecular Probes™, 2010. The Molecular Probes ® Handbook Molecular Probes ™ Handbook Their Amine-Reactive Probes Derivatives Fluorophores.

Morgan, J.T. et al., 2014. Robust and artifact-free mounting of tissue samples for atomic force microscopy. *BioTechniques*, 56(1), pp.40–2.

Na, S. et al., 2008. Rapid signal transduction in living cells is a unique feature of mechanotransduction. *Proceedings of the National Academy of Sciences*, 105(18), pp.6626–6631.

Ng, L. et al., 2007. Nanomechanical properties of individual chondrocytes and their developing growth factor-stimulated pericellular matrix. *Journal of biomechanics*, 40(5), pp.1011–23.

Overby, D. & Bertrand, J., 2014. Ultrastructural changes associated with dexamethasone-induced ocular hypertension in mice. *… ophthalmology & visual*

Overby, D.R. et al., 2014. Altered mechanobiology of Schlemm's canal endothelial cells in glaucoma. *Proceedings of the National Academy of Sciences of the United States of America*, 111(38), pp.13876–81.

Overby, D.R., Stamer, W.D. & Johnson, M., 2009. The changing paradigm of outflow resistance generation: towards synergistic models of the JCT and inner wall endothelium. *Experimental eye research*, 88(4), pp.656–70.

Price, L.S. et al., 1998. Activation of Rac and Cdc42 by Integrins Mediates Cell Spreading. *Molecular Biology of the Cell*, 9(7), pp.1863–1871.

Puig, F. et al., 2007. Stiffening and Contraction Induced by Dexamethasone in Alveolar Epithelial Cells. *Experimental Mechanics*, 49(1), pp.47–55.

Quigley, H. a & Broman, a T., 2006. The number of people with glaucoma worldwide in 2010 and 2020. *The British journal of ophthalmology*, 90(3), pp.262–7.

Raghunathan, V.K. et al., 2015. Dexamethasone Stiffens Trabecular Meshwork, Trabecular Meshwork Cells, and Matrix. *Investigative Opthalmology & Visual Science*, 56(8), p.4447.

Read, a T., Chan, D.W.-H. & Ethier, C.R., 2006. Actin structure in the outflow tract of normal and glaucomatous eyes. *Experimental eye research*, 82(6), pp.974–85.

Reffay, M. et al., 2014. Interplay of RhoA and mechanical forces in collective cell migration driven by leader cells. *Nat Cell Biol*, 16(3), pp.217–223.

Rico, F. et al., 2005. Probing mechanical properties of living cells by atomic force microscopy with blunted pyramidal cantilever tips. *Physical Review E*, 72(2), p.21914.

Riveline, D. et al., 2001. Focal contacts as mechanosensors: Externally applied local mechanical force induces growth of focal contacts by an mDia1-dependent and ROCK-independent mechanism. *Journal of Cell Biology*, 153(6), pp.1175–1185.

Russell, P. & Johnson, M., 2012. Elastic Modulus Determination of Normal and Glaucomatous Human Trabecular Meshwork. *Investigative Opthalmology &*

Visual Science, 53(1), p.117.

Sit, S.-T. & Manser, E., 2011. Rho GTPases and their role in organizing the actin cytoskeleton. *Journal of cell science*, 124(Pt 5), pp.679–683.

Solon, J. et al., 2007. Fibroblast adaptation and stiffness matching to soft elastic substrates. *Biophysical journal*, 93(12), pp.4453–61.

Stamer, W. & Roberts, B., 1998. Isolation, culture, and characterization of endothelial cells from Schlemm's canal. *… ophthalmology & visual …*, pp.1804–1812.

Suresh, S. et al., 2005. Connections between single-cell biomechanics and human disease states: gastrointestinal cancer and malaria. *Acta biomaterialia*, 1(1), pp.15–30.

Tham, Y.C. et al., 2014. Global prevalence of glaucoma and projections of glaucoma burden through 2040: A systematic review and meta-analysis. *Ophthalmology*, 121(11), pp.2081–2090.

Vajaranant, T.S. et al., 2012. A 40-year forecast of the demographic shift in primary open-angle glaucoma in the united states. *Investigative Ophthalmology and Visual Science*, 53(5), pp.2464–2466.

Vargas-Pinto, R., 2011. A thesis on Young ' s Modulus of Healthy and Glaucomatous Schlemm ' s Canal Endothelial Cells Using Atomic Force Microscopy. , (December).

Vargas-Pinto, R. et al., 2014. Finite element analysis of the pressure-induced deformation of Schlemm's canal endothelial cells. *Biomechanics and Modeling in Mechanobiology*, (Johnson 2006), pp.851–863.

Vargas-Pinto, R. et al., 2013. The effect of the endothelial cell cortex on atomic force microscopy measurements. *Biophysical Journal*, 105(2), pp.300–309.

Wang, N., Butler, J.P. & Ingber, D.E., 1993. Mechanotransduction across the cell surface and through the cytoskeleton. *Science (New York, N.Y.)*, 260(5111), pp.1124–7.

Wessendorf, M., 2004. Autofluorescence: Causes and Cures. *Internet*, pp.1–8.

Xu, J., 2005. Preparation, Culture, and Immortalization of Mouse Embryonic Fibroblasts. *Current Protocols in Molecular Biology*, Chapter 28, pp.1–8.

Yamada, H., Mouri, N. & Nobuhara, S., 2010. Three-Dimensional Morphometry of Single Endothelial Cells with Substrate Stretching and Image-Based Finite Element Modeling. *EURASIP Journal on Advances in Signal Processing*, 2010, pp.1–11.

Zeng, D. et al., 2010. Young's modulus of elasticity of Schlemm's canal endothelial cells. *Biomechanics and modeling in mechanobiology*, 9(1), pp.19–33. A

Zhou, E.H. et al., 2012. Mechanical responsiveness of the endothelial cell of Schlemm's canal: scope, variability and its potential role in controlling aqueous humour outflow. *Journal of the Royal Society, Interface / the Royal Society*, 9(71), pp.1144–55.

Appendix

A. Human Eye Perfusion and Facility Measurement Procedure

Date: __________

Eye type: Normal , Glaucoma Number:_______________

Name of the eye bank: ____

Death time and procurement interval:

Arrival Date &Time: ______________________________________ Eye Type: Paired Not Paired

Name of People Doing the Experiment:

Notes:

____

____

____

____

Equipment and materials for 1 eye perfusion:

Ultra pure UV filtered nanowater
0.9% Sodium Chloride (2250mg/250ml)
Bleach
Dulbecco's Phosphate Buffered Saline
Glucose
70% Ethanol
Water bath and thermometer
1×25 gauge butterfly needles
4×Three way Mallinckrodt stopcocks
2×2.5ml Hamilton gas-tight glass syringes
3×24" Mallinckrodt 0.050" ID tubing
2×0.2 μm Acrodisk syringe filters
1×30ml syringe
1×10ml reservoir syringes
3×25ml beakers
2×250ml beakers
Dissection tray
Kimwipes
Paper towels
Labels and pens
PPE (lab coat, latex gloves, facemask, safety glasses)

Start up

1. Wear PPE including latex glove and lab coat
2. Turn on the pumps
3. Turn on the water bath. Pour in tap water. Set temp at 34^{0}C.

   Water bath temp:________ºC

   Time:

DBG solution preparation **Date: _________ Time: _________**

1. Wash two 250ml beakers and a 100ml graduated cylinder. Rinse with Nanowater
2. Label beakers DBG and DPBS
3. Measure 198 mg of glucose and place in beaker labeled DPBS
4. Add 200ml of Dulbecco's Phosphate Buffered Saline (DPBS) into the beaker containing 198 mg glucose to make 5.5mM glucose + DPBS (DBG) solution
5. Place beaker in water bath to let glucose fully dissolve
6. Filter the 200ml solution with 0.2μm Acrodisk syringe filter and 30ml syringe. Place filtered solution in beaker labeled **DBG**
7. Cover DBG beaker with parafilm and set DBG beaker in water bath (34^{0}C) for purpose of degassing

LabView setup

1. Open LabView to Perfusion Master (PerfusionMaster.vi)
2. Press white arrow in top left corner of the window to activate the dialog box
3. Save Datalog file
4. Open DefaultSetup file, then press Setup icon to bring up the setup window
   - Define number of channels, specify a data file name for each channel, save

- Define length of perfusion, save
- System parameters: use default values
- Control parameters: use default values
- State variables: Specify **constant flow rate** or **constant pressure** for each channel, save
- Calibrate syringe pumps: 2.5ml Hamilton syringe, save
- Calibrate transducers:
  - Set number of calibration points to 3
  - Select channel and input 3 meniscus heights
  - Mean Standard error of the calibration should be less than 0.01. If not, try again

Channel #0	**Channel #1**
Calibration Pressure (mmHg)	Calibration Pressure (mmHg)
#1 ____________	**#1** ____________
#2 ____________	**#2** ____________
#3 ____________	**#3** ____________
Slope: ____________	**Slope:** ____________
Intercept: _________	**Intercept:** ___________
MSE: _____________	**MSE:** ___________
Length of Perfusion: _____________	**Length of Perfusion**:
Perfusion Mode: Constant P , Constant Q	**Perfusion Mode**: Constant P , Constant Q
Perfusion P or Q: _____________________	**Perfusion P or Q**:

5. Continue on to next section then return to zero transducers (#6)
6. Zero Transducers:
   - Place beaker (25ml) filled with nanowater in the water bath making sure that the beaker is filled to the same level where the needle will be

  inserted into the eye

  - Place the needles in the beaker
  - Check that the perfusion reservoir is valved off and that the line from the transducer to the needle is open, and the calibration tubing is valved off
  - Select the channel and zero the transducer. Pressure reading should be between -0.2 and 0.2

Notes:

____

____

Experiment setup:

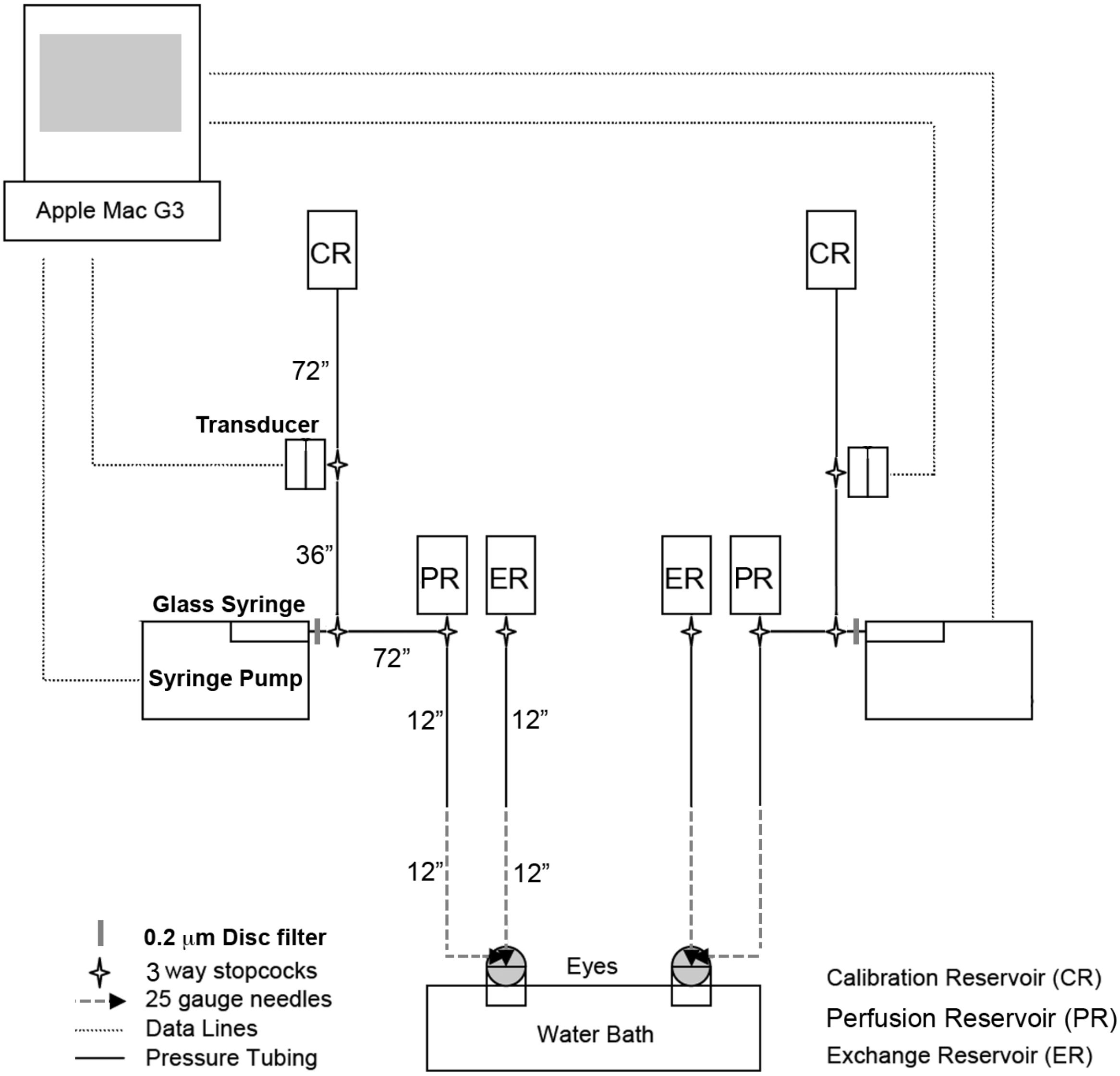

1. Fill a Hamilton Syringes (2.5ml) with DBG solution for perfusion and purge any air bubbles
2. Using a 10ml disposable syringe fill 1 Acrodisk syringe filters with DBG and apply each filter the end of the Hamilton syringe through DBG-DBG

connection

3. Attach a stopcock to the end of each filter
4. Attach 36" pressure tubing from the pressure transducer to one side of the stopcock via water to DBG connection
5. Attach 24" sterile pressure tubing to the other side of the stopcock
6. Attach a stopcock to the end of the 24" pressure tubing
7. Fill a disposable 10ml syringe with DBG solution to be used as the perfusion reservoir and place it on a ring stand. Attach the stopcock from step 6 to the end of the reservoir. Attach a 24" pressure tubing to the stopcock
8. Take a 25 gauge butterfly needle and remove the plastic wings. Attach the needle to the stopcock from step 8. Valve off the perfusion reservoir once the needle is filled with DBG solution
9. Check for and purge any air bubbles that may have formed in the system. Air bubbles often form in or near the stopcocks
10. Carefully check and purge any air bubbles
11. Place the needles from step 10 into a clean 25ml beaker filled with nanowater. Place the beaker in the water bath
12. Go back and zero the transducers (step 6 of previous section)

Time:

Notes:

Eye preparation

1. Position paper towels around the bench top and dissection tray to absorb any spills
2. Obtain a pair of eyes from the refrigerator and place in the dissection tray

Time: _________

3. Check for cuts on the cornea surface
4. Remove orbital fat and muscles from the eye and dispose tissue in a 10%

bleach solution

5. Place the eyes in 25 ml beakers
    - Fill bottom of beaker with gauze pads so that the cornea is at the same level as the rim of the beakers
    - Fill the beaker with .9% saline solution
    - Place a piece of Kimwipe over the cornea so that it does not dry out

6. Place beakers in the water bath at 34°C. Make sure the eyes are warm enough for needle insertion (no cold cataracts)
7. Once the cold cataract is clear, the eye is ready for needle insertion
8. Remove the Kimwipe from the cornea of the eye
9. Open the needle, which is in line with the transducer, to the perfusion reservoir
10. Once there is a steady flow coming out of the needle, insert the needle into the eye
    - Insert the needle through the perimeter of the cornea into the anterior chamber
    - Note the time of needle insertion

    Channel 0 Time: ________ **Channel 1 Time: ________**

    - Be careful not to make contact with the iris or lens
11. Carefully place the needle under the iris to prevent anterior chamber deepening. Do not tent the iris and do not dig under it
12. Adjust the height of perfusion reservoir to make perfusion pressure. (Usually 10 mmHg)
13. Wait 2 minutes for eye pressure to equilibrate at perfusion pressure. (Usually 10 mmHg)

    Channel 0 Time: ____________ Pressure: ____________ mmHg

    Channel 1 Time: ____________ Pressure: ____________ mmHg

Notes:

____

____

Measuring baseline facility

1. Check that both eyes are at the desired perfusion pressure before closing off the perfusion reservoir
2. Make sure that the stopcock at the filter is open, that the transducer is open to the system only and the stopcock to the exchange reservoir is closed
3. Valve off the perfusion reservoir and keep the perfusion needle open to the system. In LabView click 'adjust channel', 'pause' and then accept changes so the perfusion will begin
4. Record the initial volume of the fluid in syringe

   Channel 0: __________ [μL] **Channel 1: __________ [**μL]
5. Start perfusion (usually constant 10 mmHg for 30 minutes) for eye to reach baseline facility.
6. Record the facility and final volume of the fluid inside the syringe below

   Start Time: _________ **End Time: _________**

   Facility: Channel 0: __________ **Channel 1:**

   __________[μL/min/mmHg]

   Volume: Channel 0: __________ [μL] **Channel 1: __________ [**μL]

	DBG Volume perfused		Facility	
Time	**Channel 0**	**Channel 1**	**Channel 0**	**Channel 1**

Notes:

Clean up

1. Dress in protective clothing including gloves and a lab coat
1. Dispose of needles in proper receptacle
2. Place all contaminated material in a biohazard bag
3. Disinfect all countertops with a 10% bleach solution and let sit for 20 min
4. Place all glassware, stopcocks and disposable tubing into a 10% bleach solution for 20 Minutes
5. Place all metalware in a 70% Ethanol solution for 20 minutes to disinfect
6. Disinfect DPBS with 10% bleach solution and dispose of in the sink
7. Dispose of tubing, stopcocks, and reservoirs in ordinary wastebasket after disinfecting
8. Wash all glassware and metal ware with soap and distilled water
9. Either disinfect the contents of the biohazard bag with a 10% bleach solution or put in freezer to await autoclaving. After either of these sterilization processes the material may be double bagged and disposed of in a normal trash receptacle
10. Wash hands and organize lab

B. Procedure to dissect a human eye to extract SC inner wall

1. Wear gloves and preferably lab coats during all steps.
2. Put the eye in an antiseptic solution like Betadine and let it sit for 5 minutes.
3. Take the eye out and rinse it with DPBS.
4. Cut the fat and tissues off the eye using forceps and scissors.
5. Find the blood vessel on sclera at the backside of the eye.
6. Find the temporal muscle (located at temporal side) that is running downward. From this muscle we can figure out if the eye is the right or the left one.

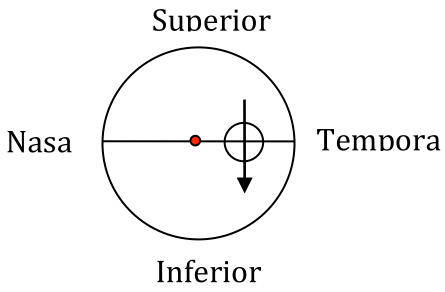

Sketch for the right eye

7. Use the blade to make a cut on the sclera and make a wedge to specify the temporal side of the eye as shown in figures below.


8. Take the cut all the way around the eye and cut the eye into half.

9. Use the fine forceps to take the lens out. Lift up the lens with the forceps and use the scissors to cut the zonule fibers attached to the lens.


10. Use big forceps to separate retina from the choroid. Hold the choroid with one and gently pull the retina. Change the location and repeat if necessary.


11. Use the cutter blade to cut the eye to quadrants. Add some DPBS if the eye is drying out. The cutting directions are shown below.

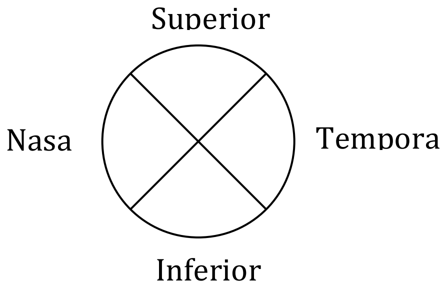

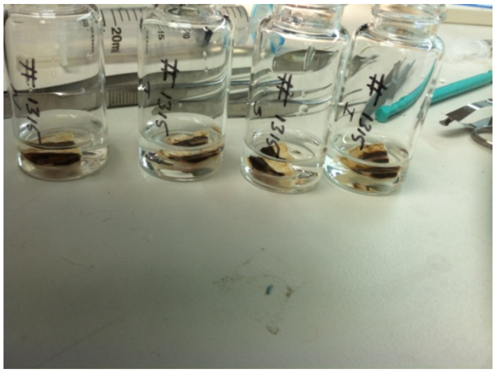

12. Label 4 vials with the eye number and the cutting region spec and fill with DPBS. For longer storage, use Co_2 independent media with 10 FBS and 1% Pen. Strep.
13. Cut each quadrant to 5 sections and store in the vials.

- **Find the Schlemm's Canal**

1- Prepare the instruments (2 fine forceps, blade breaker and brittle blade, two 30 G1/2 needles to fix the sclera and the cornea).

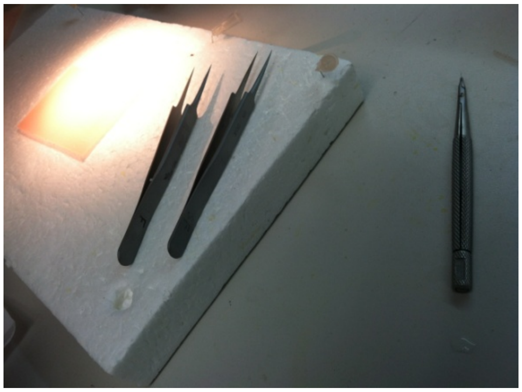

2- Take out a section from one of the vials and dry the sclera on a piece of napkin.
3- Keep the cornea fixed to the substrate and put a pin in it to fix it. Do the same thing to the sclera next.

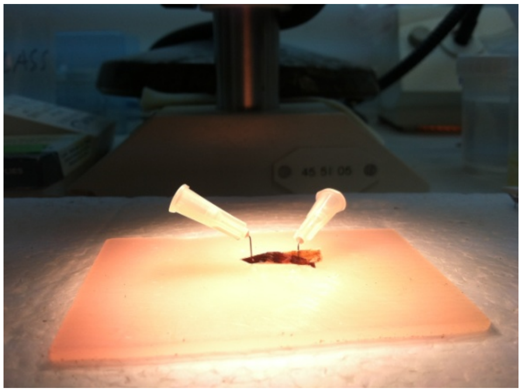

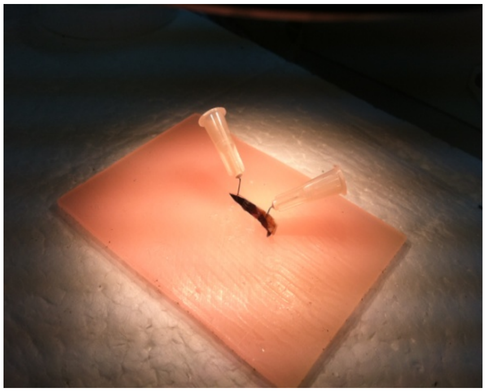

4- Cut the iris and ciliary body. Make sure not to cut parts of ciliary body that support the canal.

5- Grab the choroid and pull it toward the cornea.

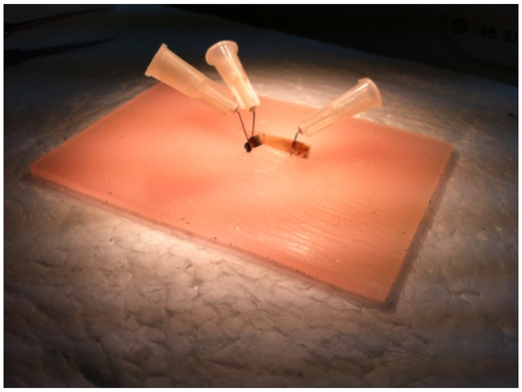

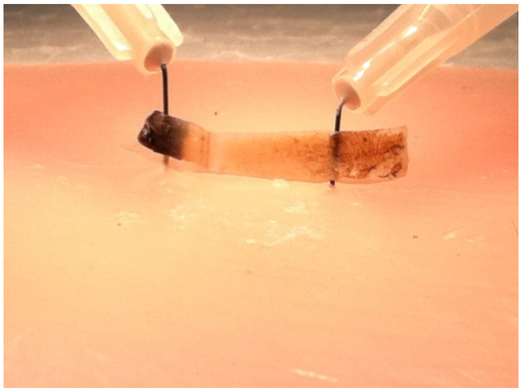

6- Look for Canal and locate the hinge. Keep the blade as close as possible to the cornea and start cutting the hinge from the top side.

7- Remove both needles from the cornea and the sclera. Pin the sclera to the board as shown below.

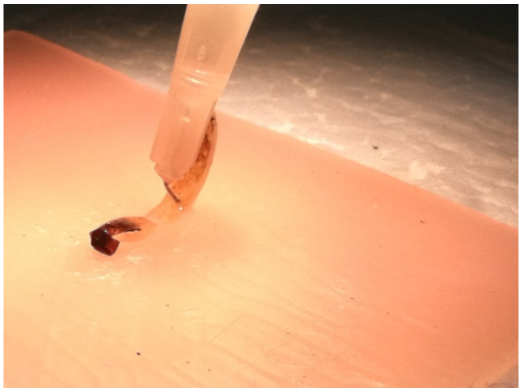

8- Cut the sclera as close as possible to the IW.
9- Make a small cut at one edge to mark the SC side of the tissue
10- Detach the IW by cutting through the line it attaches to the sclera
11- Cut the piece of choroid that is attached to the Inner Wall (IW).
12- Make tubes and label them for each region. Store the IW attached to the cornea in its corresponding tube filled with fixative or PBS or Co2 independent media with 10 FBS and 1% Pen. Strep.
13- Disinfect all instruments in betadine solution for at least 5 minutes and rinse under hot water afterwards. Store the fat and tissue in a red biohazard bag and dispose based on the biohazard tissue disposal protocol.

C. Outflow facility measurements

Tissue ID	**Source**	**Outflow facility** (µ//min*mmHg)	**Age**	**Gender**	**Normal Or Glaucoma**
W4035-V0182000	Eversight	0.21	59	M	N
W4035-V0180000	Eversight	0.25	69	M	N
W4036-V0180000	Eversight	0.09	88	M	*G

D. Optic nerve counting results

Tissue ID	**Total Cross-Sectional Area**	**Neural Area**	**No of Axons**	**Age**	**Gender**	**Normal or Glaucoma**
2411-15-01 (OS)	7,42 mm2	5,18 mm2	461013	80	F	N
2633-15-01 (OS)	No optic nerve	NA	NA	83	F	N
2633-15-01 (OD)	5,45 mm2	4,06 mm2	401778	83	F	N
W4035-V0183000	10.01 mm2	7,94 mm2	765436	60	F	N
W4035-V0180000	9,70 mm2	8,23 mm2	1084664	69	M	N
W4036-V0180000	4,01 mm2	1,13 mm2	7327	88	M	*G

E. **The number of measurements (n) and values for E_1 and E_2, for the merged data in normal (N1-N9) and glaucoma (G) samples.** Data is presented based on the ramp sizes up to 500nm, 1000nm, and 2000nm.

			N1	**N2**	**N3**	**N4**	**N5**	**N6**	**N7**	**N8**	**N9**	**G**
500nm Ramp	**E_1 (kPa)**	**Modulus (kPa)**	0.43	0.33	0.34	0.67	0.65	0.35	0.26	0.23	0.19	0.69
		n	17	35	38	25	17	17	13	12	7	39
	E_2 (kPa)	**Modulus (kPa)**	5.86	3.32	2.40	6.19	5.64	11.8	NA	14.36	14.1	14.0
		n	5	7	3	7	3	3	0	3	2	25
1000nm Ramp	**E_1 (kPa)**	**Modulus (kPa)**	0.28	0.25	0.3	0.58	0.64	0.35	0.26	0.23	0.25	0.65
		n	10	19	20	16	12	17	13	12	6	38
	E_2 (kPa)	**Modulus (kPa)**	10.5	3.25	3.41	6.11	4.79	6.33	NA	14.36	11.2	11.8
		n	3	4	2	5	3	6	0	3	3	3
2000nm Ramp	**E_1 (kPa)**	**Modulus (kPa)**	0.2	NA	NA	0.54	0.63	0.35	0.28	0.23	0.25	0.65
		n	1	0	0	11	6	17	12	12	6	38
	E_2 (kPa)	**Modulus (kPa)**	NA	NA	NA	5.12	5.00	6.34	1.12	14.35	11.2	10.1
		n	0	0	0	2	1	6	2	3	3	43

F. **The number of measurements (n) and values for E_{final} for the dark and bright regions in normal (N; n=9) and glaucoma (G; n=1) samples.** Data is presented based on the analyzed indentation size.

			N		**G**	
			Bright	**Dark**	**Bright**	**Dark**
200nm Indentation	**E_{final} (kPa)**	**Modulus (kPa)**	1.43	1.75	7.9	6.48
		n	162	97	7	81
500nm Indentation	**E_{final} (kPa)**	**Modulus (kPa)**	0.88	1.42	4.03	4.95
		n	80	33	2	56
1000nm Indentation	**E_{final} (kPa)**	**Modulus (kPa)**	0.69	0.73		4.02
		n	32	7		33

G. Examples of the plots for patterns P1-P5 (The label specifies the experiment date and file number)

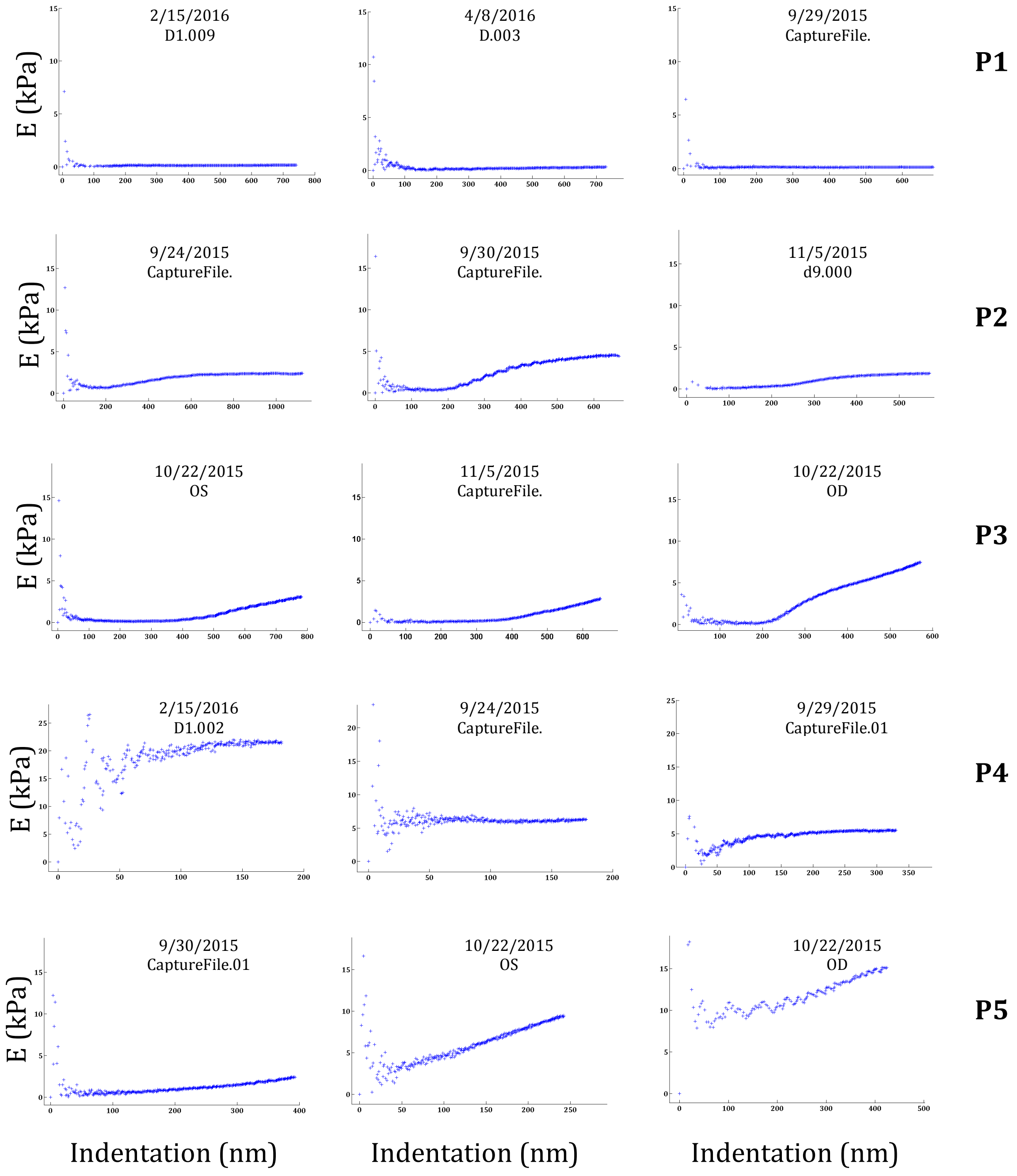

H. Young's Modulus (kPa) values from the dexamethasone experiment

AFM sharp tip

Cell line	Control	0.01µM	0.1µM	1µM
SC 76	6.21±0.7	6.57±1.08	8.92±1	12.83±1.09
SC 71	6.09±0.96	4.54±0.44	5.54±0.6	9.86±1.59
SC 57g	7.81±0.67	7.54±0.64	12.10±1.81	16.28±1.92
SC 64g	5.41±0.67	7.70±0.51	5.94±0.41	11.85±1.97

AFM rounded (10µm) tip

Cell line	Control	0.01µM	0.1µM	1µM
SC 76	1.15±0.2	1.47±0.24	1.26±0.15	1.16±0.16
SC 71	1.53±0.2	1.17±0.15	1.08±0.11	1.42±0.42
SC 57g	1.30±0.17	1.37±0.2	1.33±0.24	1.40±0.21
SC 64g	1.73±0.22	1.13±0.16	1.17±0.18	1.35±0.4

I. Young's Modulus (kPa) values from alpha actinin and RhoA experiment

AFM sharp tip

Cell line	No virus	GFP	A-Actinin	RhoA
SC 57g	7.99±1.19	5.00±1.25	11.04±1.82	11.94±1.44
SC 69	3.74±0.5	2.97±0.63	5.62±0.64	7.82±0.93
SC 71	-	7.03±1.03	10.56±0.82	9.62±1.22
SC 73	4.46±0.58	5.50±0.54	7.12±0.86	7.63±0.57
SC 76	2.83±0.41	3.29±0.51	4±0.44	-

AFM rounded (10μm) tip

Cell line	No virus	GFP	A-Actinin	RhoA
SC 57g	0.77±0.09	0.48±0.15	0.55±0.1	0.45±0.08
SC 69	0.58±0.16	0.70±0.16	0.56±0.16	0.40±0.05
SC 71	-	0.69±0.1	0.67±0.15	0.43±0.18
SC 73	1.45±0.21	0.78±0.1	0.36±0.1	0.75±0.19
SC 76	0.55±0.07	0.4±0.03	0.46±0.1	-

`

J. Western blot for dexamethasone experiment comparing the expression level of βactin, SMA, vimentin, and tubulin.

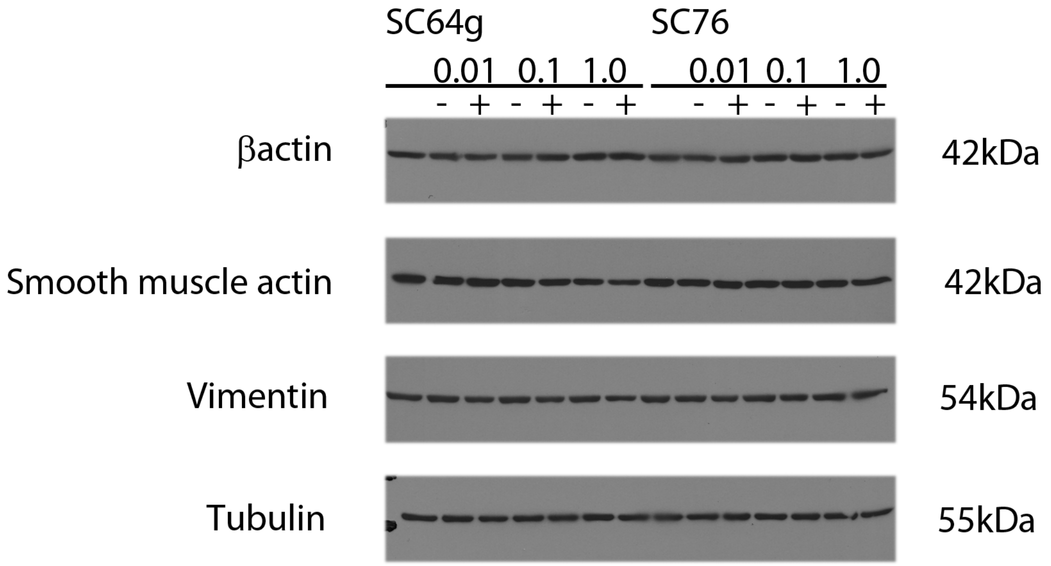

K. Western blot for RhoA and alpha actinin experiments comparing the expression level of α-actinin, vimentin, β-actin, and tubulin.